ORNL/TM-2015/270

Manufacturing Demonstration Facility: Roll-to-Roll Processing

Panos G. Datskos
Pooran C. Joshi
Chad E. Duty
Frederick A. List
Beth L. Armstrong
Ilia N. Ivanov
Christopher B. Jacobs
David E. Graham
Ji Won Moon

August 5, 2015

ORNL/ TM-2015/270

Advanced Manufacturing Office

MANUFACTURING DEMONSTRATION FACILITY: ROLL-TO-ROLL PROCESSING

Author(s)
Panos G. Datskos
Pooran C. Joshi
Chad E. Duty
Frederick A. List
Beth L. Armstrong
Ilia N. Ivanov
Christopher B. Jacobs
David E. Graham
Ji Won Moon

Date Published: June, 2015

Prepared by
OAK RIDGE NATIONAL LABORATORY
Oak Ridge, TN 37831-6283
managed by
UT-BATTELLE, LLC
for the
US DEPARTMENT OF ENERGY
under contract DE-AC05-00OR22725

CONTENTS

LIST OF FIGURES

LIST OF TABLES

ACRONYMS AND ABBREVIATIONS

ABS	Acrylonitrile Butadiene Styrene
AMO	Advanced Manufacturing Office
CATS	Center for Advanced Thin-film Systems
CAD	Computer Aided Drafting
CIGS	Copper Indium Gallium Sulfide
Cm	Centimeter
CNMS	Center for Nanophase Materials Science
CW	Continuous Wave
DOE	Department of Energy
EERE	Office of Energy Efficiency and Renewable Energy
FCC	Face Centered Cubic
FDM	Fused Deposition Modelling
FFT	Fast Fourier Transform
FGA	Forming Gas Annealing
FTIR	Fourier Transfer InfraRed
GLY	Glycine
IDE	InterDigitated Electronics
IEP	IsoElectric Point
ITO	Indium Tin Oxide
I-V	Current-Voltage
kHZ	KiloHertz
KW	KiloWatt
L	Liter
LED	Light Emitting Diode
LGT	Langatate
MHZ	Megahertz
mM	micromole
MW	Molecular Weight
NF	NanoFermentation
nM	NanoMole
nm	nanometer
NP	Nanoparticle
NTA	Nitrilotriacetic acid
ORNL	Oak Ridge National Laboratory
PEG	Polyethylene glycol
PEI	Polyethyleneimine
PET	Polyethylene Terephthalate
PI	Polyimide
pL	Picoliter
PL	PhotoLuminesence
PLD	Pulse Laser Deposition
PTP	Pulsed Thermal Processing
QE	Quantum Efficiency
RF	Radio Frequency
RF-SAW	Radio Frequency Surface Acoustic Wave
RFID	Radio-frequency Identification

RGB	Red, Green, Blue
RH	Relative Humidity
SEM	Scanning Electron Microscope
TEM	Transmission Electron Microscope
TCO	Transparent Conducting Oxide
TGA	Thermal Gravimetric Analysis
UV	UltraViolet
XPS	X-Ray Photoelectron Spectroscopy
XRD	X-Ray Diffraction
ZGT	Zinc Gallate

ACKNOWLEDGEMENTS

This Oak Ridge National Laboratory (ORNL) Manufacturing Demonstration facility (MDF) project was funded by the US Department of Energy (DOE), Office of Energy Efficiency and Renewable Energy (EERE) Advanced Manufacturing Office (AMO). This project was managed as CPS Agreement Number: 24764. The lead organization was the Oak Ridge National Laboratory. The project duration was from January 23, 2012 through March 31, 2015. Other project partners included: Novacentrix, Stratasys and Cabot Corporation.

EXECUTIVE SUMMARY

This Manufacturing Demonstration Facility (MDF) roll-to-roll processing project provided an excellent opportunity to investigate a number of advanced manufacturing approaches to achieve a path for low cost devices and sensors. Critical to this effort is the ability to deposit thin films at low temperatures using nanomaterials derived from nanofermentation (NF). The overarching goal of this project was to develop roll-to-roll manufacturing processes of thin film deposition on low-cost flexible substrates for electronics and sensor applications. This project utilized ORNL's unique Pulse Thermal Processing (PTP) technologies coupled with non-vacuum, low temperature deposition techniques, ORNL's clean room facility, slot dye coating, drop casting, spin coating, screen printing and other equipment including a Dimatix ink jet printer and a large-scale Kyocera ink jet printer.

This roll-to-roll processing project had three main tasks: 1) develop and demonstrate zinc-based opto-electronic sensors using low cost nanoparticulate structures manufactured in a related MDF Project using nanofermentation techniques, 2) evaluate the use of silver based conductive inks developed by project partner NovaCentrix for electronic device fabrication, and 3) demonstrate a suite of low cost printed sensors developed using non-vacuum deposition techniques which involved the integration of metal and semiconductor layers to establish a diverse sensor platform technology.

In this project we have developed non-vacuum, large-scale deposition and processing techniques for nanoparticle-based inks and pastes that reduce cost and energy requirements associated with processing of thin film electronics. We have demonstrated controllable assembly of multilayer (up to 15) nanofermented sulfide nanoparticles on areas up to 1ft x1ft with a scalable technology with direct transfer of deposition parameters to roll-to-roll processing. The nanoparticles of Zn based complexes were produced by a nanofermentation process, which was optimized to achieve the optimal nanoparticle size and distribution. Zn complexes were synthesized and evaluated in terms of optical properties and performance. We used X-ray Diffraction (XRD) to optimize the NF process for Zn complex synthesis. We performed photoluminescence (PL) measurements that helped establish the optical absorption and emission characteristics for optoelectronic applications. PTP was instrumental in processing non-vacuum low temperature deposition by taking advantage of short exposure time radiant heating (energy flux in excess of 20 kW/cm^2, heating rates up to 600,000°C/s) over a large uniform exposure are (1,000 cm^2).

The development of appropriate inks is critical for high quality thin films for electronics and sensor applications. In the project we pursued ink development using a variety of solvents, additives, modifiers, dispersants, and nanoparticles in order to produce thin and thick films on appropriate substrates. We deposited thin films using sonospray deposition and PTP to anneal the thin films, and then evaluated the PTP treatment in terms of the microstructure, optical, and electrical properties of thin films.

The sensors we have developed in this project can operate at 0.5 V compared to 5V required for conventional sensors. The sensor can be activated using ultraviolet (UV) light compared to conventional sensors that require 400°C for activation. Use of UV light is more energy efficient compared to using a high temperature system (see Figure 3.39(a)). The UV activation process improves sensor response by a factor of five, and the sensor response is directly proportional to the exposure time (amount of material). For the baseline sensor, the impedance was reduced by 55 kOhm under UV illumination, leading to a permanent change, and a 2x improvement in sensor impedance response to a single pulse. The sensor kinetics were 212 seconds with UV activation and 23 seconds partial recovery time (CO_2/H_2O).

Zinc-based opto-electronic sensors using low cost nanofermented nanoparticules can be commercially viable depending on the desired performance. For example, the results from this project indicate that the potential for such devices is high. Furthermore, the development of conductive inks is an important component for any electronics system and particularly important for realizing low cost printed sensors and establishing a sensor platform technology.

1. INTRODUCTION

1.1 PROJECT OBJECTIVE

The main objective of this project was to develop roll-to-roll manufacturing of thin film electronics on low-cost flexible substrates using ORNL's unique Pulse Thermal Processing (PTP) technologies coupled with non-vacuum low temperature deposition techniques. An additional objective of the project was to develop non-vacuum, large scale deposition and processing techniques for nanoparticle-based inks and pastes that reduced cost and energy requirements associated with processing of thin film electronics. The work performed was divided into three tasks:

1) Functionalization of Zn Complexes for Optoelectronics. This involved the development and demonstration of low-cost, phosphor materials and coatings for optoelectronic applications using zinc complexes produced by NanoFermentation (NF), deposited by low-temperature non-vacuum techniques, and sintered using Pulse Thermal Processing (PTP) technologies.
2) Drying and Sintering of Silver Inks. The main focus of this task was the evaluation of aqueous and solvent based conductive inks developed by NovaCentrix for electronic device applications. Our goal was to deposit silver inks on plastic substrates by roll-to-roll compatible inkjet printing and screen-printing techniques and use the PulseForge tool to combine the drying and sintering processes into a single pass for high throughput commercial applications – potentially reducing processing time by 2-3 orders of magnitude.
3) Low Cost Printed Sensors. The objective of this task was to demonstrate low cost printed sensor development by non-vacuum deposition techniques employing low thermal budget photonic curing. This work involved integration of metal and/or semiconductor layers to establish a diverse sensor technology platform. The initial application for the low cost sensor technology is a thin film temperature sensor for energy efficient buildings, defense applications, and manufacturing diagnostics.

1.2 PROJECT BACKGROUND

Developing roll-to-roll manufacturing processes for thin film deposition on low-cost flexible substrates will enable the fabrication of cost-effective electronics and sensor and device applications. In order to accomplish the project objectives it is necessary to demonstrate materials and coatings with low-cost nanoparticle structures manufactured using nanofermentation techniques. The development of appropriate inks is critical for high quality thin films for electronics and sensor applications. This involved evaluation of silver conductive inks by focusing on the sintering and electrical performance of ink jet printed materials. In addition, the development of non-vacuum, large-scale deposition and processing techniques for nanoparticle-based inks and pastes is important in reducing cost and energy requirements associated with processing of thin film electronics.

An important factor that impacts the eventual thin film performance is the amount of impurities or residue left behind from burn-out of surfactant materials and dispersants. It is crucial to understand not only the nature of these impurities but also the amount that can be tolerated in order to still have acceptable thin film materials for the particular application. The impact of particle size and distribution on the coating quality also need to be understood, and therefore coatings should be characterized for their structural, optical, and electrical properties. For example, resistive sensors based on nanoparticles can be used to analyze the gas sensing characteristics of SnO_2 particles as a function of temperature and applied bias.

The work performed on each of task, along with the milestone demonstration goals, is summarized in the following project tasks. Project results and discussion are organized by the project task.

2. TASK 1: FUNCTIONALIZATION OF ZN COMPLEXES FOR OPTOELECTRONICS

The goal of this task 1 was to develop and demonstrate low-cost, high performance phosphor materials and coatings for optoelectronic applications using zinc complexes produced by NanoFermentation (NF), deposited by low-temperature non-vacuum techniques, and sintered using Pulse Thermal Processing (PTP) technologies.

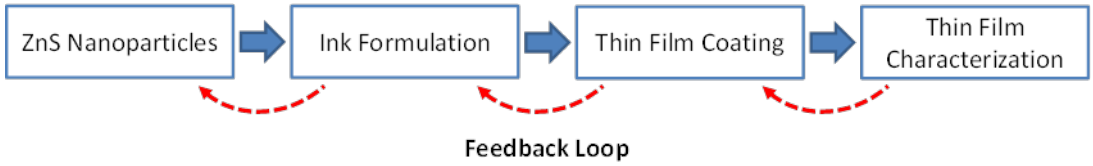

Figure 1.1. General steps in the development of NF Zn complexes for optoelectronic applications.

The overall process for the production of Zn complexes by NF and characterization of particles and thin film coatings for optoelectronic applications is summarized in Figure 1.1. Four subtasks in our development of Zn complexes for optoelectronic applications have been identified and are as follows:

- Zn complexes: The nanoparticles of Zn based complexes will be synthesized by a nanofermentation approach. The nanofermentation process will be optimized to achieve the target nanoparticle size and distribution suitable for high performance phosphor development. This subtask was pursued under the Low Temperature Materials Synthesis project of the Manufacturing Demonstration Facility (MDF).
- Ink development: The development of appropriate inks is critical for the realization of high quality thin films for optoelectronic applications. The ink development will bring together the elements of solvent, additives, modifiers, dispersants, and nanoparticles for the development of thin and thick films on suitable substrates. An important factor impacting the eventual thin film performance will be the amount of carbonaceous residue left behind from burn-out of surfactant materials and dispersants.
- Thin film coating: The thin films were deposited by ultrasonic spray deposition technique (Sonospray deposition). Pulse thermal processing (PTP) techniques will be explored for low thermal budget annealing of thin films. The impact of PTP treatment will be evaluated in terms of the microstructure, optical, and electrical properties of thin films.
- Thin film characterization: The thin films will be characterized in terms of the structural, optical, and electrical properties. The photoluminescence (PL) measurements will be conducted to establish the optical absorption and emission characteristics for optoelectronic applications.

In the following sections, the work performed on each of these subtasks is described in detail.

2.1 ZnS PRODUCTION AND CHARACTERIZATION

The details of various ZnS/CdS nanoparticle batches that were initially investigated are highlighted in Figure 1.2. The main process variables under exploration for these batches were dosing impact, incubation time, and dopant concentration. These efforts were covered in further detail in the quarterly and final reports for the Low Temperature Materials Synthesis project of the MDF.

Particle Type	Start Date	Batch	Sample Number	Sample Description	Receiver	Transfer Date
ZGT	111107	A	1	Mn (4%) doped zinc gallate (freeze dried, 1g)	Pooran, Jay	120221
ZGT	111107	B	1	Cr (1%) doped zinc gallate (freeze dried, 1g)	"	"
ZGT	111107	C	1	Co (2%) doped zinc gallate (freeze dried, 1g)	"	"
ZNS				ZnS 5 mM impact dosing, 10 day incubation (in DIW, 0.5g)	elemental S contamination : revoked	
				ZnS 0.5 mM/day dosing, 10 day incubation (in DIW, 0.5g)		
				ZnS 1 mM/day dosing, 10 day incubation (in DIW, 1g)		
				ZnS 5 mM impact dosing, 3 day incubation (in DIW, 0.5g)		
				ZnS 5 mM impact dosing, 5 day incubation (in DIW, 0.5g)		
				ZnS 1 mM/day dosing, 5 day incubation (in DIW, 0.5g)		
				ZnS 0.5 mM/day dosing, 5 day incubation (in DIW, 0.25g)		
ZNS	120220	A	1	ZnS (drop deposit on glass)	Ilia	120306
ZNS	120220	B	1	ZnS:Cu0.5% (drop deposit on glass)	"	"
ZNS	120220	C	1	ZnS Cu1% (drop deposit on glass)	"	"
ZNS	120220	D	1	ZnS Cu2% (drop deposit on glass)	"	"
ZNS	120220	E	1	ZnS Cu4% (drop deposit on glass)	"	"
ZNS	120220	F	1	ZnS Cu6% (drop deposit on glass)	"	"
ZNS	120220	G	1	ZnS Cu8% (drop deposit on glass)	"	"
ZNS	120226	A	1	ZnS 5 mM impact dosing, 10 day incubation (in DIW, 0.5g)	Beth	120319
ZNS	120226	B	1	ZnS 0.5 mM/day dosing, 10 day incubation (in DIW, 0.5g)	elemental S contamination : suspend	
ZNS	120226	C	1	ZnS 1 mM/day dosing, 10 day incubation (in DIW, 1g)		
ZNS	120226	D	1	ZnS 5 mM impact dosing, 5 day incubation (in DIW, 0.5g)		
ZNS	120226	E	1	ZnS 0.5 mM/day dosing, 5 day incubation (in DIW, 0.5g)		
ZNS	120226	F	1	ZnS 0.1 mM/day dosing, 5 day incubation(in DIW, 0.5g)		
ZNS	120226	A	2	ZnS 5 mM impact dosing, 10 day (freeze dried, into quartz cell)	Jay	120319
CDS	110602	A	1	CdS (110703 harvested, freeze dried, into quartz cell)		

Figure 1.2. Various NF nanoparticle batches investigated.

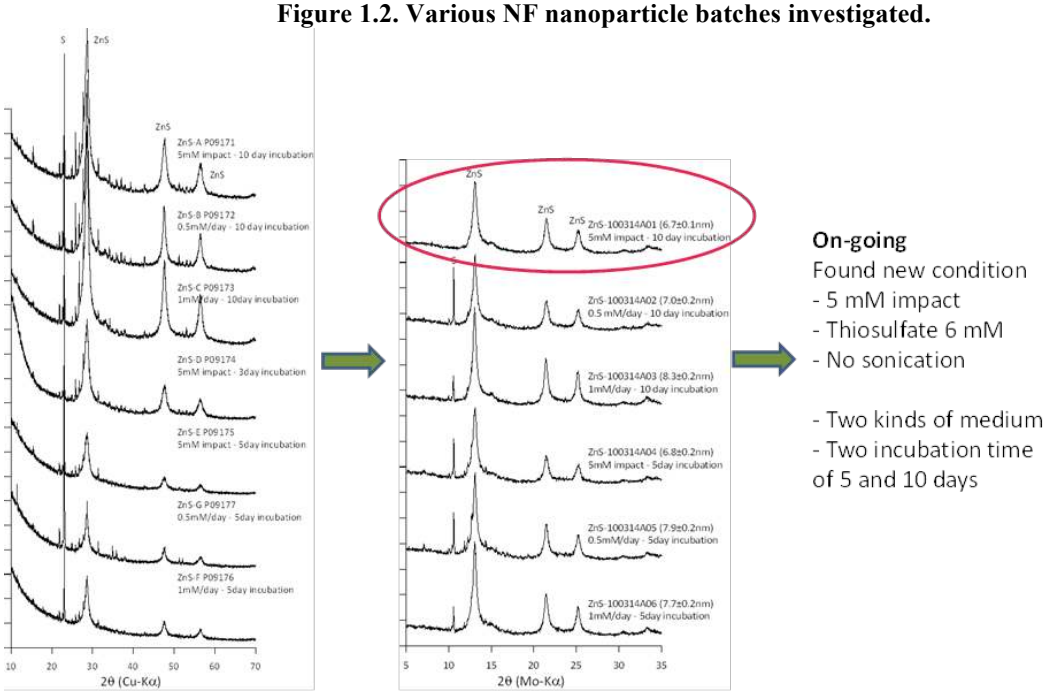

Figure 1.3. The impact of incubation time on nanoparticle growth and microstructure.

X-ray Diffraction (XRD) was used to optimize the NF process for Zn complex synthesis. Figure 1.3 shows the effect of incubation time on the microstructure of ZnS nanoparticles. As shown in Figure 1.3, the optimum process conditions result in well-defined crystalline ZnS phase. The bio-ZnS was produced by the incubation of 10 mM of glucose as electron donor, 10 mM of thiosulfate as electron acceptor and sulfur source, and 2% (v/v) mid-log growth TOR-39 at 65^{o}C. Zinc salt was dosed as a single dose injecting a total target amount of Zn salt or a discrete pulsed dose injecting a partial amount at a time with multiple times until approaching total target amount. The first batch was revoked due to co-existing of elemental sulfur (S^0) (Figure 1.2). The protocol we used had never produced elemental sulfur previously, and the reason for its production in this batch is not certain. We

then we reduced thiosulfate concentration to 8 mM. The impact of reduced concentration on the crystallinity and sulfur incorporation is shown in Figure 1.3. Elemental sulfur was detected for both single and discrete pulsed dosing at second batch (ZNS120226 series). But average crystallite size obtained from the X-ray diffraction patterns explicated that single dosing induced smaller size compared to discrete pulsed one. The batch circled in red gave the purest ZnS phase with minimal elemental sulfur.

Based on the observed x-ray diffraction results (Figure 1.3), we proceeded to make a third batch with a reduced thiosulfate concentration of 6 mM and a single dosing method. Additionally we tried a different medium composition (Figure 1.4). We found that a single dose with 10 day incubation in B-medium produced smaller size and better crystallinity ZnS nanoparticles (results circled in red in Figure 1.4).

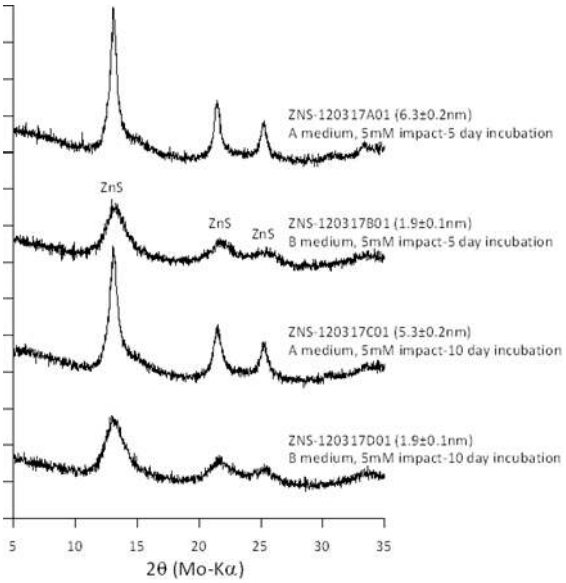

Figure 1.4. The impact of single dosing, thiosulfate concentration, and increased incubation time on ZnS nanoparticle growth and crystallinity.

2.1.1 ZnS Process Scale-up

Based on the understanding of phase formation kinetics, we scaled up to a 4L batch composed of simultaneous 4 batches of 1L medium scale (ZNS120403) and a 24L batch composed of dual parallel reactors of 12L (ZNS120426) (Figure 1.5(a)). This result showed that scaled-up nanofermentation can be advantageous in shortening the process time and saving energy. For the same synthesis condition, the 24L batch showed higher crystallinity (Figure 1.5(b)) than the 4L batch, indicating that the incubation period can be reduced without sacrificing material quality.

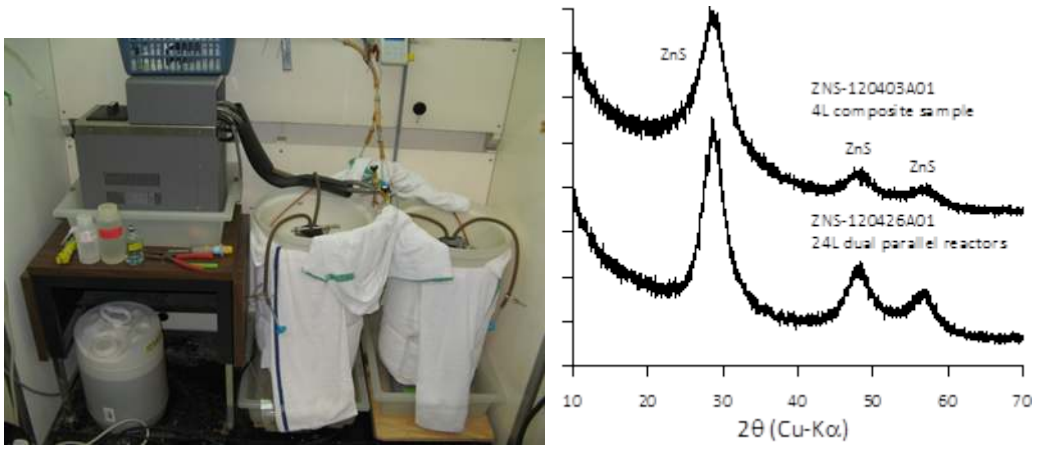

Figure 1.5. (a) Setup for process scale up, and (b) x-ray diffraction patterns indicating that phase formation kinetics are well-maintained for the scaled up process.

2.1.2 ZnS Photoluminescence Response

Photoluminescence (PL) measurements were conducted to gain further insight into the ZnS material characteristics. As shown in Figure 1.6(a), a short incubation (5 day) single dose sample exhibited the strongest PL emission. Based on the PL response, the incubation period was shortened to 5 days for the 2nd 24L ZNS120515 batch. The crystallinity of the ZnS nanoparticles was not influenced by the shorter incubation time as shown in Figure 1.6(b). The PL measurements are limited by the setup capabilities. The photon energy from our illumination light source is too small to see the fundamental excitonic PL from the ZnS nanocrystals. We used an illumination wavelength of 458 (2.71 eV), while an illumination wavelength >3.9 eV (<317 nm) is required to see the fundamental PL spectra.

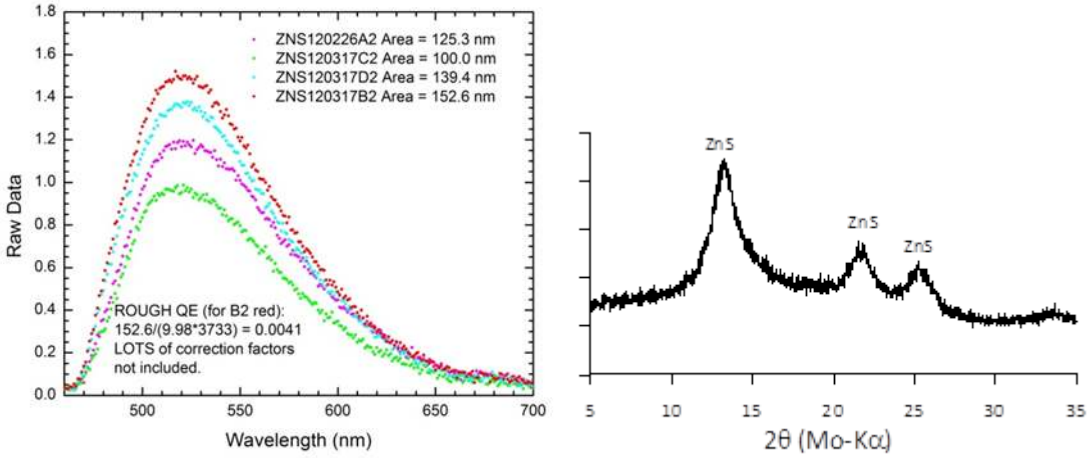

Figure 1.6. The impact of shorter incubation time on the (a) PL response for the batches shown in the figure, and (b) crystallinity of ZnS nanoparticles for batch number ZNS120515.

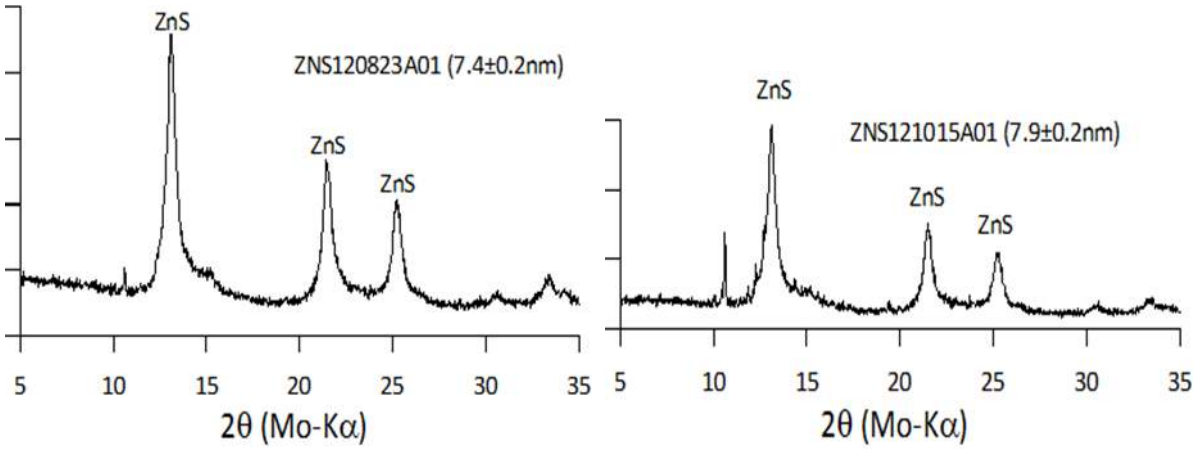

Figure 1.7. X-ray diffraction patterns of ZnS nanoparticles with estimated particle size of (A) 7.4 ± 0.2 nm and (B) 7.9 ± 0.2 nm.

In the work described above, the size of NF-produced ZnS nanoparticles was in the range of 2-3 nm (as measured by XRD). Subsequently, larger sized particle sizes (sample ZNS120823A01) were produced with estimated particle sizes in excess of 7 nm (see Figure 1.7) in quantities sufficient for PL and dispersion analyses. Sample ZNS121015A01 resulted in similar sized ZnS particles, in scaling up to 24L batch fabrication, even though that procedure had produced >12 nm sized ZnS particles when fabricated in a 50 ml batch process.

2.1.3 Nanoparticulate Solution Purification

Techniques were also explored for decreasing the organic content of the nanoparticulate solutions. Since this is a biologically-based process, it is necessary to provide nutrients for the bacteria to survive and produce the nanoparticles. During the course of this work, we postulated that the organic materials used during the nanoparticle synthesis technique were responsible for potential carbonaceous residue witnessed after thin film sintering. Therefore, various nutrient sources were investigated to reduce the organic content of the nanoparticle solutions. Table 1.1 lists a number of the nutrient materials considered and Figure 1.8 shows the effect on the optical density (turbidity) of the various samples. Three of the most promising samples (i.e. glucose, xylose, and pyruvate) were analyzed by XRD (Figure 1.9), and ZnS nanoparticle formation was confirmed for two of the samples (glucose and xylose).

Table 1.1. Nutrients evaluated for NanoFermentation of ZnS to reduce organic content

Nutrients	Formula and molecular weight
Glucose (standard)	C6H12O6, MW = 180.16
Xylose	C5H10O5, MW = 150.13
Lactate	C3H6O3, MW = 90.08
Pyruvate	C3H4O3 MW = 88.06
Acetate	C2H3O2, MW = 60.05
Formate	HCOO, MW = 45.02

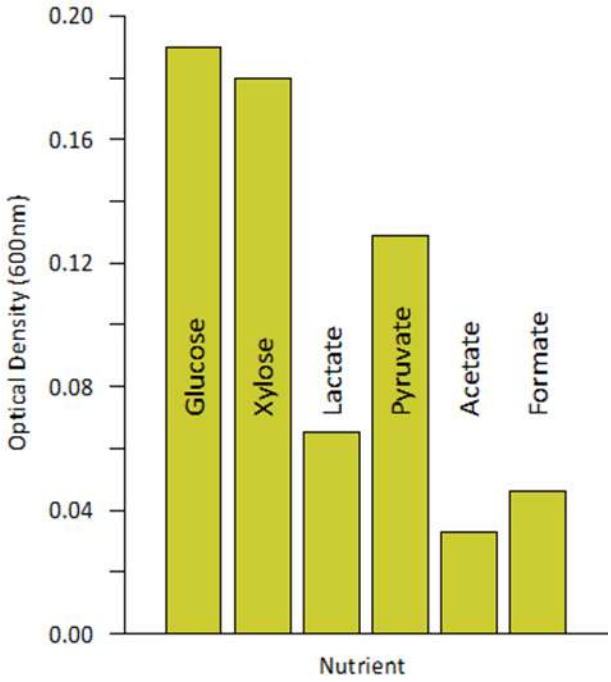

Figure 1.8. Optical density measurement of ZnS nanoparticle solutions synthesized with various nutrient sources.

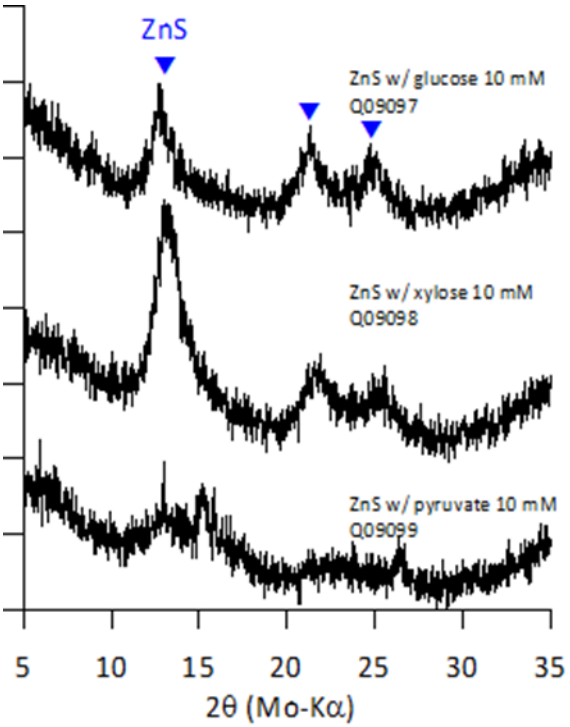

Figure 1.9. X-ray diffraction pattern of ZnS nanoparticles produced with glucose (top), xylose (middle), and pyruvate (bottom

In order to further reduce the organic content of the nanoparticle solutions, the abiotic production of ZnS nanoparticles was also explored. Instead of using bacteria, chemical and electrochemical routes were explored to provide nucleation sites and reduction potential. We demonstrated that it was possible to produce ZnS nanoparticles in degased water with the addition of Cysteine-S under careful pH control. These techniques were described in additional detail in the Low Temperature Synthesis FY2012 Q4 MDF quarterly report. The abiotic production process provided nanoparticles with increased particle sizes of up to 9.5 nm as estimated by XRD (Figure 1.10).

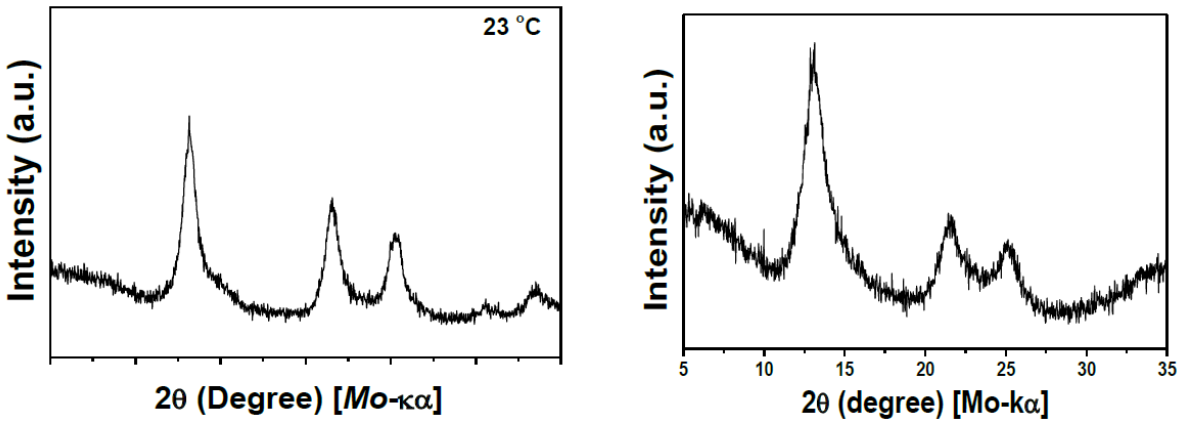

Figure 1.10. X-ray diffraction patterns of ZnS nanoparticles produced (A) abiotically and (B) biotically, demonstrating an increase in particle size from 4.6 to 9.5 nm.

The abiotic synthesis of ZnS nanoparticles also demonstrated a marked decrease in the organic content, as demonstrated by reduced organic bonding (circled portion of FTIR spectrum in Figure 1.11).

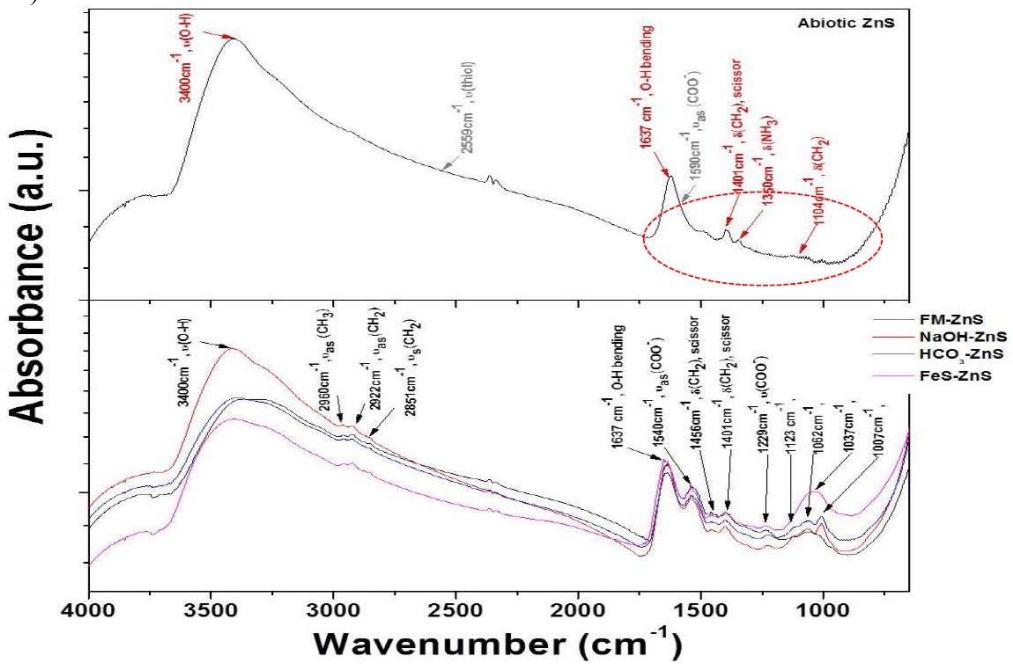

Figure 1.11. Fourier transfer infrared (FTIR) spectroscopy of abiotic (top) versus biotic (bottom) production of ZnS, showing reduced organic bonding for abiotic production.

Initial attempts to fabricate the NP ZnS resulted in agglomerates that were too large. Subsequent studies were performed to further disperse the ZnS nanoparticles in deionized water. Variables of interest during post recovery treatment included surfactant types, surfactant concentration, ZnS dispersed content, sonication method and time, and sedimentation periods. Currently, the best results have been achieved with the dispersant NTA, producing aggregates with average size ~ 120 nm (Figure 1.12).

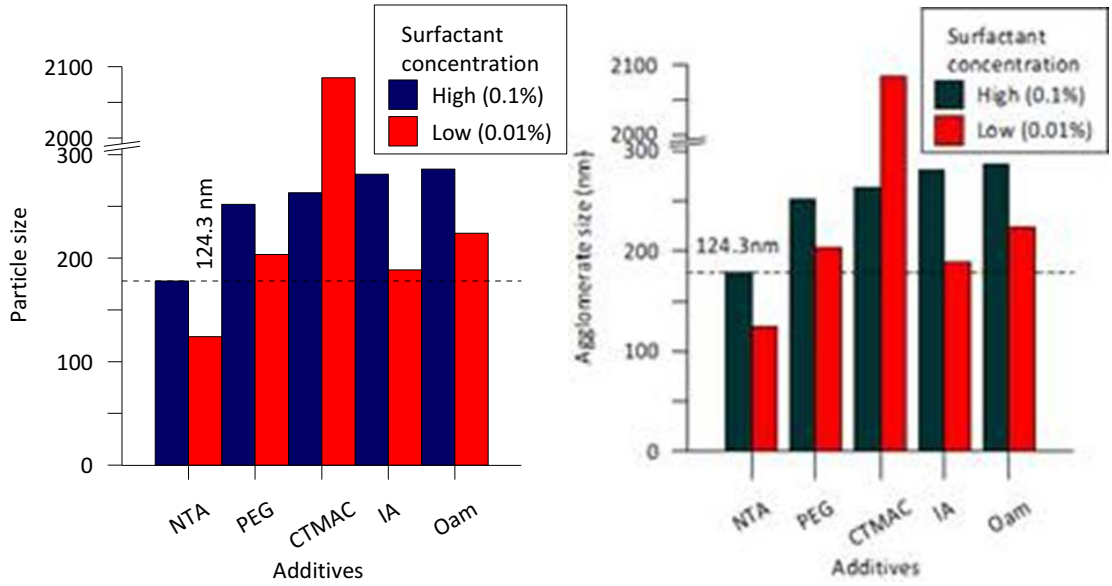

Figure 1.12. ZnS average agglomerate size after post recovery treatment with the various surfactants.

We were unable to reproduce the impressive results from earlier work (down to 25 nm), so it appears that data point may have been a measurement artifact. We also investigated ways to accomplish in-situ dispersion of the nanoparticles. Use of the dispersant thioglycerol gave almost the same aggregate size to NTA, however all dispersant candidates included in the post recovery treatment experiments gave large average crystallite sizes. Surfactant addition timing was also tested as some surfactants block microbial activity and can be used as another carbon source for the bacteria. The average sizes of the ZnS nanoparticles obtained in these studies are summarized in Figure 1.13, and show that the time of the addition of the thioglycerol made little difference on the size of the resultant ZnS particles. A second study looked at the effect of the amount and timing of the thioglycerol on the size of the ZnS agglomerates. The results shown in Figure 1.14 indicate again that timing is relatively unimportant, but there is a small decrease in ZnS agglomerate size with increasing thioglycerol concentration.

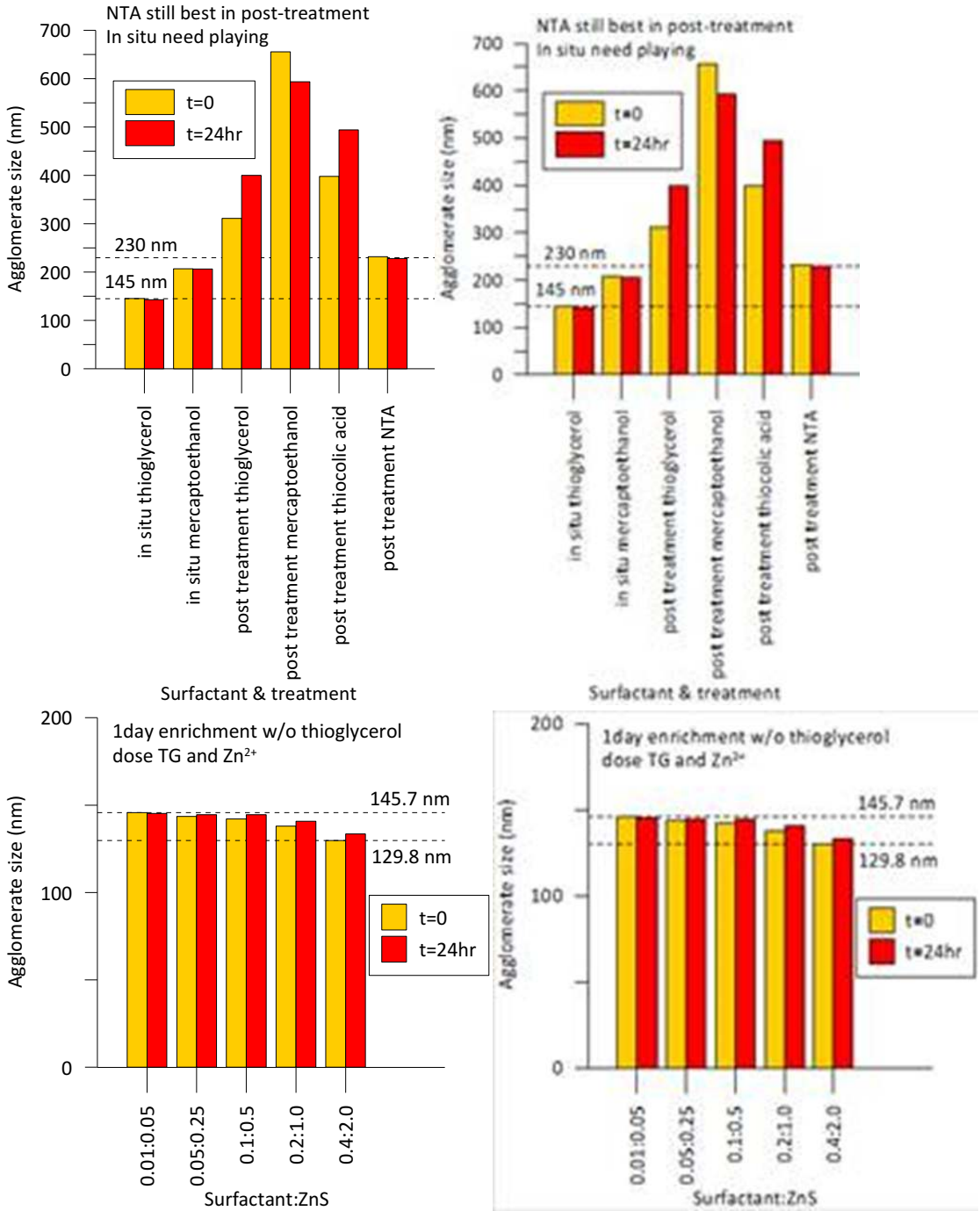

Figure 1.13. (right) ZnS average agglomerate size for various in-situ versus post recovery treatments.

Figure 1.14. ZnS agglomerate size Comparison study for in-situ treatment according to dosing.

The measured ~120 nm aggregate size of biologically produced ZnS nanoparticles is supported by the other study reported in the literature (Moeau JW, Weber PK, Martin MC, Gilbert B, Hutcheon ID, Banfield JF. "Extracellular proteins limit the dispersal of biogenic nanoparticles." Science 2007; 316: 1600) that showed that aggregation of 3 nm inorganically produced ZnS particles, capped with an amino acid, initially occurred rapidly to form 100 nm diameter aggregates. The growth rate of the aggregates subsequently slowed greatly or ceased after one week. A minimum aggregate size of

around 100 nm from many dispersion cases, and several of these aggregates were examined by surface characterization.

All samples were studied using FT-IR, regardless of the medium (mostly buffer) used to disperse the ZnS particles. These studies clearly showed that the samples contained organic matter as indicated by $\nu(CH_2)$ and $\nu(CH_3)$ groups at 2960 cm^{-1}, 2922 cm^{-1}, and 2851 cm^{-1}, and scissor modes of CH_2 at 1456 cm^{-1} and 1401 cm^{-1} (Figure 1.15a). The spectra from all the samples seemed to be related to $–COO^-$ groups, as featured by $\nu(COO)$ at 1540 cm^{-1} and 1229 cm^{-1}. XPS spectrum (Figure 1.15b) also clearly exhibited the dominant hydroxyl carbon (C–O, 286.2 eV) and carbonyl carbon (C=O, 287.5 eV) peaks. Another spectrum (Figure 1.15c) exhibited a prominent peak at ~ 399.5 eV, that most likely belonged to amine ($–NH_2$) and a smaller peak at ~ 402.1 eV which could be a protonated form of the amine. These observations supports the idea that the final end products of fermentation included lactate and acetate as well as microbially derived extracellular protein, including amine and carboxylic acids, which most likely facilitated, not only keeping the average nano sized dimensions of the crystallite ZnS nanoparticle, but also increased the particle aggregation.

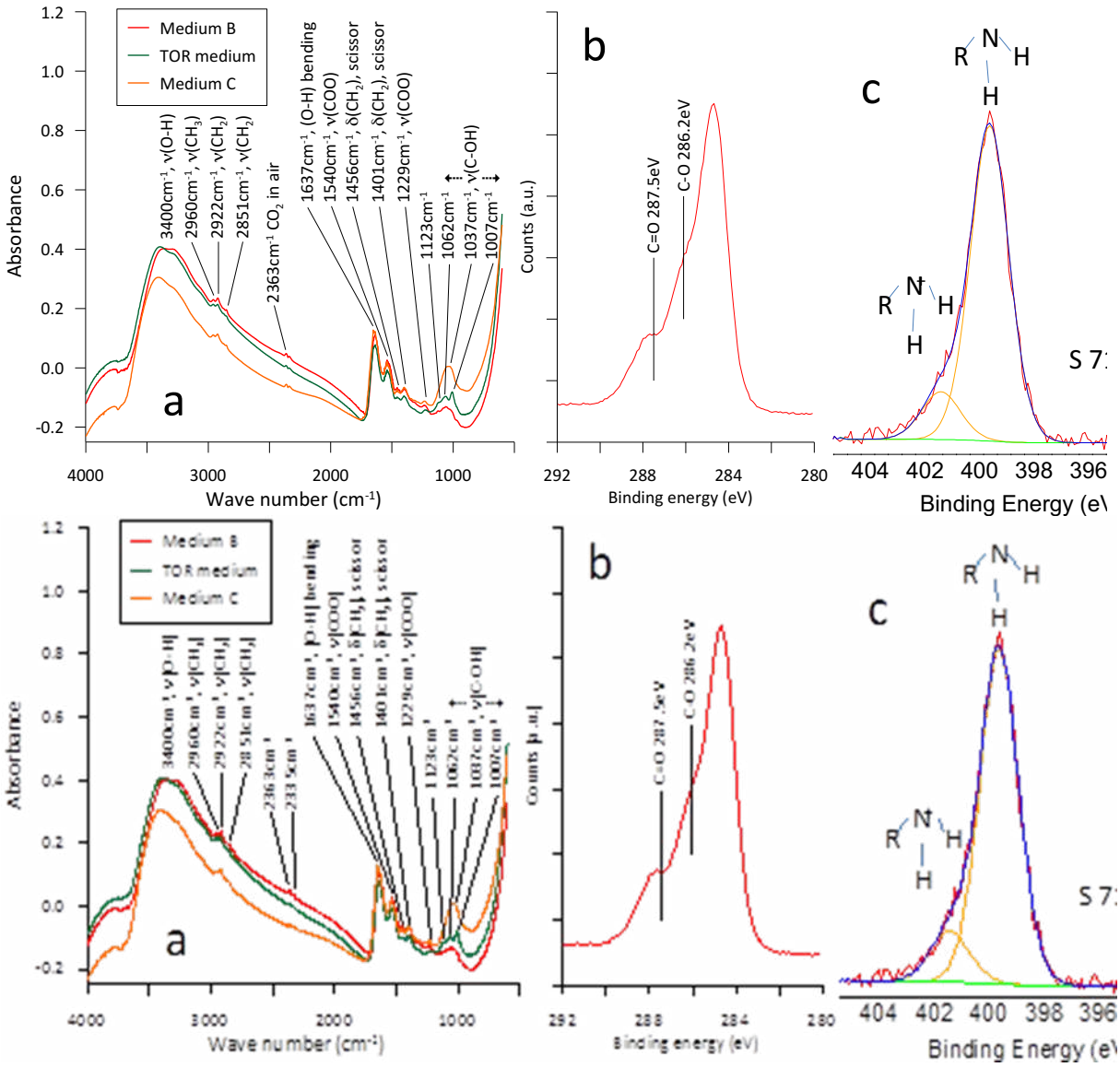

Figure 1.15. FT-IR spectroscopy and XPS measurement of the surface of NP ZnS formed by *Thermoanaerobacter* X513. (a): FT-IR spectra of the NP ZnS using various buffer systems; (b), XPS spectrum showing C–O and C=O bonding; (c), XPS spectrum showing amine (-NH_2) and protonated amine bonding

2.1.4 Zn Gallate Manufacturing and Characterization

The primary effort within this subtask is focused on the production of colored phosphor nanoparticles by doping different metals into the zinc gallate host structure, as well as evaluating their optical properties as a function of the various post fabrication treatments. The initial work in this task is focused on the fabrication of various colored phosphors, which could produce red, green, and blue (RGB) emissions using small 10mL reactor vessels. This effort was subsequently scaled up from 10 mL to 2L culture bottles – a 200x increase in scale. The next step was to scale production of the phosphors using several 12L carboy reactor vessels, which represented a 2,400x scale-up from the initial 10mL test tube production capabilities. The reactor vessels used in each of these scale-up experiments are shown in Figure 1.16. After one week of incubation, the phosphors were washed in deionized water and freeze dried.

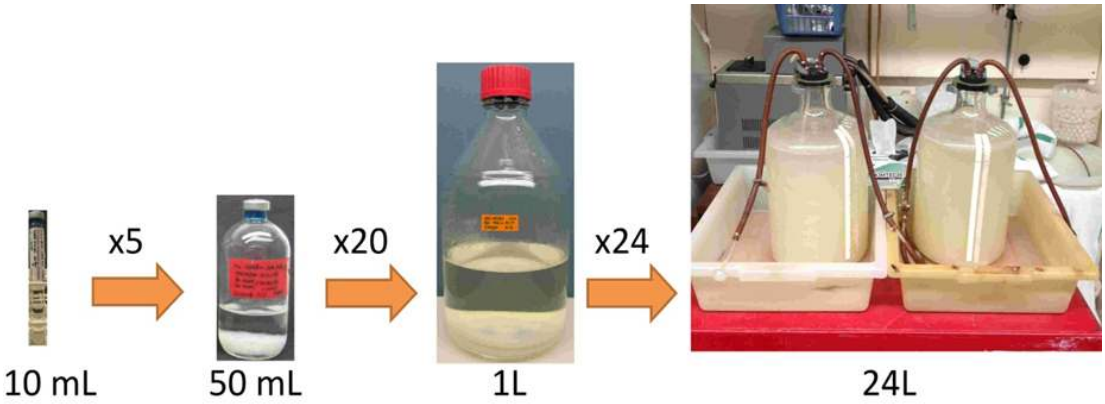

Figure 1.16. Scale up of NanoFermented phosphor production with scale factor of 100.

Table 1.2. Experiments performed to prepare the wet and dried nanoparticle phosphors

Sample	Description
ZGT120529A01	Using precursor with Co 1% replacing Zn, freeze dried 1.686g/3L for BLUE
ZGT120529B01	Using precursor with Mn 4% replacing Ga, freeze dried 2.015g/3L for GREEN
ZGT120529C01	Using precursor with Cr 1% replacing Ga, freeze dried 1.875g/3L for RED
ZGT120711A01	Using precursor with Mn 4% replacing Zn, freeze dried 1.574g/2L for GREEN
ZGT120711B01	Using precursor with Mn 4% replacing Zn with Gallium Nitrate Hydrate, freeze dried (0.897g/L) for GREEN
ZGT120614A01	Using precursor Co 1% replacing Zn, 6.7% solution in water
ZGT120614B01	Using precursor Mn 4% replacing Ga, 5.6% solution in water
ZGT120614C01	Using precursor Cr 1% replacing Ga, 6.3% solution in water
ZGT120626A01	Using precursor Mn 4% replacing Zn, 7.9% solution in water

In the initial small-scale experiments, Co-doped zinc gallates produced a blue emission, Mn-doped zinc gallates (where the Mn replaced either the Zn or Ga in nominal mole fraction in precursor composition) produced a green emission, and Cr and Eu doped zinc gallates (where the dopant replaced the Ga) produced a red emission. Simple blending of Co for blue, Mn for green, and Cr for

red resulted in doped zinc gallates that produced white light.

In follow-on experiments, we focused on Co replacing Zn for blue, Mn replacing Zn rather than Ga (due to yield), and Cr rather than Eu (due to higher price of rare earth elements) replacing Ga precursors and their phosphor production. A FeS medium, which was used for ZnS synthesis in the first year of the project, was incubated with 10 mM of glucose and 2% mid-log growth thermophilic bacteria (Tsp). After 24hr, the Zn with a 2.5 mM dopant and Ga with a 5 mM dopant with the same volume of 1.5M MOPS buffer were dosed, and then incubated for one week. Table 1.2 summarizes the experiments that were performed to fabricate the RGB phosphors.

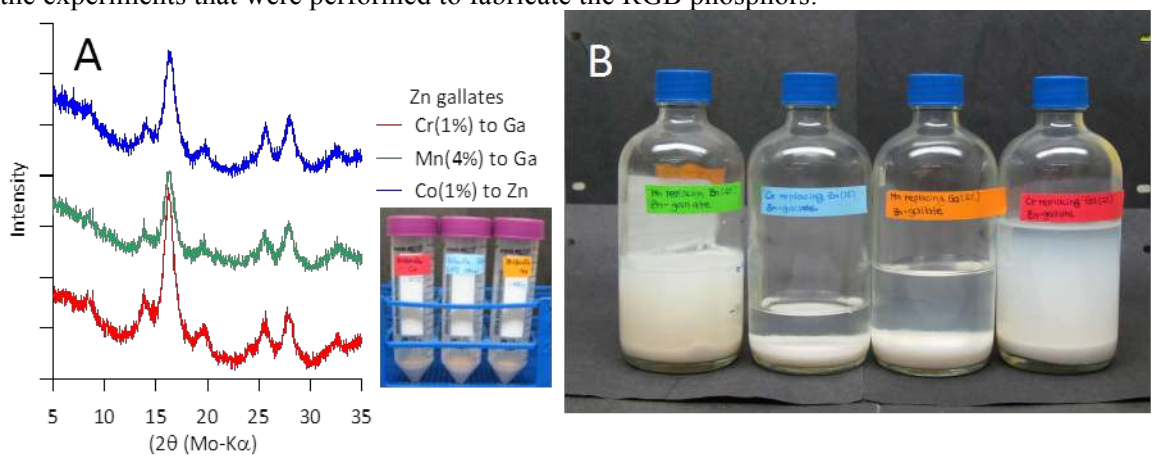

Figure 1.17. XRD patterns from representative RGB Zn-gallate phosphor before post-treatment.

Gallium nitrate was also used in some experiments as the precursor chemical for the formation of Zn gallate instead of the more conventional gallium chloride. Some representative samples were analyzed and the XRD spectra shown in Figure 1.17. The finding that metal-doped zinc gallate formation was possible using the adjusted pH-Eh micro-environment mediated by microbial activity, without reducible metal or non-metal components in the system, was a unique approach to phosphor production. Consequently, ORNL filed this as US Patent Application Number 61/644,211 (2012) on May 8, 2012 and filed this as international patent application (PCT) on March 14, 2013.

Table 1.3. Agglomerate Size Results for the Zinc Gallate Study

		Sizes (μm)				Sample
Modification	Sonicated		Diameter on Cumulative %			ID Number
		Mean	10%	50%	90%	
Co replacing Zn (1%)		6.77012	3.2581	6.3241	10.8869	ZGT120614A01
Co replacing Zn (1%)	Yes	4.69867	1.8551	4.3382	7.9792	ZGT120614A01
Mn replacing Ga (4%)		8.70829	4.7768	8.1905	13.2274	ZGT120614B01
Mn replacing Ga (4%)	Yes	6.39268	3.1200	6.0089	10.1463	ZGT120614B01
Cr replacing Ga (1%)		7.26818	3.5818	6.8082	11.5189	ZGT120614C01
Cr replacing Ga (1%)	Yes	5.44319	2.2125	5.0333	9.1934	ZGT120614C01
Mn replacing Zn (4%)		7.21283	3.5240	6.7367	11.4930	ZGT120626A01
Mn replacing Zn (4%)	Yes	4.95120	1.7619	4.4794	8.7174	ZGT120626A01

The experiments to produce NF zinc materials produced particles that were highly agglomerated with particle sizes in the 10 micron size range. A significant effort was pursued to reduce the size of the agglomerated NF zinc materials using sonication techniques. These experiments and the analyzed particle sizes are summarized in Table 1.3.

Additional efforts were focused on integrating dispersant agents into the Nanofermentation synthesis process in order to reduce agglomeration and limit organic contamination. A detailed description of these efforts can be found in the Q1 FY2013 Low Temperature Materials Synthesis project of the MDF quarterly report.

Each of the RGB color phosphors was produced under identical process conditions in a 24 L growth medium (Figure 1.16). All samples resulted in the similar average crystallite size at around 2-3 nm calculated by X-ray diffraction patterns (Figure 1.18). Also, the crystallinity of each RGB color phosphor was found to be inversely proportional to the ionic toxicity of the doping metals. The low toxicity of doped manganese compared to cobalt and chromium exhibited the highest crystallinity, even though doping amount was high at 4% compared to 1% cobalt and 1% chromium.

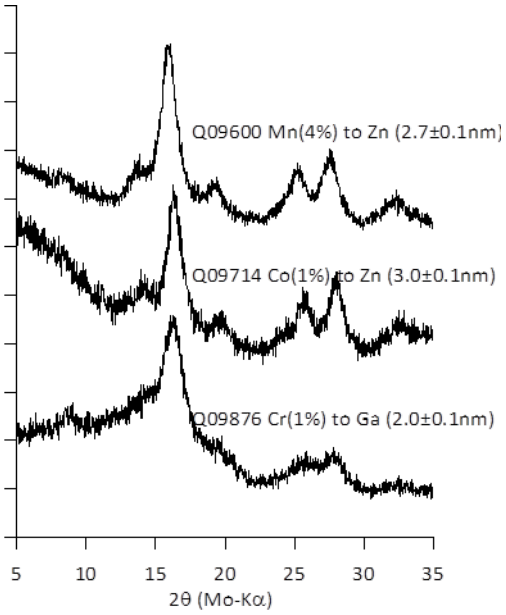

Figure 1.18. X-ray diffraction patterns for each of the RGB color phosphors produced in the 24L reactor.

Table 1.4 Stock solution compositions

Final Input (M)			
Zn (M)	Mn (M)	Ga (M)	Total (M)
0.187	0.008	0.556	0.75
0.206	0.009	0.536	0.75
0.223	0.009	0.517	0.75
0.240	0.010	0.500	0.75
0.255	0.011	0.484	0.75
0.270	0.011	0.469	0.75
0.284	0.012	0.455	0.75

Earlier work on the project found that the photoluminescence of zinc gallate samples showed some variance in that starting the incubation with all ingredients and bacteria at initial and shorter incubation periods resulted in better photoluminescence. Another variable is the stoichiometry of the precursor solution to enhance photoluminescence. Previous elemental analysis of final product using a Zn:Ga =1:2 stock solution was found to be very close to 1:2. Therefore we tuned 30% zinc variation with 10% increment from Zn:Ga ratio ($Zn_{1\pm0.3}$:Ga_2). The goal was to achieve Mn 4% doped

zinc gallate, which exhibited the highest green emission. Stock solutions were prepared at 4% Mn-doping (see Table 1.4) and incubated with 10 mM glucose, 2% mid-log growth bacteria stock solution, total 7.5 mM stock solution, and additional MOPS buffer to keep the pH between 7.5-8.0. Figure 1.19 show samples of nanofermented zinc gallate precipitates.

Figure 1.19. NanoFermented zinc gallate precipitates.

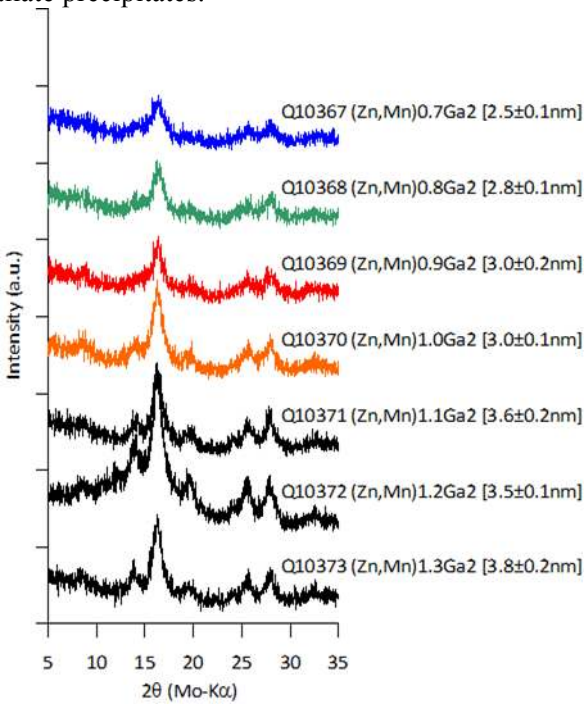

Figure 1.20. X-ray diffraction patterns of zinc gallates using various ([Zn]+[Mn])/[Ga] ratios.

2.1.5 Zn, Sn, Ni, Co and Cu Sulfide Manufacturing

Four additional metal sulfides were studied; namely SnS, Ni_3S_4, CoS_2, and CuS. These nanoparticles were produced using a 24 liter scale production capability. In order to achieve the 24 liter reaction scale, 12 liters of growth medium was added to two 13.25 liter glass carboys. The carboys were equipped with ventilation ports in the headspace and were autoclaved for a period of 2 hours. The carboys were subsequently cooled to 70 °C in the autoclave. The samples were further cooled with continuous purging using N_2 gas through a 0.2-micron filter overnight and put into plastic containers, which were connected to a 65 °C water bath. Figure 1.21 shows examples of samples of metal sulfides (SnS, Ni3S4, CoS2, and CuS) produced in the 24 liter reactor, which will be used to fabricate our thin films metal oxide gas sensors.

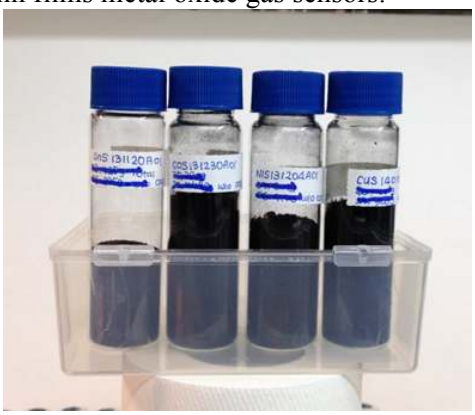

Figure 1.21. (a) Examples of samples of metal sulfides (SnS, Ni_3S_4, CoS_2, and CuS) produced in our 24 liter reactor. These will be used to fabricate thin films metal oxide gas sensors. (b) SnS and Ni_3S_4 samples.

The 100 liter anaerobic reactor produced >50 g of ZnS during the first batch run. The actual amount of ZnS produced during this process was ~ 62 g and the crystallite size was about 4.9 nm. This was very important for the scale up efforts required to achieve large amounts of NF-nanoparticles. The potential for using nanofermentation to produce nanoparticles without any effects on the size of the nanoparticles is crucial for both optoelectronics and sensor applications.

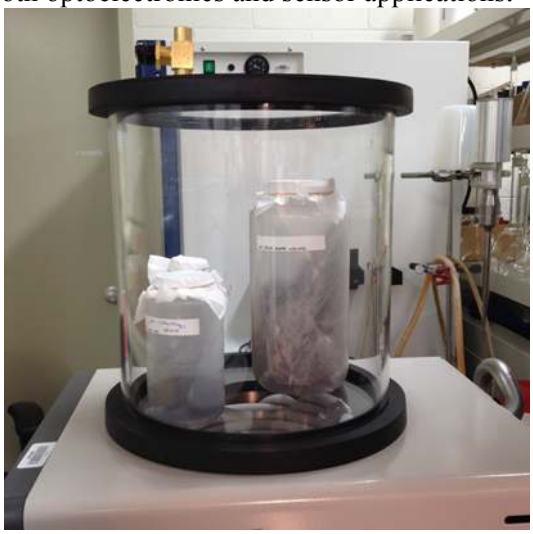

Figure 1.22. Freeze drying condensed zinc sulfide sample at >50g amount from the 100 liter reactor.

2.1.6 Metal Oxide Coatings by Nanofermentation Route

The final subtask is focused on the development of metal oxide coatings using n-type ZnO and p-type NiO nanoparticles synthesized by nanofermentation (NF) bioprocessing method.

2.1.6.1 ZnO coatings and thin films

To improve the ZnO coating quality, different capping agents and post-washing treatments were investigated. The surface capping agents were expected to enhance particle agglomeration control during synthesis and increase ink loading without compromising ink quality. The post-washing treatments were aimed at elimination of surface groups controlling particle agglomeration and dispersion.

The ZnO thin films have been developed by pulsed laser deposition technique using a ZnO target processed from NF ZnO particles. The ZnO thin film performance has been evaluated in terms of the structural, optical, and electrical characteristics.

The Low Temperature Materials Synthesis team supplied us with another batch of ZnS (>20g) precursors for sensor as-synthesized. These precursors can be also be converted to ZnO through a controlled annealing process. Two zinc sulfides samples (Figure 1.23, right two samples) were newly synthesized and compared to the other two samples (Figure 1.23, left two samples) synthesized from a continuous batch using MOPS buffer and multiple batches involving HEPES buffer. After harvesting and freeze-drying the appearance of the latest samples exhibited a brighter color on the surface than previously produced samples. This nanofermentation process required only a 24 hour

reaction period which indicates that the modified production protocol with the reduced reaction time can play a role in improving the production rate.

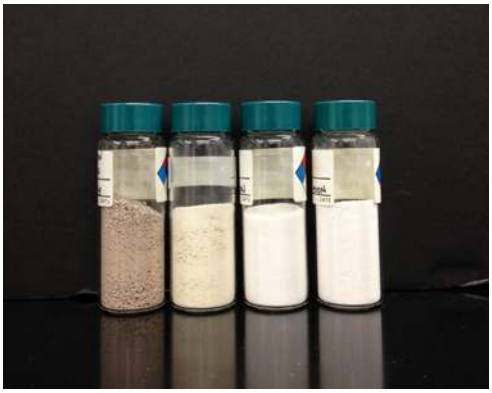

.

Figure 1.23. The latest batch of ZnS NF-nanoparticles produced in the Low Temperature Materials Synthesis project.

2.2 INK DEVELOPMENT

The nanoparticle ink development task involved the following critical steps:

→ Characterization of the ZnS nanoparticle (NP) surface
→ Identification of Sonospray deposition requirements and translate into nanoparticle properties and ink characteristics required for successful deposition
→ Defining the amount of NPs required for deposition and ink development studies
→ Determining range of Sono-spray solution solids loadings for NPs
→ Identification of potential additives to adjust dispersion, flow requirements, processing aids, etc., of ink formulation without contamination of final thin film

The initial task work on this project, involved the purchase of commercial ZnS nanoparticles (~10μm size), which were used as a baseline reference to determine applicable solvent chemistry and approximate coating quality for micron-sized particles. The following steps were initiated in the characterization of commercial and NF ZnS raw material for ink development:

- Establishing powder size distribution and surface chemistry
- Measuring nanoparticle size
- Determining the zeta potential
- Measuring the surface area

The initial candidate dispersants for NF ZnS were evaluated based on the following characterization of commercial and NF powders/solutions:

- Sedimentation
- Zeta potential
- Rheology

2.2.1 Commercial ZnS Zeta Potential Results

The zeta potential of a system is a measure of charge stability, and controls all particle-particle interactions within a suspension. Measuring the zeta potential of particles in suspension is used to predict stability and behavior when exposed to changes in ionic strength of the solution. When

nanoparticles are suspended in a fluid, zeta potential maintains the dispersion or discreteness of the particles in suspension. Understanding zeta potential is of critical importance in controlling dispersion and determining the stability of a nanoparticle suspension, i.e. to what degree aggregation will occur over time. The zeta potential is the measure of the electric potential at the slip plane between the bound layer of diluent molecules surrounding the particle, and the bulk solution. This can be closely linked to the particle's surface charge in simple systems, but is also heavily dependent on the properties of the diluent solution. A higher level of zeta potential results in greater electrostatic repulsion between the particles, minimizing aggregation/flocculation. The nanoparticle ink development was carried out in close correlation between zeta potential and pH of the ink. Figure 1.24 shows the initial results on commercial ZnS particle based ink. First results indicated that a cationic dispersant, such as polyethyleneimine (PEI), appears to be a good candidate for the sedimentation studies (Isoelectrical Point (IEP) is ≤ 4).

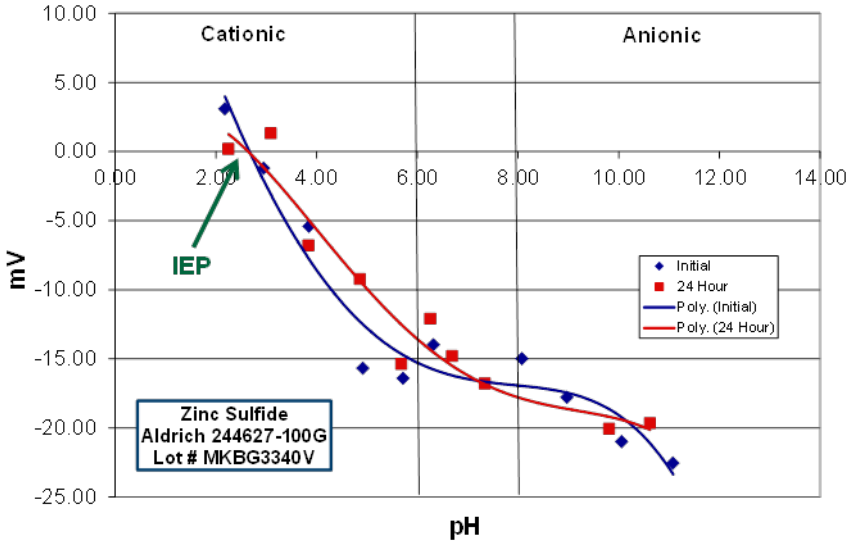

Figure 1.24. Relation between the zeta potential and pH of the ink using polyethyleneimine.

2.2.2 Dispersion of NF ZnS Particles

The development of a NF derived ZnS slurry was built on the zeta potential characterization that was completed on commercially produced ZnS powder. These results showed that the commercially derived ZnS had an Isoelectrical Point (IEP) ~ 3. As the NF ZnS is received in a solution of water, and assuming the surfaces of the commercially derived and NF ZnS will be similar to each other, suspension of the NF ZnS in this solution was facilitated by the use of a cationic dispersant. To balance the size of the NF ZnS with an equivalent molecular weight (MW) of a typical cationic dispersant, three low molecular weights were selected. An effective way to quickly evaluate the stability of powders in solution is a sedimentations study. Simply, the sediment height is measured as a function of time. The longer powders stay in the suspension without settling, the more stable the suspension. Dispersants can be added to the solutions to examine the efficacy of the dispersant as well as study the effect of the ratio of the dispersant to the solids by weight. For the NF ZnS sedimentations studies, 600, 1200, and 1800 MWs of polyethyleneimine (PEI) were selected. In general, polyethyleneimine (PEI) was able to suspend NF ZnS at a minimum concentration over a 24-hour period. The settling curves and the minimum concentrations for 600, 1200 and 1800 MW are shown in Fig. 1.25 through 1.27 with concentrations of 51, 36, and 37%, respectively. NF ZnS slurries were provided for evaluation in the coating studies for each of these minimum concentrations.

In these studies, dilute (~1 wt% solids) NF ZnS slurries were developed utilizing a cationic dispersant polyethyleneimine (PEI). Film formation of the dilute slurries showed several developmental issues that still needed to be addressed. The dilute nature of the slurries did not allow for dense film formation upon heat treatment. Slurries with higher solids loadings were required. In addition, there was concern that the high concentrations of PEI used relative to the actual solids of ZnS were leaving behind a carbonaceous ash upon heat treatment. As a result of that concern, the focus for the next stage if the work was to determine the level of ash left behind from the PEI, determine if it was detrimental to the final film formation, and in parallel search for an alternative dispersion approach for the PEI.

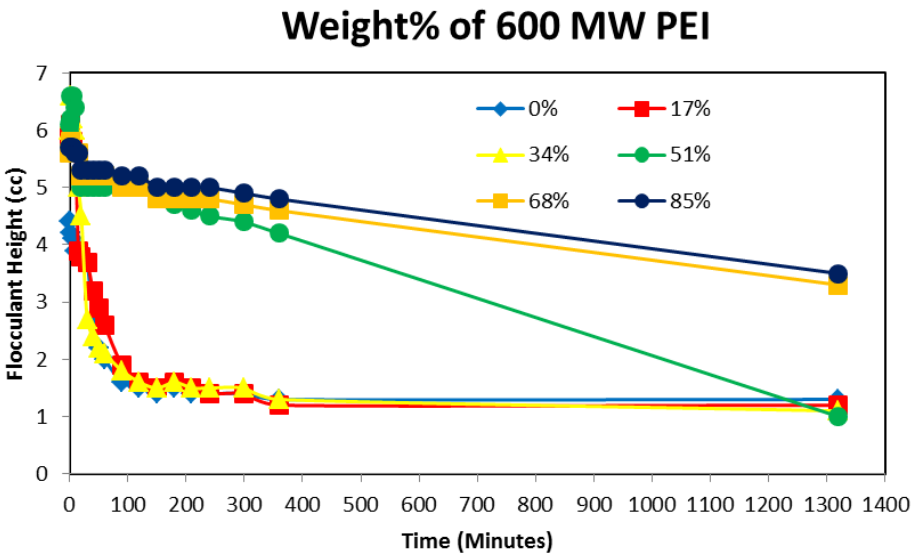

Figure 1.25. Sedimentation Curve for Additions of 600 MW PEI in an Aqueous Solution of 1 weight % NF ZnS.

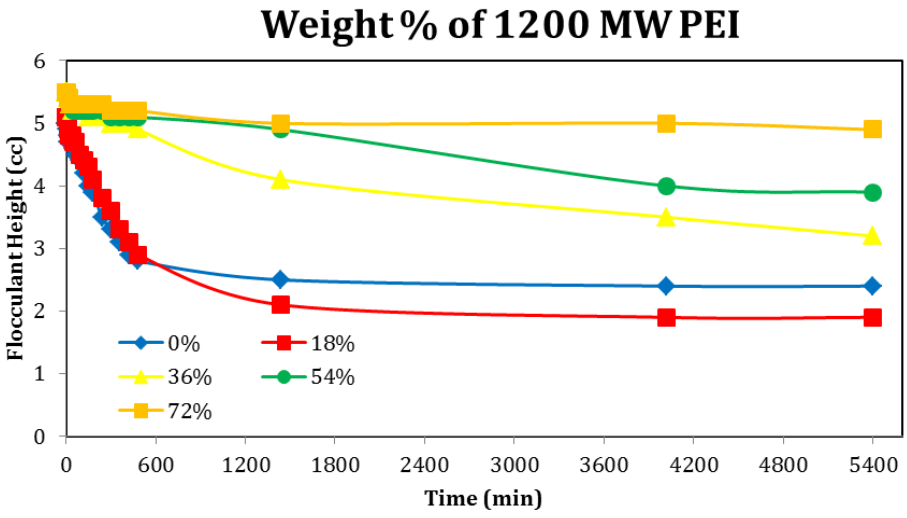

Figure 1.26. Sedimentation Curve for Additions of 1200 MW PEI in an Aqueous Solution of 1 weight % NF ZnS.

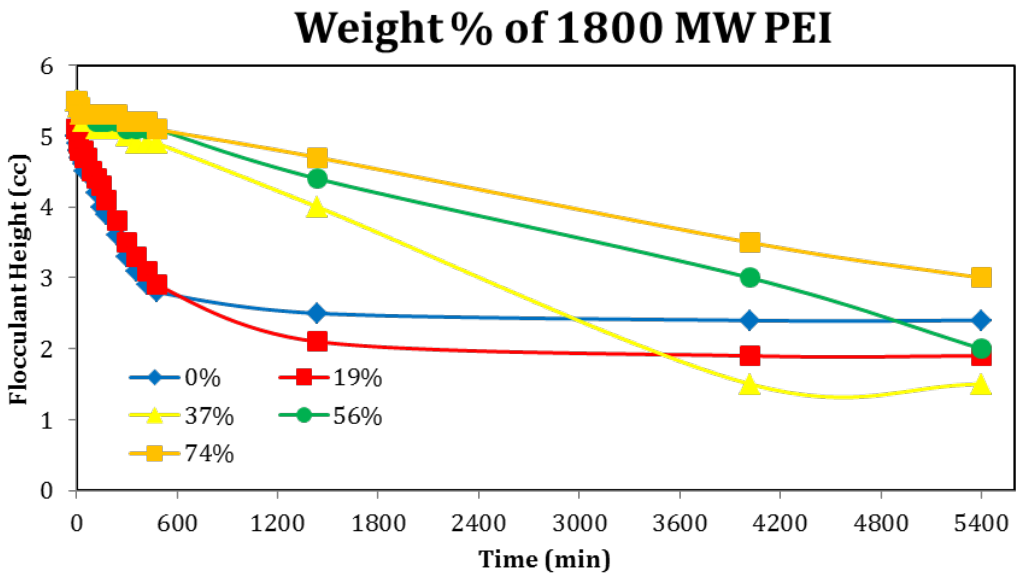

Figure 1.27. Sedimentation Curve for Additions of 1800 MW PEI in an Aqueous Solution of 1 weight % NF ZnS.

To determine the amount of carbonaceous material on the surface of the ZnS particles, thermal gravimetric analysis (TGA) was run in both air and argon environments of slurries of both stabilized and unstabilized (as-synthesized) NF ZnS slurries. Figures 1.28 and 1.29 show the weight loss curves as a function of temperature in air and argon, respectively. There were differences in the weight loss depending on whether the sample is heated in air or in argon. When argon was used, the major weight loss occurs between 200°C and 400°C. Also there was additional weight lost above 800°C and the rate was increasing as the temperature increased above 800°C. There was no heating above 1000°C, nor hold at 1000°C, so the final weight loss in argon was not determined. When air was used, the "as received ZnS" had weight loss between 200-400°C and again between 550 and 650°C. The overall weight loss was about 34%. Above 800°C there was a slight weight gain – not a weight loss as exhibited when run in argon. The samples containing the PEI dispersant exhibited several regions between 200 and 700°C where the rate of weight loss reached maximum values. What can be seen in both weight loss curves irrespective of atmosphere is that there is carbonaceous material present on the surface of the as-synthesized powders. This is residue from the fermentation process, which motivated the efforts described above to reduce the organic content. The full effect of this excess carbon was examined more closely to determine if it impacted the processing or electronic properties in the final film. In addition, the high temperatures required to remove the PEI and the amount of ash remaining after heat treatment due to the large amounts of PEI utilized to stabilize the slurry may also be detrimental to final electronic properties. As a result, alternative approaches to stabilization were examined.

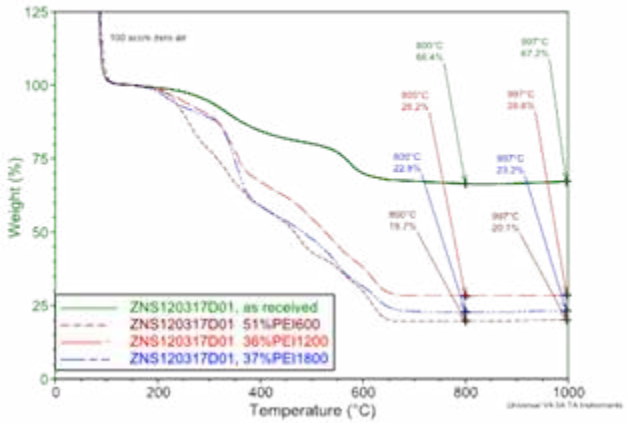

Figure 1.28. Weight loss cures of NF ZnS solutions in air with and without the use of the dispersant PEI.

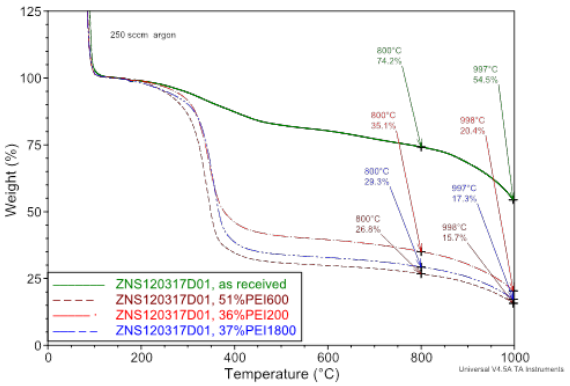

Figure 1.29. Weight loss cures of NF ZnS solutions in argon with and without the use of the dispersant PEI.

Initially, zeta potential of commercial ZnS powders (Aldrich) was characterized while waiting for the NF ZnS solutions to be ready. Stabilization approaches were based on the results of the commercial powder. As larger quantities of the NF ZnS solutions became available for characterization, the zeta potential was re-measured using the NF materials. The zeta potential comparison between the two powder sources is shown in Figure 1.30. The Aldrich ZnS has a very low isoelectric point requiring a cationic dispersant for stabilization whereas the NF ZnS's isoelectric point is higher. The NF ZnS still can utilize a cationic dispersant, but an anionic dispersant could also be used due to the more neutral value of its isoelectric point. It is believed the difference in the isoelectric point is due to the carbonaceous material seen on the surface of the ZnS powder from the TGA experiments.

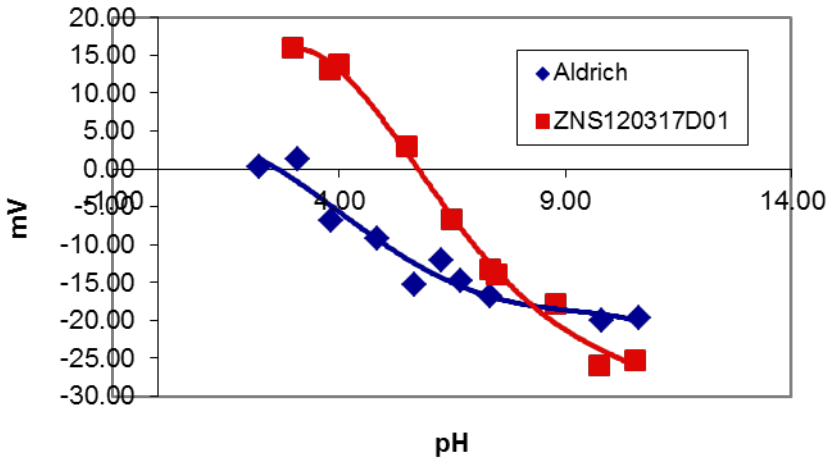

Figure 1.30. Zeta potential curves of commercial and NF ZnS powders.

To evaluate the effect of charge stabilization versus steric stabilization (pH control versus the use of a polymeric dispersant), a sedimentation study was conducted where a NF ZnS slurry pH was left

unadjusted (control), adjusted to a pH of 3 or 10 and the addition of 1 wt% oleic acid by solids weight was added. Oleic acid was chosen as a replacement dispersant for PEI due to its low burnout temperatures (<300°C). The resulting sedimentation behavior as a function of time is shown in Figure 1.31. The charge stabilized conditions, pH 3 and 10, were ineffective in preventing powder settling even over short time periods. Oleic acid seemed to be a slight improvement over natural solution.

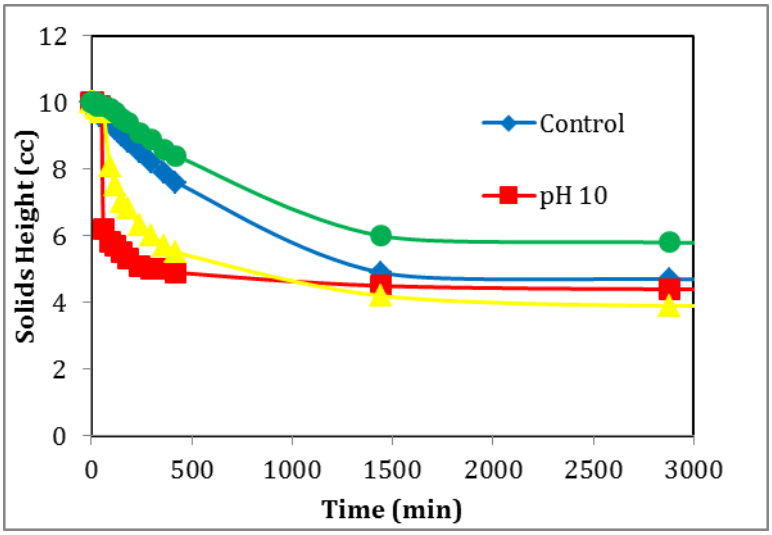

Figure 1.31. Sedimentation curve for alternative dispersion approaches for NF ZnS in an aqueous solution.

These dispersion studies of the NF zinc sulfide powders showed oleic acid to be a slight improvement in sedimentation studies as a candidate replacement dispersant for PEI. PEI, although effective, is burned out, i.e., removed by heating and the subsequent break down and volatization of the organic material, at relatively high temperatures (>400 C). To maintain the nanoparticulate nature of the starting materials by limiting heat treatment temperatures that might promote grain growth and reduce the opto-electronic properties of the final film, a search was initiated to identify dispersants that may decompose at lower temperatures than PEI.

Initially, a 10% by weight solution of NF ZnS was used as the base for the dispersant studies. A wide variety of candidate dispersants were selected and evaluated for effectiveness. The dispersants were chosen based on decomposition temperature and/or compatibility to the starting chemistry. Each candidate was added to an aliquot of the base ZnS solution, mixed ultrasonically, and the resulting particle size of the solution was measured using a laser light scattering technique. Generally, if the average particle size (D50) was minimized, and the total size distribution was tight (the minimum range from the D10 to the D90), the dispersant was flagged for further consideration. Table 1.5 shows the results from the initial dispersant particle size study. The dispersant Triton X-100 (polyethylene glycol octyphenyl ether) showed the best improvement and the tightest spread in particle size overall, but as this technique was used just for preliminary screening, four additional dispersants from this group of 13 were selected for further study. They were ethylenediaminetetraacetic acid (EDTA), nitrilotriacetic acid (NTA), glycine (GLY), and sodium lignosulphonate (Lignotech Vanisperse CB). Polyethylene glycol (PEG) and oleic acid were also included.

Table 1.5 Particle Size Results for NF ZnS Dispersant Screening Study

Chemical Name	Mean Size (µm)	Diameter on cumulative 10%	Diameter on cumulative 50%	Diameter on cumulative 90%
Glacial Acetic Acid	1.42591	0.6884	1.2828	2.3318
Alginic Acid Sodium Salt	2.62987	1.0266	2.2449	4.7957
Aquazol 200	0.75057	0.2550	0.6401	1.3803
EDTA	1.02373	0.1903	0.3009	2.9656
EDTA Disodium Salt	52.62920	0.2844	55.6674	107.4003
EDTA Magnesium Disodium Salt	1.50506	0.7352	1.3327	2.4741
Glycine	18.85070	0.7870	2.2372	87.6004
Isopropyl Myristate	1.1479	0.4397	0.9921	2.0257
Lignotech Vanisperse CB	0.68462	0.1935	0.2981	1.3157
Nitrilotriacetic Acid	0.44343	0.1624	0.2417	0.5823
Polyacrylic Acid	23.77108	1.3172	3.7303	84.5252
PVA 14,000 MW	63.22652	2.4985	64.4539	106.9646
Triton X-100	0.26456	0.1717	0.2460	0.3722

In the first dispersant evaluation, the dispersants were added post-synthesis, that is they were added after the nanofermentation process was completed and the particles were harvested. The dispersants were effective, but the goal was to further reduce the agglomerate/particle size of the NF ZnS powder. One hypothesis was that the NF ZnS particles may be agglomerating while they growing in solution. If a dispersant can be utilized during synthesis, agglomeration may be able to be further controlled and minimized. Therefore, a second set of particle size measurements were run on the seven dispersants selected post-synthesis for evaluation as in-situ dispersants, and the results are given in Table 1.6.

Table 1.6 Particle Size Results for NF ZnS In-Situ Dispersant Study

Dispersant	Sonicated	Sizes (μm)			
		Mean	Diameter on Cumulative %		
			10%	50%	90%
NTA		27.51362	1.4292	4.1024	91.6895
NTA	Yes	42.33607	0.8939	9.0422	106.9210
PEG		3.67071	0.9054	1.7291	3.8481
PEG	Yes	0.78509	0.2427	0.6549	1.4812
GLY		3.46347	0.8943	1.6846	3.7526
GLY	Yes	43.22005	0.4518	44.5329	90.1340
Oleic Acid		1.89081	0.8453	1.6176	3.2741
Oleic Acid	Yes	31.72499	0.3629	2.2040	90.8515
EDTA		3.12265	1.3719	2.7984	5.3282
EDTA	Yes	2.51732	0.7856	2.0624	4.8778
Triton X-100		33.08715	1.3137	3.7612	112.8235
Triton X-100	Yes	1.13278	0.3448	0.9436	2.1266
Lignosulfonate		72.68216	0.2780	59.7383	168.7897
Lignosulfonate	Yes	90.53172	0.2356	67.7824	209.2655

The results shown in Table 1.6 were encouraging. Similar results were seen for the Triton X-100, and an even smaller size and distribution were seen for PEG. Again, as this was a screening tool to assist in down selecting an effective dispersant, no optimization of the dispersant in terms of concentration of dispersant to surface area of the NF ZnS or the molecular weight of the PEG to the size of the particle had been completed yet. Thus, a third study was run where the concentration of the PEG was varied during synthesis from 0.05 to 5.0 weight%, a normal dispersant concentration range for colloidal to submicron particles in suspension. Again, particle size was measured on the resulting solutions, and the results are given in Table 1.7. The most reduction in particle size is seen between 0.1 and 0.5 weight% PEG. Larger concentrations show larger agglomeration indicating entangling of the PEG strands causing larger agglomerates.

Table 1.7 Particle Size Results for NF ZnS- PEG Concentration Study

Dispersant	Sonicated	Sizes (μm)			
			Diameter on Cumulative %		
PEG		Mean	10%	50%	90%
0.05% PEG		2.77971	1.2154	2.4258	4.8458
0.05% PEG	Yes	1.94941	0.4993	1.5940	3.8435
0.1% PEG		2.05337	0.9134	1.7585	3.5674

0.1% PEG	Yes	1.20252	0.3969	1.0074	2.2012
0.5% PEG		2.54345	1.0496	2.1122	4.5935
0.5% PEG	Yes	1.44521	0.4639	1.1374	2.6727
1.0% PEG		2.24235	0.9809	1.8865	3.9429
1.0% PEG	Yes	782.19592	442.1594	843.0077	969.5259
5.0% PEG		1.94428	0.8283	1.6328	3.4144
5.0% PEG	Yes	805.37909	628.0833	814.9722	964.2176

2.2.3 Zn Gallate Nanoparticle Synthesis

The Zn Gallate nanoparticle synthesis process was developed for low-cost, high performance phosphor applications. The ink development process was optimized for particle size control in the sub-micron range while larger particles were used for passive device development. The Zn Gallate material performance was evaluated in terms of the ink stability, coating quality control, particle crystallinity, PL response of intrinsic/doped coatings, and electrical conductivity. The sample splits for the investigation are listed in Table 1.8. The initial sample set included various dopants to analyze their impact on the PL emission characteristics.

Table 1.8 Zinc Gallate sample splits

Particle Type	Sample ID	Sample Description
Zn Gallate	120529_A01	FeS medium, precursor with Co 1% replacing Zn-1wk incubation Freeze dried (1.686g/3L) With sintering (30 min in air + 30 min in nitrogen gas) should show strengthened BLUE
Zn Gallate	120529_B01	FeS medium, precursor with Mn 4% replacing Ga-1wk incubation Freeze dried (2.015g/3L) With sintering (30 min in air) should show GREEN
Zn Gallate	120529_C01	FeS medium, precursor with Cr 1% replacing Ga-1wk incubation Freeze dried (1.875g/3L) With sintering (30 min in air) should show RED
Zn Gallate	120711_A01	FeS medium, precursor with Mn 4% replacing Zn-1wk incubation Freeze dried (1.574g/2L) with Gallium chloride With sintering (30 min in air) should show GREEN
Zn Gallate	120711_B01	FeS medium, precursor with Mn 4% replacing Zn-1wk incubation Freeze dried (0.897g/L) with Gallium Nitrate Hydrate With sintering (30 min in air) should show GREEN

2.2.4 Ultrasonic Excitation

The next task was to disperse nanoparticle agglomerates and increase the shelf life of inks and pastes through ultrasonic excitation. The primary surfactant used for paste development was nitrilotriacetic acid (NTA) at concentrations between 0.05 and 1.0%. Ultrasonic excitation was considered as a post-synthesis approach to physically break up agglomerate structures, both immediately following

synthesis as well as following storage. Bottled samples were placed in an ultrasonic bath and exposed to frequencies of 40, 170, and 270 kHz. The frequency 40 kHz worked the best because it reduced the particle size from 378.6 nm to 177.3 nm in one hour (Figure 1.32). Further testing of the 40 Hz frequency revealed that increasing the time to two hours yielded a small decrease in particle size. The same test run at 40 Hz for one hour in an ice bath yielded a particle size of 192.5 nm, which was larger than that generated for one hour in water of unregulated temperature.

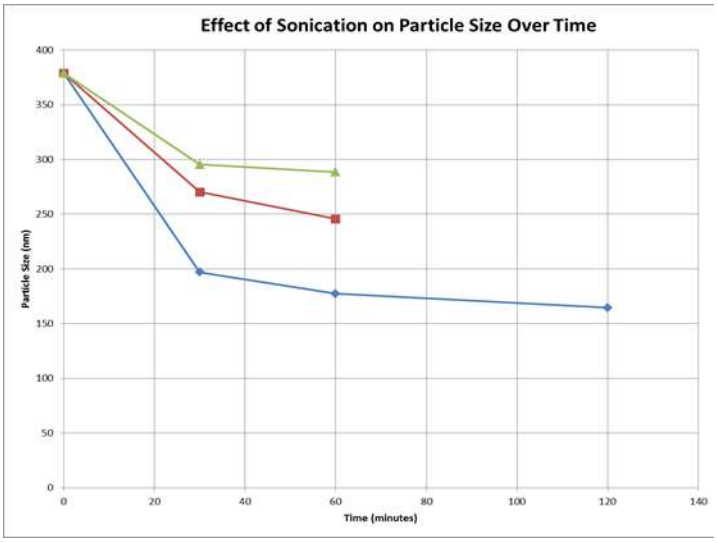

Figure 1.32. Particle size as a function of ultrasonic excitation exposure.

2.2.5 Oxidation of NF metal sulfide (ZnS, NiS, SnS, CoS, and Cu) particles

In the next phase of the study, metal sulfide samples were produced (ZnS, NiS, SnS, CoS, and Cu) and were oxidized in either air or oxygen environments over a range of temperatures to determine the optimum heat treatment conditions to convert the sulfide materials to their oxide forms. The resulting powders were analyzed using x-ray diffraction to determine the phases formed during the heat treatment (see Figure 1.33).

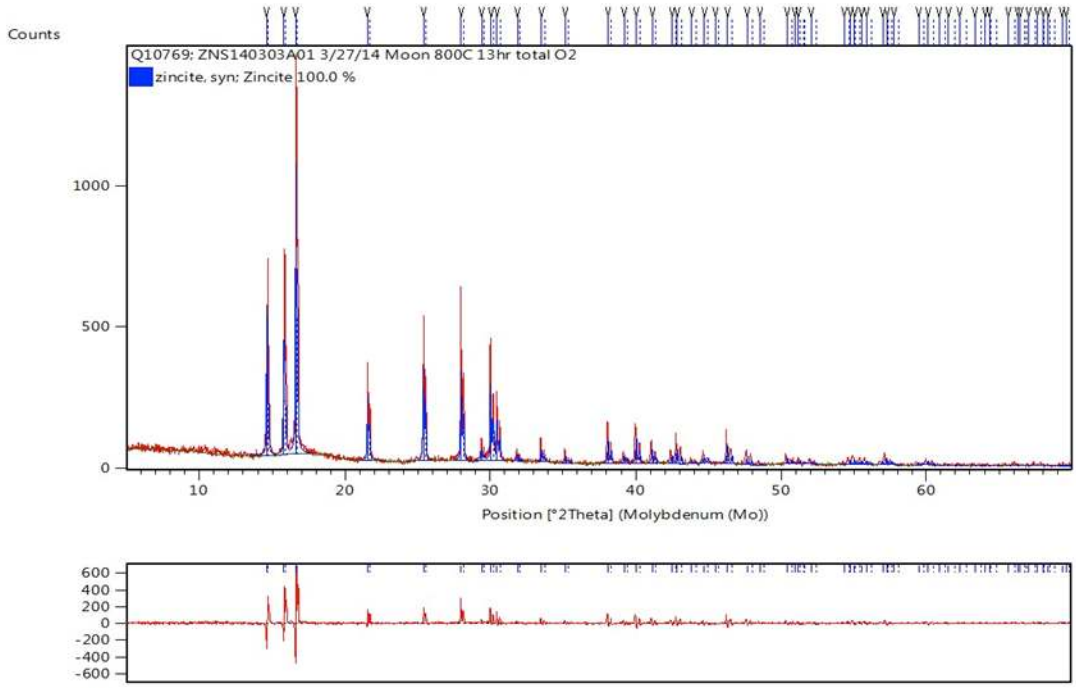

Figure 1.33. The ZnS was converted to ZnO with oxidation in O_2 atmosphere at 800°C for 1 hour.

Subsequently, a set of ZnO coatings was prepared for conductivity measurements. Two types of ZnO powder were used, one exposed to laboratory air or one exposed to pure oxygen. Both witnessed heat treatment conditions of 600°C for 1 hour. The coatings were fabricated by pressing the powder onto an adhesive Cu substrate. The Cu substrate will be used as an electrode for the conductivity measurements. A stencil (5 mm x 5 mm x 12 μm) was placed on top of the Cu to create a coated area with specific dimensions.

Fabrication of another set of ZnO and SnO coatings for conductivity measurements was initiated. This approach used screen-printing as the coating technique, and the screens were selected with the appropriate design. These included platinum screening printing paste for the electrode coating and a low temperature curing screen-printing paste vehicle from DuPont. The goal was to find either a conductive or a non-insulating coating material that will enable either no or low temperature heat treatment of the sensor materials such that flexible, polymer substrates could be utilized.

2.2.6 Oxidation of NF metal sulfide (SnS, CoS_2, Ni_3S_4, and CuS) particles

The nanofermentation process was used for binary metal oxide particle synthesis and coating development. Nanofermentation process is efficient in the development of metal sulfide particles, which can be oxidized to form metal oxide particles for advanced sensor applications. In the present study, we have investigated the oxidation efficiency of four different NF metal sulfide particles: SnS, CoS_2, Ni_3S_4, and CuS. The nanoparticles were annealed in a furnace in a flowing O_2 atmosphere at various temperatures in the range of 400-800°C. The metal-oxide structure was analyzed by x-ray diffraction technique. As shown in Figure 1.34, it was possible to obtain a well-defined oxide phase at an annealing temperature of 800°C for all the metal-sulfides except CoS_2. For CoS_2 particles, a $CoSO_4$ phase was also observed, as listed in Table 1.9, indicating incomplete removal of sulfur after 60 min of annealing at 800°C. At an annealing temperature of 600°C, only SnS was completely converted into the corresponding metal oxide. The XRD results indicated that a pure SnO_2 phase was formed even after annealing at a temperature of 400°C. The initial investigations focused on SnO_2

particles for coating development. The impact of particle size and distribution on the coating quality were evaluated, and the coatings characterized in terms of structural, optical, and electrical characteristics. The resistive sensors were developed to analyze the gas sensing characteristics of SnO_2 particles as a function of temperature.

The nanofermentation ZnS particles were oxidized to induce ZnO phase at an annealing temperature of 800°C. The oxidation efficiency was found to strongly depend on the initial ZnS amount during annealing. It was possible to induce a pure ZnO phase even at an annealing temperature of 600°C for <1g ZnS sample. However, impure ZnO phase was obtained even after annealing at 800°C when using >5g ZnS sample as shown in Fig. 1.35. The phase purity did not improve even after second annealing at 800°C for 60 min. On inspection, the furnace tube was found to be heavily coated by sulfur when using larger amounts of sulfur and the sulfur partial pressure was responsible for inefficient conversion of ZnS phase into ZnO phase. The tube was thoroughly cleaned prior to third anneal. As shown in Figure 1.35, a well-defined zincite phase was obtained after furnace tube cleaning, indicating that the oxidation efficiency was limited by sulfur partial pressure in the furnace rather than the annealing temperature. As a result of these observations, x-ray diffraction measurements were regularly conducted to maintain batch-to-batch control.

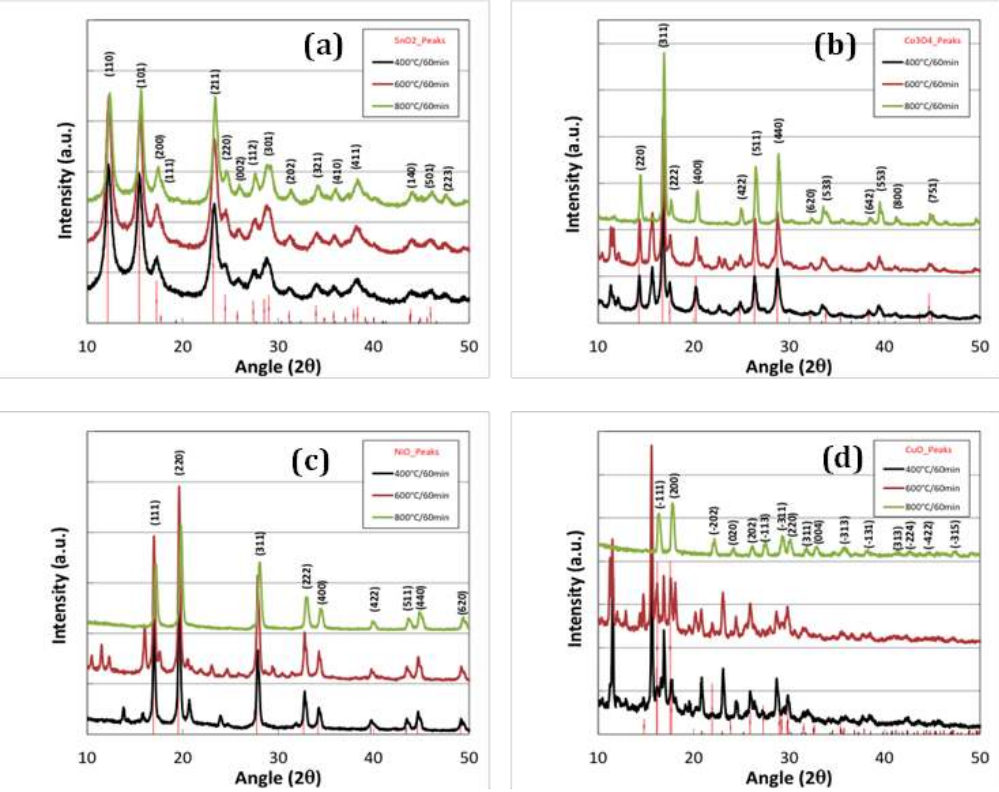

Figure 1.34. The x-ray diffraction patterns showing the impact of O_2 annealing on the metal oxide phase formation for (a) SnS, (b) CoS_2, (c) Ni_3S_4, and (d) CuS particles.

Table 1.9 The impact of O_2 annealing on the metal oxide phase formation for (a) SnS, (b) CoS_2, (c) Ni_3S_4, and (d) CuS particles.

		Annealing Temperature		
Initial Material	Target Composition	400°C	600°C	800°C
SnS	SnO_2	100%	100%	100%
Ni_3S_4	NiO	80% Ni3S2: 5% NiS: 15%	63% Ni(SO4): 37%	100%
CuS	CuO	8% Cu(SO4): 77% Cu2O(SO4): 15%	10% Cu(SO4): 48% Cu2O(SO4): 42%	100%
CoS_2	Co_3O_4	44% Co(SO4) [α-25%, β-32%]	41% Co(SO4) [α-36%, β-23%]	85% Co(SO4) [α-15%,]

Focus

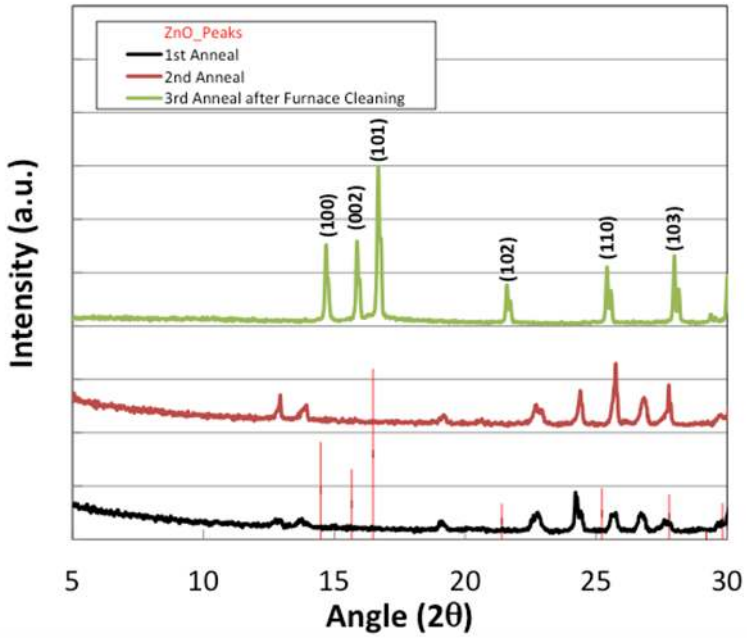

Figure 1.35. The impact of multiple anneals at 800°C on ZnO phase formation.

As a follow-on step, metal sulfide samples were produced (ZnS, Ni_3S_4, SnS, CoS_2, CdS, and CuS) and were oxidized to produce ZnO, NiO, SnO_2, Co_3O_4, and CuO. A mixed sample strategy of three runs of 24 liter dual parallel reactor was subsequently followed. In order to initiate the 24 liter reaction, 12 liter of growth medium was added to two 13.25 liter glass carboys, equipped with ventilation ports to the headspace, which were autoclaved for 2 hours. The carboys were cooled to 70

°C in the autoclave and were further cooled with continuous purging using N_2 gas through a 0.2-micron filter overnight and put into plastic containers which were connected to a 65 °C water bath. To produce SnS, the solution was enriched for 24 hours using 10 mM of glucose, 6 mM thiosulfate as a sulfur source, and 2% mid-log growth phase stock solution. SnCl was dosed after 24 hours. The three runs showed high reproducibility of average crystallite size of 3.3–3.7 nm and of the yields ranged of 15.9–17.0g / 24 liters. Figure 1.36 shows the resultant samples from the three runs, while the analysis results are summarized in Table 1.10.

Table 1.10 SnS sample preparation (24 liter) of the three batches

Run	Condition (10 mM of glucose, 6 mM thiosulfate)	Sn	Yield	Average Crystallite Size
1st, SNS140325A01	5 days in fresh medium	4mM	15.86g	3.3±0.2 nm
2nd, SNS140409A01	5 days in fresh medium	4mM	16.17g	3.5±0.4 nm
3rd, SNS140425A01	5 days in fresh medium	4mM	17.01g	3.7±0.2 nm

Figure 1.36. Samples produced from the low temperature materials synthesis project. The material was > 50g of SnS and was oxidized to n-type SnO_2 and used for gas sensing.

The consecutive batch processing resulted in ~200g of SnS, but we observed that the surface had an organic coating. We investigated the water quality, medium buffer, purging period, aging, and exposure to the air, and identified the main problem being the accumulation of carbon sources in the water. Using purified water solved this problem.

The nanofermented SnS nanoparticles were oxidized to produce SnO_2 phase at an annealing temperature of 800°C. The oxidation efficiency was found to strongly depend on the initial SnS amount during annealing. As was mentioned above for the case of ZnO, it was possible to induce pure ZnO phase even at an annealing temperature of 600°C for <1g ZnS. In Table 1.11 we show the information for the SnO_2 phases and the size of the nanocrystals. The resulting powders were analyzed using x-ray diffraction to determine the phases formed during the heat treatment (see Figure 1.37).

Table 1.11 Conversion of SnS nanoparticles to SnO_2

Sample	Phase	Wt %	Space Group	a (Å) α	b (Å) β	c (Å) γ	Size (Å)
SnS 130711 A01 800 C, 5 hours, 500 ccm O_2 P10997	SnO_2	100	Tetragonal	4.744	4.744	3.189	120
			P 42/m n m (136)	90	90	90	
SnS 140409 A01 800 C, 5 hours, 500 ccm O_2 P10999	SnO_2	100	Tetragonal	4.742	4.742	3.188	300
			P 42/m n m (136)	90	90	90	
SnS 140325 A01 800 C for 5 hours, 500 ccm O_2 P10998	SnO_2	100	Tetragonal	4.737	4.737	3.185	460
			P 42/m n m (136)	90	90	90	

The nanofermentation Ni_3S_4 nanoparticles were oxidized to produce the NiO phase at an annealing temperature of 800°C. The resulting powders were analyzed using x-ray diffraction to determine the phases formed during the heat treatment (see Figure 1.38). The NiO nanoparticles were further processed to produce printable ink that was used to characterize electrical conductivity of NiO/Pt resistors. The as-processed nanoparticles were found to be quite large, as shown in Figure 1.39, with average size exceeding 10µm. The large size is possibly due to particle agglomeration, which calls for improved chemical processes for effective passivation of particle surface bonds.

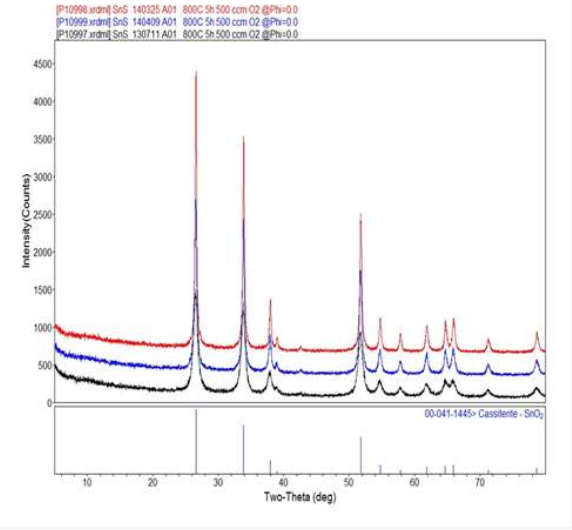

Figure 1.37. The SnS was converted to SnO_2 with oxidation in O_2 atmosphere at 800°C for 1 hour.

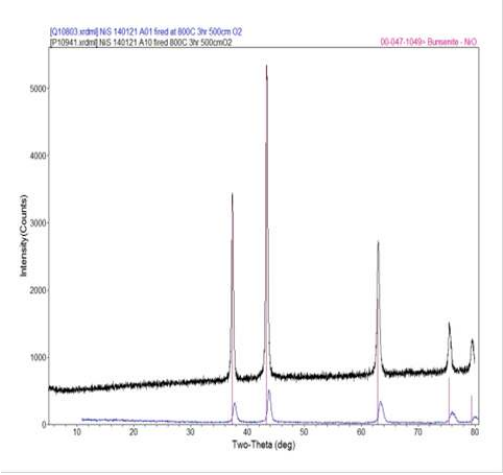

Figure 1.38. The Ni3S4 was converted to NiO with oxidation in O2 atmosphere at 800°C for 1 hour. A pure NiO phase was produced after annealing at 800°C.

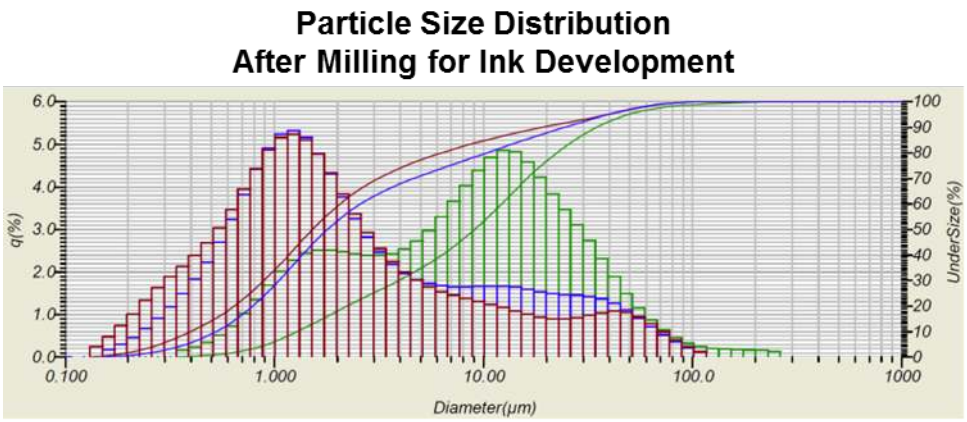

Figure 1.39. Particle size distribution of NiO nanoparticles that were processed to produce a printable ink.

2.2.7 Sensor Test Apparatus

An essential part of the sensor development was the design of the experimental environment where sensors can be tested. We teamed with the Center for Nanophase Materials Sciences and developed Environmental Chamber Vacuum- Referenced, Multimode Sensing system which allowed for cross referenced testing of thin film sensors in a controlled environment (see Figure 1.40). The pressure in the vacuum chamber was 10^{-6} Torr, the humidity 0-90%, the oxygen concentration 0.01 - 20%, the temperature RT<T <85 C. The programmable multimode testing was with a Keithley 4200SC (PV, diode, transistor.), along with broad frequency impedance spectroscopy, transmittance, reflectance, photoluminescence, Raman (1064 nm) measurements. The system was also implemented for in situ measurements of changes in the thin film weight using a 5 MHz Quartz crystal microbalance. Multimodality of sensors was also advanced with in situ statistical analysis (PCA, MCR).

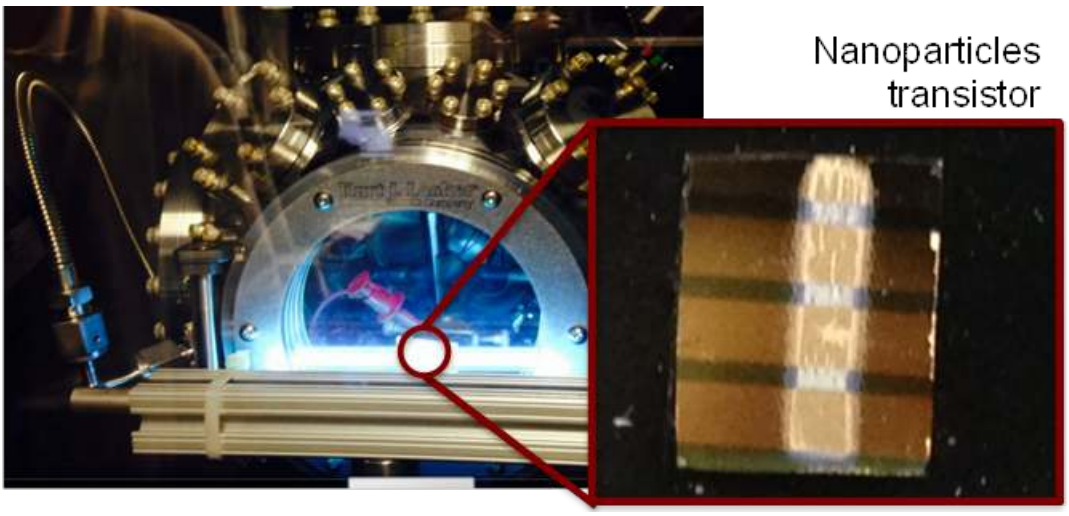

Figure 1.40. Background image of the Environmental Chamber. The inset shows the screen printed ZnO transistor on the surface of Si/SiO2 wafer tested in the chamber.

2.2.8 Low Temperature Nickel Oxide Thin Films

Metal oxide thin films offer a unique combination of structural, electrical, optical, magnetic, and chemical properties for advanced sensor applications. Low temperature processing of high quality metal oxide thin films was critical for integration into a flexible sensor platform. The investigation focused on the development of low temperature nickel oxide (NiO) thin films exploiting RF sputtering and pulse thermal processing techniques. NiO is a wide bandgap *p*-type semiconducting material with suitable properties for gas sensor, battery, supercapacitor, organic light emitting diode (OLED), and solar cell applications. The electrochromic properties of NiO are being exploited for a wide range of applications, such as energy efficient windows and multi-color displays. The details of the NiO thin film deposition process and the impact of process temperature on the microstructural, optical, and electrical characteristics are highlighted in the following sections.

2.2.8.1 Nickel Oxide Thin Film Deposition

NiO thin films were deposited by a RF sputtering technique from a stoichiometric NiO target in an $Ar+O_2$ atmosphere. As shown in Figure 1.41(a), the Ar/O_2 ratio, chamber pressure, and RF sputtering power were kept constant at 80%, 9 mTorr, and 350W, respectively, while the effects of process temperature on the thin film growth and properties were analyzed in the range of 25-400°C. The NiO thin films were deposited on bare Si and fused quartz substrates. The deposition rate of NiO thin films, as shown in Figure 1.41(b), was found to decrease from 12.7 Å/min to 10.3 Å/min with an increase in process temperature from 25 to 400 °C. The observed temperature dependence of the thin film deposition rate indicated that the grain growth was influenced by the process temperature.

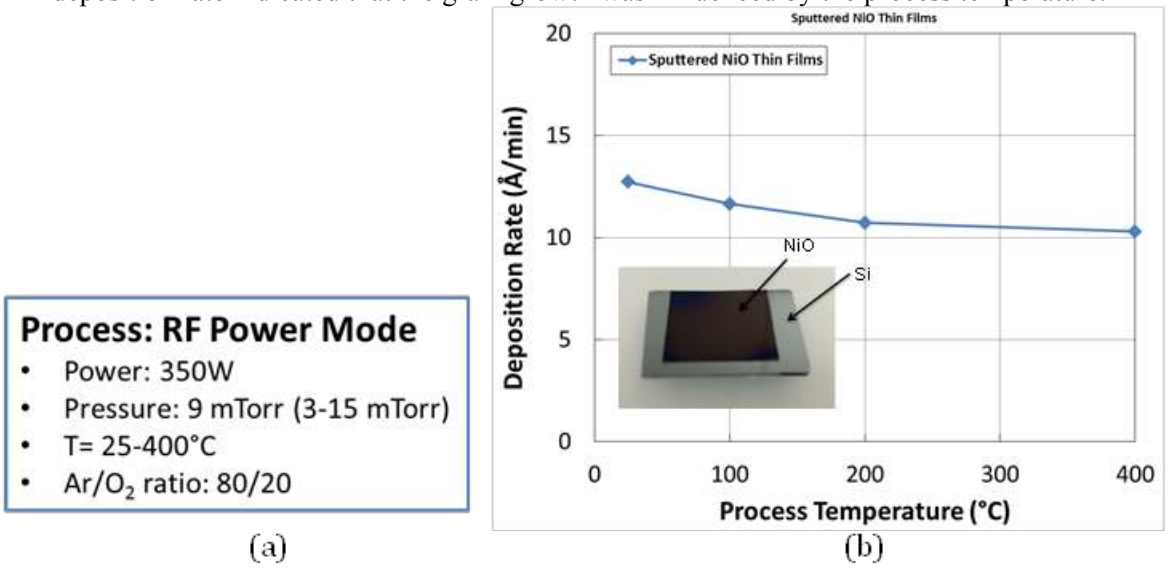

Figure 1.41. (a) Process conditions and (b) deposition rate of rf sputtered NiO thin films as a function of substrate temperature.

2.2.8.2 Nickel Oxide Microstructure

The crystallinity of NiO thin films was analyzed by x-ray diffraction (XRD) technique. Figure 1.42 shows the XRD patterns of the films deposited on bare Si and fused quartz substrates. All the films deposited in the temperature range of 25-400°C exhibited a polycrystalline cubic phase. The XRD peak intensity was found to increase with an increase in deposition temperature indicating an improvement in film crystallinity. The XRD patterns did not show any appreciable change in the FCC phase with process temperature indicating the formation of a stable phase. The NiO thin films

showed a preferential growth along the [111] direction. A similar XRD pattern was obtained on films deposited on amorphous quartz substrates indicating that the film growth was not influenced by substrate microstructure. The morphology of the films was analyzed by scanning electron microcopy as shown in Figure 1.43.

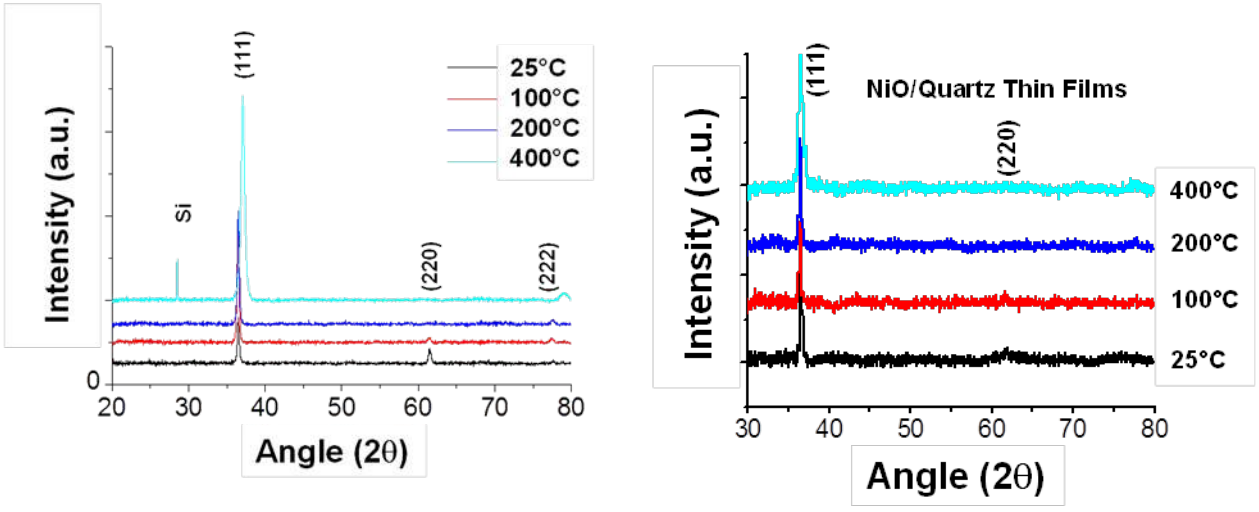

Figure 1.42. The x-ray diffraction patterns of NiO thin films deposited on (a) Si and (b) quartz substrates.

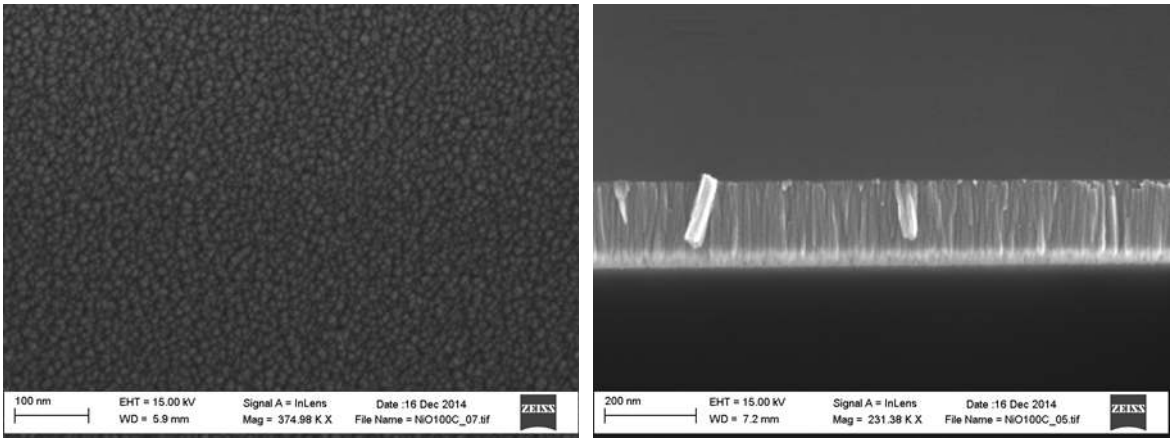

Figure 1.43. (a) Surface morphology and (b) SEM cross section of NiO thin films deposited on Si substrates at a temperature of 100°C.

The surface and cross-sectional morphology of NiO films deposited at 100°C showed a dense microstructure with fine grains. The SEM cross section showed closely packed columnar grains which grew perpendicular to the film surface. The high crystallinity and dense microstructure of NiO thin films deposited at low process temperatures show promise for integration on flexible paper and plastic substrates.

2.2.8.3 Nickel Oxide Optical Properties

The optical properties of NiO thin films were established from the transmittance and reflectance measurements (Figure 1.44) conducted at room temperature using a UV-VIS-NIR spectrophotometer. The optical transmittance of the NiO thin films, as shown in Figure 1.44(a), indicated a wide bandgap in the process temperature range of 25-400 °C with absorption edge in the UV part of the spectrum.

The optical transmittance of NiO thin films did not show any appreciable temperature dependence down to a process temperature of 100 °C while it was found to decrease appreciably at 25°C. To gain further insight into the optical response, the optical absorption coefficient, α, was calculated from the optical transmittance, *T*, and reflectance, *R*, data using the relation: $\alpha = 1/t[\ln T/(1-R^2)]$, where *t* is the film thickness.

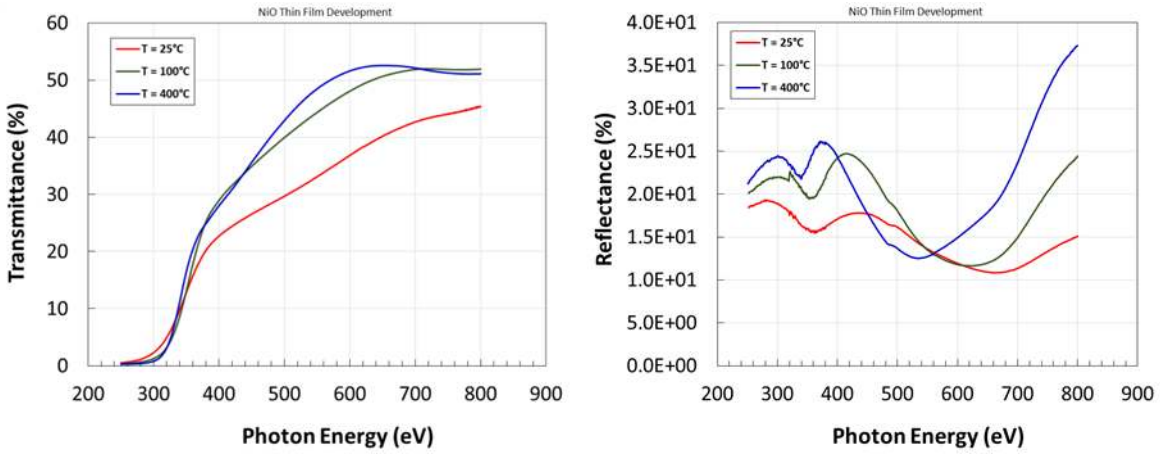

Figure 1.44. (a) Optical transmittance and (b) reflectance of NiO thin films as a function of process temperature.

For direct bandgap NiO thin films, the absorption coefficient dependence on the incident photon energy, $h\nu$, is given by the relation: $\alpha h\nu = A(h\nu - E_g)^{1/2}$, where Eg is the material bandgap. The energy of the optical bandgap of NiO thin films was established by extrapolating the linear part of the $(\alpha h\nu)^2$ *vs* $h\nu$ plot to abscissa. The optical bandgap of the NiO thin films, as depicted in Figure 1.45, did not show a strong dependence on the process temperature and the value remained higher than 3.3 eV in the process temperature range of 25-400 °C. The observed wide bandgap value even at a process temperature of 25 °C is in good agreement with the values reported for films processed at higher temperatures exceeding 200 °C, indicating high optical density of the present films. The present NiO thin films were deposited at an oxygen partial pressure of 20%. The high optical bandgap of NiO thin films deposited at 25°C indicates that the film stoichiometry and density were dictated by the oxygen partial pressure and the plasma density rather than the thermal state of the substrate. The observed optical properties of NiO thin films are consistent with the XRD and SEM analyses indicating the formation of a well-defined polycrystalline phase and a dense microstructure even at a low process temperature of 25 °C.

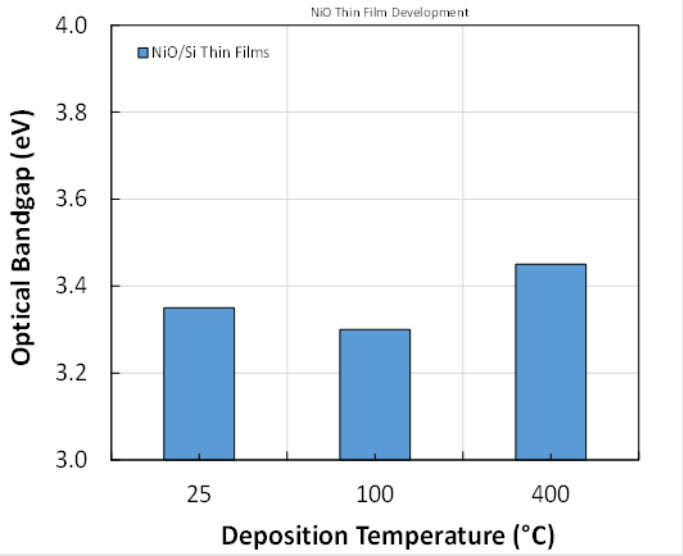

Figure 1.45. The optical bandgap of NiO thin films as a function of process temperature.

The *n-k* optical dispersion characteristics were established from the spectroscopic ellipsometry measurements as shown in Figure 1.45(a and b). Spectroscopic ellipsometry data were obtained using a two-modulator generalized ellipsometer (2-MGE) at an angle of incidence of 65.01°. NiO thin films were modeled as a simple three layer structure (interface-1/NiO/interface-2) to fit the Tauc-Lorentz dispersion function. Interface-1 was modeled through Bruggeman effective medium approximation, consisting of 50% void and 50% of the NiO medium below. Interface-2 was modeled as native oxide layer on the Si substrate. The optical constant of the NiO thin films were well-behaved, as shown in Figure 1.46, and the energy dispersion matched well with the reported data on single crystal, thin films, and nanoparticles. The observed results are consistent with the XRD findings showing a well-define crystalline FCC phase in NiO thin films even at a low processing temperature of 25 °C.

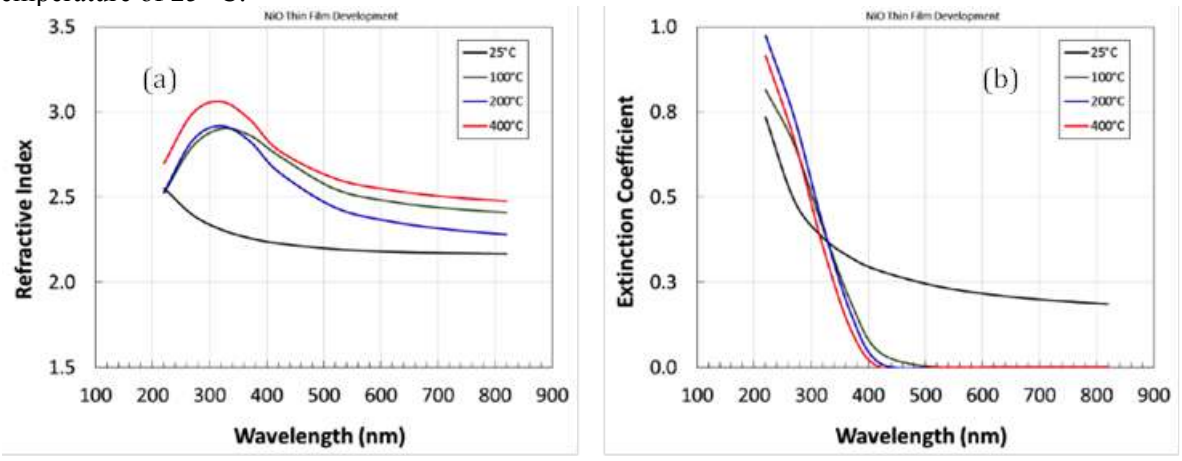

Figure 1.46. (a) Refractive index and (b) extinction coefficient of NiO thin films as a function of process temperature.

2.2.8.4 Nickel Oxide Hall Measurements

The electrical properties of the NiO thin films deposited on quartz substrates were evaluated by Hall effect measurements. As shown in Figure 1.47a, the carrier concentration values were found to be

positive in the entire processing temperature range of 25-400 °C indicating *p*-type conduction. The mobility of the NiO films was measured to be 0.40 cm^2/Vs at a process temperature of 400 °C. As shown in Figure 1.47 (b), the mobility value decreased with a decrease in process temperature down to 100 °C. However, it was found to be increase appreciably to a value of 0.86 cm^2/Vs at a process temperature of 25 °C. The observed increase clearly indicates a change in the thin film microstructure that influences carrier scattering. The XRD patterns did not indicate any significant change in the film crystallinity as a function of process temperature. Detailed electrical measurements will provide further insight into the critical process parameters dictating the thin film growth and observed high mobility at a process temperature of 25 °C. The *p*-type NiO films showed a high carrier concentration of about 4.2×10^{17} cm^{-3} at a process temperature of 25 °C. The carrier concentration remained in the range of $(4.2\text{-}22.4)\times10^{17}$ cm^{-3} for films processed in the temperature range of 25-400 °C indicating that the film density was well maintained even at low process temperatures suitable for flexible substrate integration.

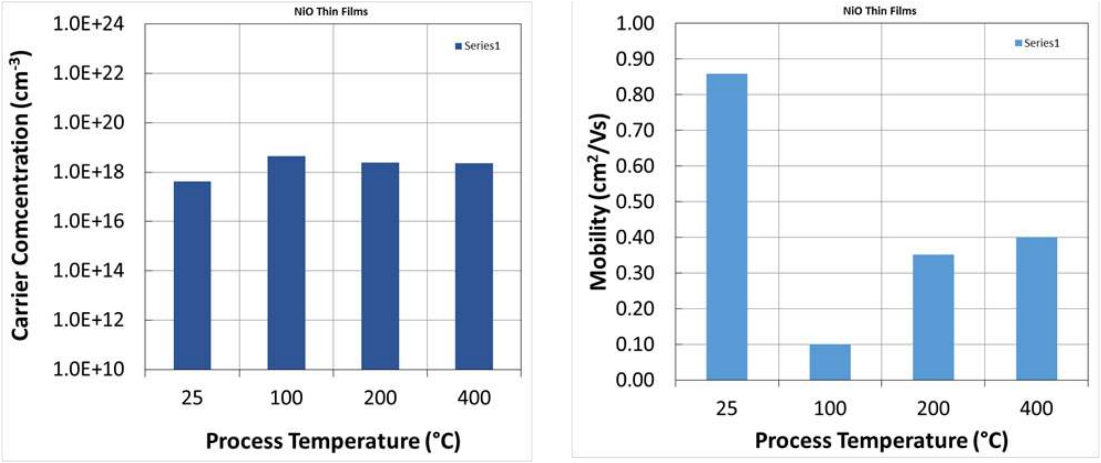

Figure 1.47. (a) Carrier concentration and (b) Hall mobility of NiO thin films as a function of process temperatures.

2.2.8.5 NiO Low Temperature Photonic Curing

The pulse thermal processing (PTP) technique was explored to influence NiO thin film properties at low thermal budgets suitable for integration on low temperature substrates such as plastic and paper. The photonic curing system is capable of delivering a high intensity, short duration (<20ms) broadband light (200-1400nm) from a directed xenon flash lamp to generate very high processing temperatures required for thin film densification, recrystallization and annealing, but without damaging the underlying temperature-sensitive substrates or co-integrated electronics. The photonic curing system is capable of delivering maximum peak power in excess of 20kW/cm^2 while the pulse width can be maintained as short as 30 microseconds. Table 1.12 lists the sample splits for the first lot of samples used in PTP investigation. The peak pulse power was varied in the range of 2.6-9.1 kW/cm^2 while keeping the pulse width and number of pulses constant at 500 µs and 25, respectively. A test sample exposed to 100 pulses of 1 ms duration was also included in the first lot to analyze the impact of thermal budget on thin film microstructure. Figure 1.48 shows the impact of PTP curing on the crystallinity of NiO thin films deposited at process temperatures of 25 and 100 °C. The crystallinity of the films deposited at 25°C did not show any significant impact of the photonic curing while the films deposited at 100 °C showed a small variation in the [220] peak intensity while the dominant [111] peak intensity did not change appreciably. The SEM, optical and electrical measurements need to be conducted in details to gain further insight into the impact of photonic

curing on film microstructure, optical absorption characteristics, and electrical conductivity. Overall, the high quality of the low temperature deposited NiO thin films in combination with the low thermal budget photonic curing show promise for the integration of NiO sensor on a flexible sensor platform.

Table 1.12 Samples splits for low thermal budget photonic curing investigation

S.No.	Sample ID	Dep. Temp. (°C)	Peak Power (kW/cm^2)	Number of Pulses
1	NiO_RT	25	2.6	25 pulses
2	NiO_100	100		
3	NiO_RT	25	4.3	25 pulses
4	NiO_100	100		
5	NiO_RT	25	6.4	25 pulses
6	NiO_100	100		
7	NiO_RT	25	9.1	25 pulses
8	NiO_100	100		
9	NiO_RT	25	2.4	100 pulses
10	NiO_100	100		
11	RT_Ref	25	No PTP	Reference sample
12	100_Ref	100	No PTP	Reference sample

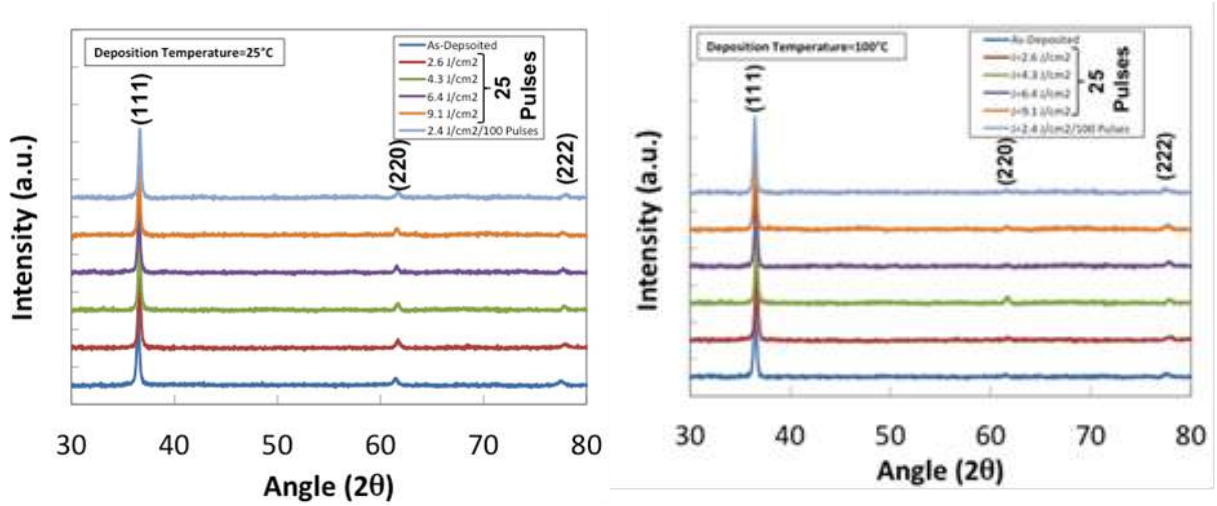

Figure 1.48. The impact of photonic curing on the structural characteristics of NiO thin films deposited at 25 °C and 100 °C.

2.3 THIN FILM DEPOSITION

Thin films were deposited by ultrasonic spray deposition technique (see later in section below). Pulse thermal processing (PTP) techniques were used for low thermal budget annealing of thin films and the impact of PTP treatment was evaluated by performing thin film characterization in terms of the structural, optical, and electrical properties.

2.3.1 Ultrasonic Spray Coating Technique

The nanoparticle thin films were deposited by ultrasonic spray deposition technique using sono-spray system as shown in Figure 1.49. The robotic sono-spray system offers partial atmosphere and process temperature controls (25-180°C) for high quality thin films development. The key features of the sono-spray systems are highlighted below:

- Processing nanoparticle dispersions into thin film
- Optimization of single/multi-layer coatings on quartz and glass slides
- Characterization of optical properties of thin film assemblies
- Optimization of temperature, dispersant, particle size, surface treatment conditions

2.3.2 Optical Characterization

Two different optical techniques were used to characterize ZnS and CdS nanoparticles fabricated using nanofermentation: 1) diffuse reflectance and 2) photoluminescence.

2.3.2.1 Diffuse Reflectance

Diffuse reflectance measurements were taken on samples of nanoparticles enclosed in a mini-cuvette ~ 200 microns thick. The measurement apparatus consisted of a Perkin-Elmer Lambda 900 spectrophotometer equipped with an integrating sphere, pictured in Figure 1.49. The resulting diffuse reflectance data, shown in Figure 1.50(a) can be interpreted using the Kubelka-Munk theory[1], originally developed for the characterization of paper. This theory works best for optically thick materials, where very little of the light is transmitted through the sample and when the amount of reflected light is >~20%. Using this theory, the ratio of the absorption coefficient S and the scattering coefficient S can be expressed in terms of the reflectance R as:

$$\frac{\alpha}{S}=\frac{(1-R)^2}{2R}$$

The resulting values of the ratio α/S are shown in Figure 1.50(b).

1 Kubelka and Munk, Zeit. Fuer Tekn. Physik, **12**, 593 (1931)

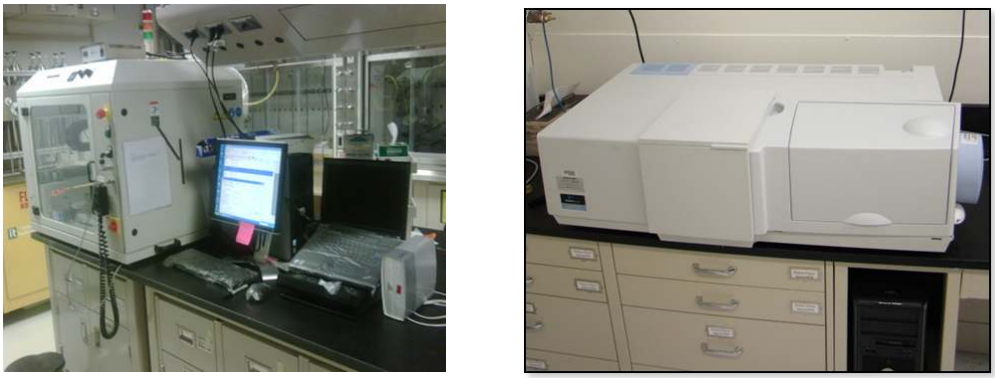

Figure 1.49. Sono-spray deposition system for nanoparticle thin film processing (L) and Perkin-Elmer Lambda 900 spectrophotometer with integrating sphere attachment (R)

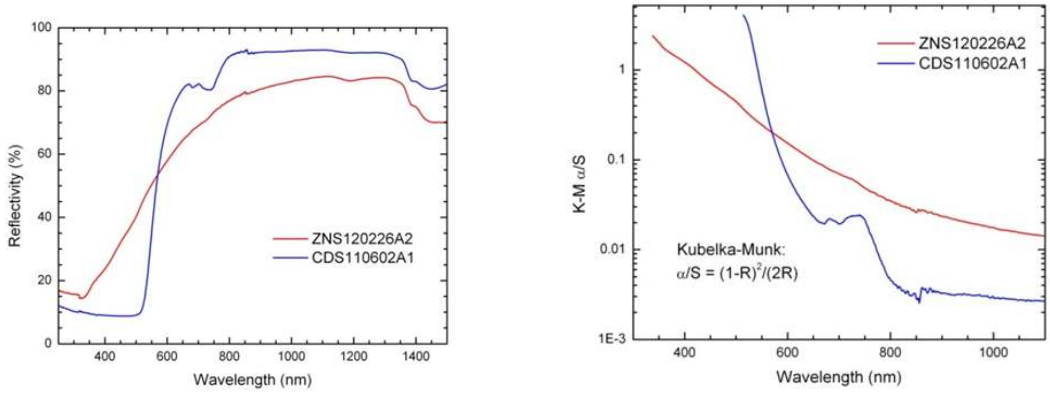

Figure 1.50. a) The measured diffuse reflectivity from samples of nanocrystalline ZnS and CdS. b) the values of the Kubelka-Munk α/S coefficient, determined from the reflectivity measurements.

From the data shown in Figure 1.50(b), we can conclude that the onset of optical absorption in the CdS nanoparticles is quite sharp, and the band edge is ~500 nm. This is consistent with the observed band edge of thin-film CdS (~2.5 eV ~ 500 nm)[2], commonly used as emitters for CdTe and CIGS solar cells. Moreover, the CdS spectrum in Figure 1.50(b) shows two absorption features near 670 and 720 nm. The identity of these features is not known at this time.

While the onset of optical absorption for CdS is quite abrupt, the onset of optical absorption for ZnS is quite gradual. It is not known why this is the case, but may relate to the size distribution of the ZnS nanoparticles in the sample.

2.3.2.2 Photoluminescence

The photoluminescence system consists of several light sources and two detectors. The sample can

2 J. Li, J. Chen, and R. W. Collins, Appl. Phys. Lett. **97**, 181909 (2010).

be illuminated using 1) a pulsed nitrogen laser (337 nm), 2) a multi-line argon-ion laser with 6 lines between 457 and 514 nm, and a HeNe laser at 633 nm. The light can be detected using a photomultiplier tube (200-850 nm) or a cooled Ge detector (600-1700 nm). The monochromator is an Oriel/Newport Cornerstone 260 with 3 gratings and a filter wheel. The sample can be placed in a closed cycle cryostat to obtain temperatures from 10K to 400 K. The detected light can be continuous wave (CW) or chopped, where the chopped system incorporates a Stanford Research 830 lock-in amplifier.

Figure 1.51 shows photoluminescence spectra from the CdS and ZnS samples, also discussed above. The ZnS sample shows a large, broad PL peak near 520 nm, which is not duplicated with the CdS sample. This broad PL peak in ZnS is similar to that observed in other nanocrystalline samples of ZnS[3], where the peak and breadth of the observed PL is a function of the distribution of particle size in the sample. The spectra from both samples show several distinct lines, where the line width is determined by the instrumental line width (1.5 nm for the present configuration). The origin of these distinct lines is unknown at present.

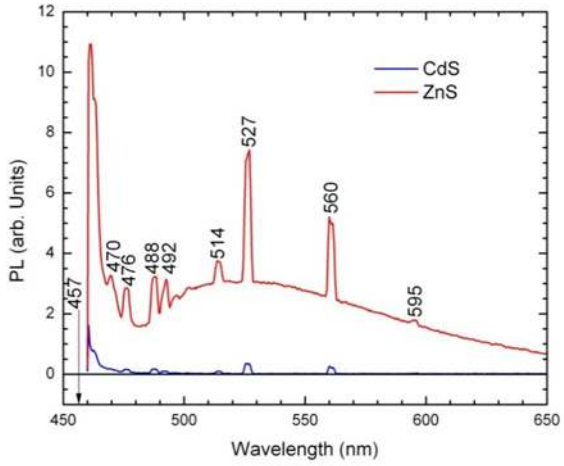

Figure 1.51. The photoluminescence spectra from the CdS and ZnS nanocrystalline samples.

2.3.3 Sonospray Coatings

The sonospray deposition system was shown to be advantageous over other deposition approaches, including jet printing, to generate high quality nanoparticle coatings. The Exactacoat setup was used for thin deposition on the surface of 2×3 inches glass slides. Prior to depositions, glass slides were cleaned in isopropanol and acetone for 15 min under mild sonication. The thermodynamics of ZnS PEI solution on PE and glass substrates was tested using dynamic sessile drop method for a series of solutions of water, PEI and ZnS in PEI. The results are summarized in Figure 1.52.

As shown in Figure 1.52(a), the introduction of PEI increases contact angle from 13 to 33 degrees for glass. Nanoparticles further increase the value of contact angle solution to 34 degrees. While further increase in ZnS nanoparticles concentration may further increase the contact angle, it is still smaller that contact angle of water-PEI-ZnS solutions on plastic. This suggests that the glass substrate is better for sonospray deposition of ZnS-PEI solution.

3 C. Unni, D. Philip, and K. G. Gopchandran, Opt. Mat. **32**, 169 (2009).

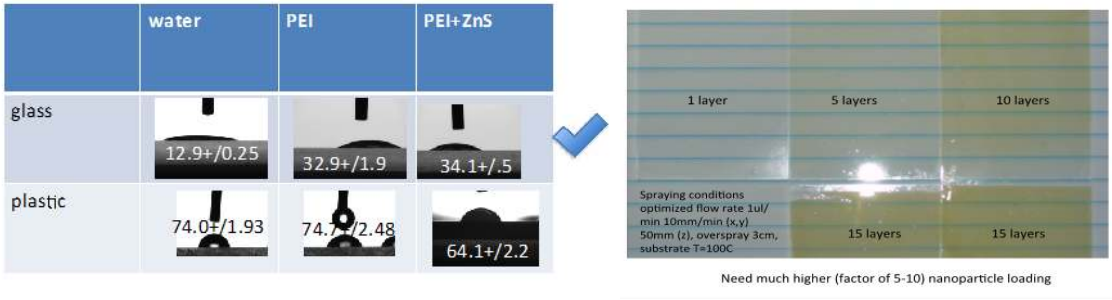

Figure 1.52. The ZnS thin film coating development in terms of (a) solvent/substrate interaction and (b) nanoparticle loading effect analysis.

2.3.3.1 Thin Film Characterization

We tested nanoparticle deposition in various regimes of the flow rate, X-Y raster speed and Z- high. The substrate temperature was varied from room temperature to 100oC. The optimal deposition was obtained for substrates heated to 100oC. It allowed complete removal of water after each pass. Multilayer depositions were tested as well. Figure 1.52(b) shows a series of depositions of 1, 5, 10 and 15 layers of PEI-ZnS solution using optimized deposition conditions: flow rate 1µl/min 10mm/min (x,y) 50mm (z), overspray 3cm, substrate T=100^{o}C. All films demonstrate good coating uniformity, which was tested using optical transmittance measurements in different areas of the film (Figure 1.52(b)).

After deposition the coatings were further dried in the air and tested using LED 450 nm transmittance/photoluminescence. The results and photograph of transmittance through 15 layers system are shown in Figure 1.53. The nanoparticle film uniformity was found to be independent of the number of coatings.

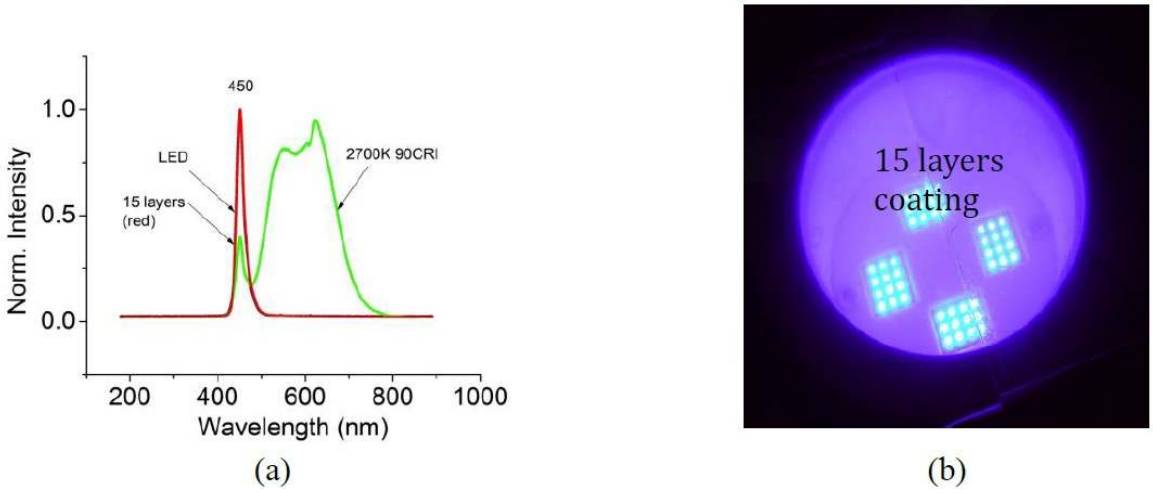

Figure 1.53. (a) Optical transmittance and (b) thin film uniformity as analyzed using 450nm LED.

Preliminary experiments on PEI removal indicated that 200°C annealing was not sufficient for complete removal of organic binder. After 40 min annealing, the color of PEI-ZnS film turned brown and did not change after further annealing at the same temperature for 3 hours. Thermal gravimetric analysis of 600, 1200 and 1800 MW PEI; as shown in Figure 1.54, suggests that a high temperature is required to remove PEI from the coating. The requirement to anneal nanoparticle coatings is temperatures > 600°C for complete PEI removal. Low temperature annealing (200°C) is expected to leave as much as 98% and as low as 92% PEI on the surface. One has to consider the consequence of using high temperature annealing for binder removal as it may alter chemical composition of the nanoparticles.

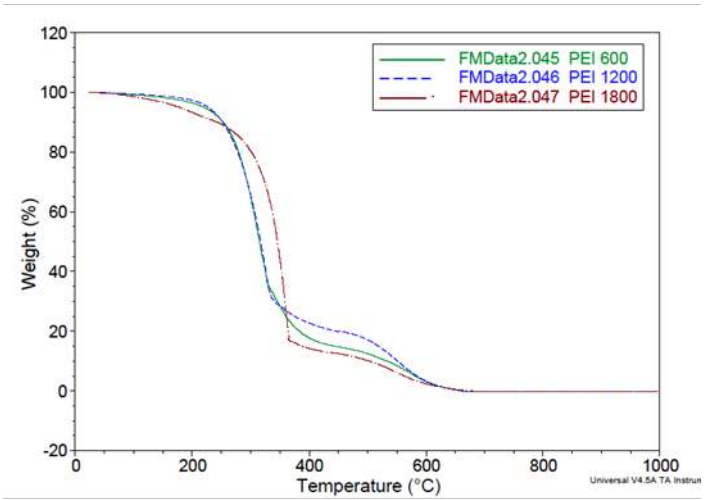

Figure 1.54. Thermal gravimetric analysis of PEI based ZnS nanoparticle inks.

The main conclusions are as follows:

- Small contact angles for (ZnS-PEI 600) glass surface were measured
- Good quality coatings (up to 15 layer coating was sono-sprayed) on glass were made
- Viscosity of water- PEI solutions is adequate for sonospray deposition of nanoparticles
- Annealing at 200°C in air does not remove PEI completely
- Temperatures higher than 600C in air are needed to remove PEI coating.
- Higher (5x) ZnS loadings are needed to create high optical density of phosphor.

In the next phase of the study, the films were annealed at various temperatures to remove organic components, density microstructure, and improve crystallinity. Figure 1.55 shows the optical images of the ZnS nanoparticle (~3.8nm) films before and after annealing at 800°C. There was no visible difference in the surface microstructure. The film adhesion was a major challenge at this stage in the thin film development. The films were found to peel-off near the edges after annealing. The ink chemistry was being modified in close correlation with the film adhesion characteristics to address the issue.

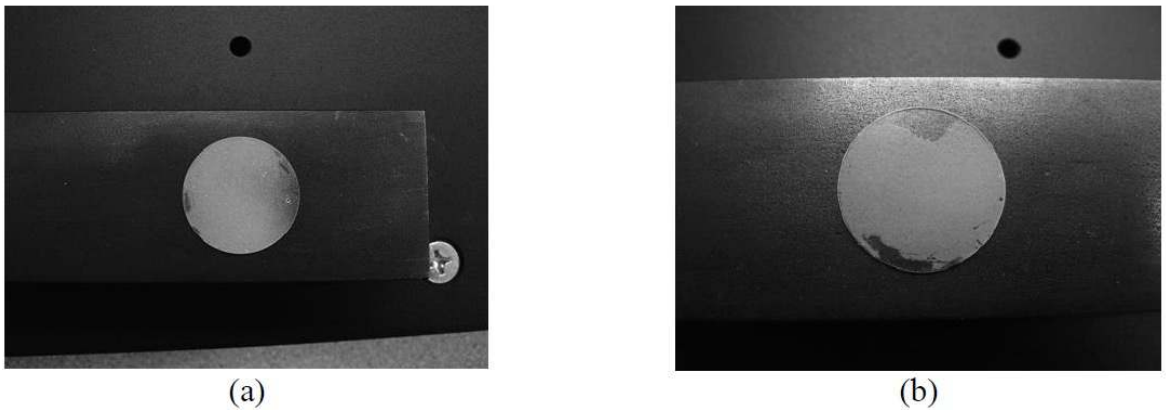

(a) (b)

Figure 1.55. Optical images of the ZnS thin films deposited quartz substrates: (a) as-deposited, (b) annealed at 800°C/30minutes.

A high resolution optical microscope was used to further analyze the surface morphology of the ZnS nanoparticle thin films. As shown in Figure 1.56, the films showed a significantly improved surface roughness profile and increased density after annealing. However, micro-cracks were also observed after annealing indicating a large change in film stress and density after annealing.

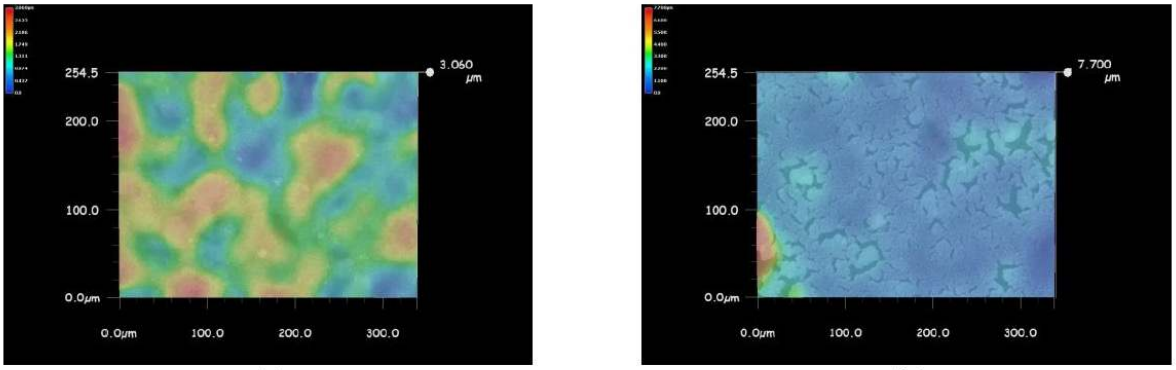

(a) (b)

Figure 1.56. Surface morphology of ZnS nanoparticle thin films: (a) as-deposited, (b) annealed at 800°C/30minutes.

Figure 1.57 shows the diffuse transmittance of the as-deposited and annealed ZnS thin films. The film transmittance was found to increase after annealing indicating an effective removal of the organic components. The optical absorption edge also shifted to higher energy levels indicating an improvement in ZnS crystallinity and microstructure.

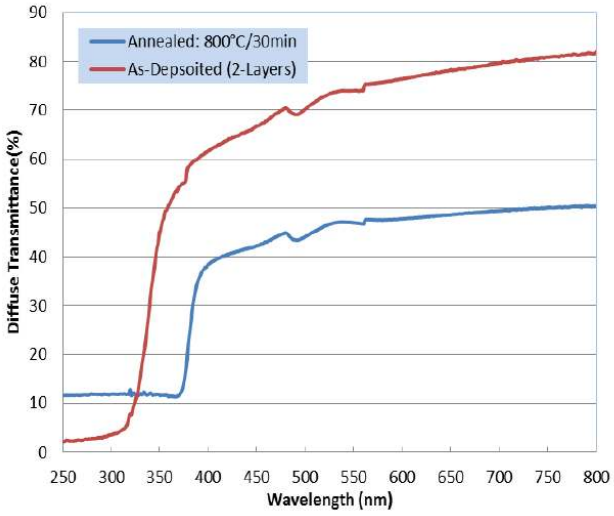

Figure 1.57. Diffused transmittance of ZnS nano-particle thin films deposited on quartz substrates.

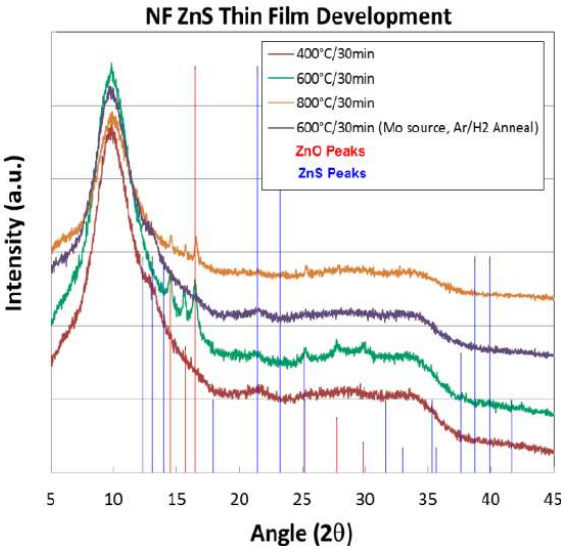

Figure 1.58. X-ray diffraction patterns of ZnS nanoparticle thin films as a function of annealing temperature

The crystalline nature of ZnS films was analyzed by x-ray diffraction (XRD) technique as shown in Figure 1.58. The XRD measurements were conducted on ZnS nanoparticle (~3.8-4.7nm) thin films deposited on quartz substrates. The films were annealed in normal air and forming gas (Ar/H_2(4%)) atmospheres. The annealing temperature had a strong influence on the ZnO phase formation. These results indicated that normal atmospheric air was enough to induce thin film oxidation even at a temperature of 400°C. It is not clear if the ambient oxygen alone was the source of oxidation.

It was possible to prevent the oxidation of ZnS nanoparticle thin films in an Ar/H_2 (4%) atmosphere as shown in Figure 1.58. However, the films turned black even at a low H_2 concentration of 4%, indicating possible reduction of ZnS thin films.

Fourier transform infrared (FTIR) measurements were conducted to analyze the impact of annealing temperature on the impurity related bonds in ZnS thin films. The FTIR spectra of ZnS nanoparticle thin films is shown in Figure 1.59(a) while the organic activity in various ZnS samples processed by NanoFermentation (NF) approach is shown in Figure 1.59(b). The ZnS thin films showed a significant reduction in -OH, CH_3, CH_2, and COO- bond concentration with increasing annealing temperature. Organic activity was very week after annealing at 800°C. Overall, it was clear that annealing temperature has a strong influence on film crystallinity, microstructure, and optical properties.

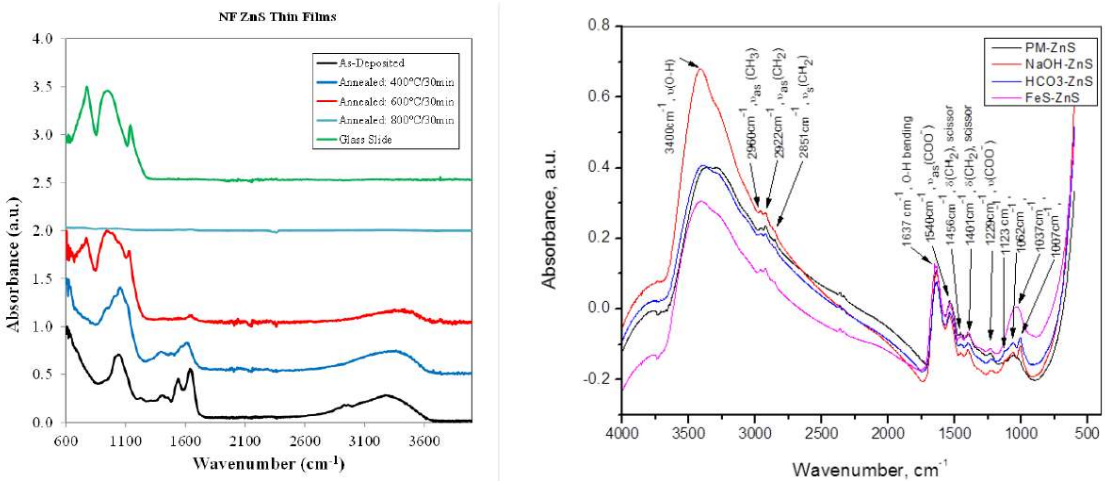

Figure 1.59. The FTIR spectra of (L) ZnS thin films and (R) various NF ZnS nanoparticle samples.

2.3.3.2 Photoluminescence

A HeCd laser, which emits 2 laser wavelengths - 325 nm and 442 nm (3.82 and 2.81 eV) was used as an excitation source for the study of ZnS and ZnO materials (with band gaps of ~3.54 and 3.44 eV, respectively), since the 325 nm line has sufficient energy to promote electrons from the valence band to the conduction band. The previous cw excitation source was an argon ion laser, which emits 6 lines between 458 and 514 nm (2.71 to 2.41 eV) all of which do not have sufficient photonic energy.

Several samples of nanoparticles of ZnS made by NanoFermentation were examined using photoluminescence, and the results are shown in Figure 1.60. The NanoFermentation process produced nanoparticles of various sizes, depending on the length of incubation in the solution with the bacteria. However, this process produced a distribution of particle sizes which was quite broad. Table 1.13 summarizes the growth conditions of the samples examined using photoluminescence, as well as identifying the plots shown in Figure 1.60. The blue data points in Figure 1.60 represent data from crystalline ZnO, used as a reference. The scale of the ZnO PL spectrum is ~50 times that of the PL from the NanoFermentation samples. (That is, the ZnO signal is ~50 times stronger).

Table 1.13 Data for photoluminescence of nanoparticles in solution for Figure 1.60

Graph color	Fabrication date	Peak Energy	Est. average particle size (nm)
Cyan	Sept 26 2012	2.89±0.02	9.5±0.2
Green	Aug. 23, 2012	2.86±0.02	7±1
Red	June 15, 2012	2.84±0.02	2-3
Magenta	June 27, 2012	2.83±0.02	2-3
Blue (c-ZnO)	---	3.28	---

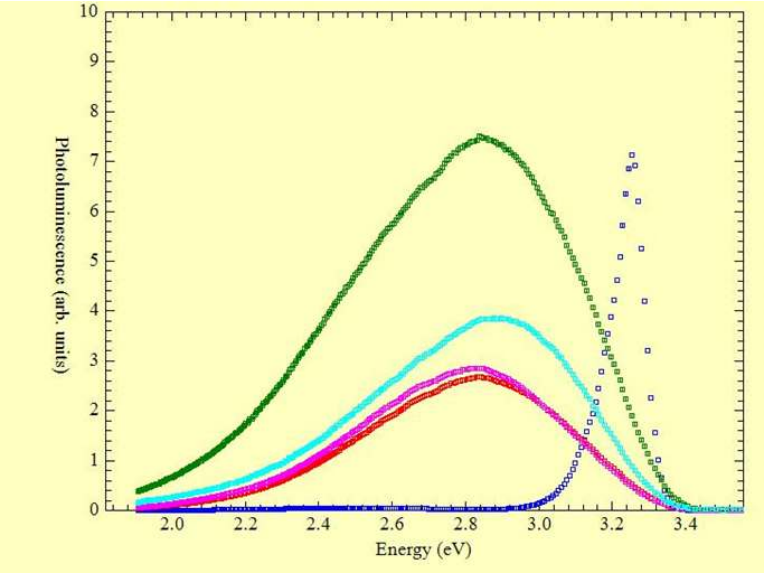

Figure 1.60. Photoluminescence of various sizes of nanoparticles in solution.

The PL from the ZnO sample showed the characteristic excitonic response just below the band edge. In addition, the ZnO PL shows a weak defect PL ~2.5 eV (See Figure 1.61), related to defects in the crystalline material. While the shape of the PL spectra from the nanoparticle solutions is representative of the samples, the magnitude of the various spectra is not significant, since the data were taken at various sensitivities on the lock-in amplifier, and some of the samples (red and magenta) were significantly diluted. However, the PL shown in Figure 1.60 and Table 1.13 do show a very broad peak that does correlate with the estimated average particle size, with the higher peak PL energies corresponding to larger estimated average particle sizes. Moreover, the observed PL response is very broad.

While there was a correlation of peak PL energy with particle size, it was small and opposite to what is often observed with PL of nanoparticles (reduced particle size often results in an increase of PL energy). This, coupled with the observation that the PL spectra were very broad indicated that the PL measurement is integration over all particle sizes in the sample, and may not correlate well with the estimated average particle size.

Figure 1.61 shows the resulting PL spectra from a variety of consolidated films of ZnS nanoparticles, as well as a reference PL from a ZnO sample. The plot in Figure 1.61 is semi-logarithmic, and shows clearly that several samples show more than one peak. In particular, the defect-related peak in ZnO, faintly observable in Figure 1.60, is obvious in Figure 1.61.

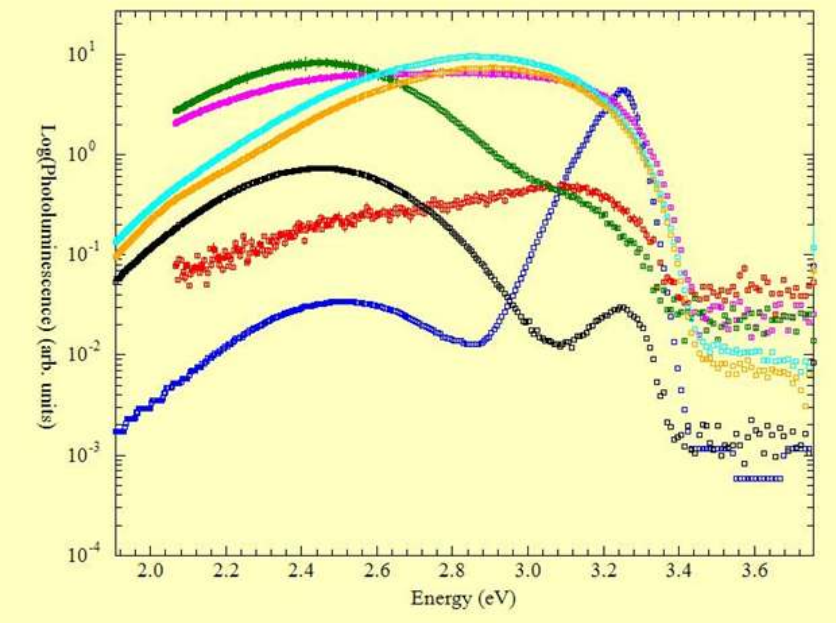

Figure 1.61. Photoluminescence of consolidated nanoparticle thin films.

The two sonosprayed samples starting with 15% solution (Cyan and Orange) show very similar PL spectra that start just below the band gap of ZnO and are very broad. The single layer sample (Black) shows a broad PL peak near 2.5 eV, similar to that seen in the crystalline ZnO, but with an additional peak near 3.28 eV, reminiscent of the excitonic peak of ZnO.

Photoluminescence (PL) is clearly a very powerful tool for the examination of ZnS materials made from NanoFermentation nanoparticles. From solutions of NanoFermentation nanoparticles, we found that there was a correlation with the PL spectra and the estimated particle size, but the correlation was weak and contrary to the expected behavior; this is probably because our samples consisted of a wide distribution of particle sizes, as well as some other materials. Consolidated films of ZnS material show quite different PL spectra, depending on fabrication and post-fabrication annealing. When the samples were treated in air, there was evidence of ZnO being present, as well as other below-bandgap defects.

As a next step, ZnS particles were annealed at different temperatures in inert and O_2 atmosphere to gain an understanding of the phase formation. The impact of the processing temperature on ZnS particle crystallinity was analyzed by x-ray diffraction (XRD) technique. The PL response of NF ZnS material was measured on discrete powder samples, and thin films deposited on quartz and alumina substrates. The photoemission performance of the nanoparticles was evaluated in terms of PL quantum efficiency. Table 1.14 lists the information on key samples that were used in the present study.

Table 1.14 NF ZnS samples annealed at various conditions

Label	Sample ID	Particle Size	Substrate	Annealing Investigation (Ar atmosphere)
120615A01	A	3.1nm	Quartz	
	B	3.1nm	Quartz	400°C/30min
	C	3.1nm	Quartz	600°/30min
120823A01	A	7.4nm	Quartz	
	B	7.4nm	Quartz	400°C/30min
	C	7.4nm	Quartz	600°/30min
120926A01	A	9.5nm	Quartz	
	B	9.5nm	Quartz	400°C/30min
	C	9.5nm	Quartz	600°/30min
Aldrich 10%ZnS	A	10μm	Quartz	
	B	10μm	Quartz	400°C/30min
	C	10μm	Quartz	600°/30min

Label	Sample ID	Particle Size	Substrate	Annealing Investigation
120926A01	A	9.5nm	Alumina	Annealing
	B	9.5nm	Alumina	Films will be anneaed at
	C	9.5nm	Alumina	400 and 600°C in air and
	D	9.5nm	Alumina	Ar atmospheres
	E	9.5nm	Alumina	

Figure 1.62 shows the PL response of discrete ZnS particles (9.5 nm) annealed at different temperatures. A comparison with the PL response of as-processed particles and single crystal ZnO reference has also been made to evaluate the performance. The samples were excited with a 325nm (He-Cd laser) optical signal for PL measurements, and the PL emission was detected with a photomultiplier tube. The photomultiplier tube (PMT) voltage was 401V, and not changed during the measurements. Data was taken from 330 to 850 nm in steps of 2 nm, but cut off at 750 nm due to the insensitivity of the PMT above 750 nm. The main points to note from Figure 1.62 are as follows:

- The ZnO reference sample shows near-band gap excitonic PL, a second, larger peak from a related defect, and a much stronger interband defect PL near 500 nm.
- The ZnS samples showed different PL, depending on heat treatment. As synthesized showed some UV PL, starting at the ZnO band edge, decaying slowly into the band gap (lower energy/higher wavelength).
- Annealing at 200 and 400 °C changed the PL spectra, mainly by moving the peak energy to lower energy/higher wavelength. *However, the 600°C anneal dramatically increased the PL*; note that the PL signal (red) is 200 times that of the other ZnS samples, and 10 times that of the ZnO. When the 325 laser was incident upon the 600°C annealed sample, the glow was really bright and appeared white.
- Detailed measurements were made to understand the origin of strong PL emission from the samples annealed at 600°C to further control the emission characteristics for optoelectronic applications.

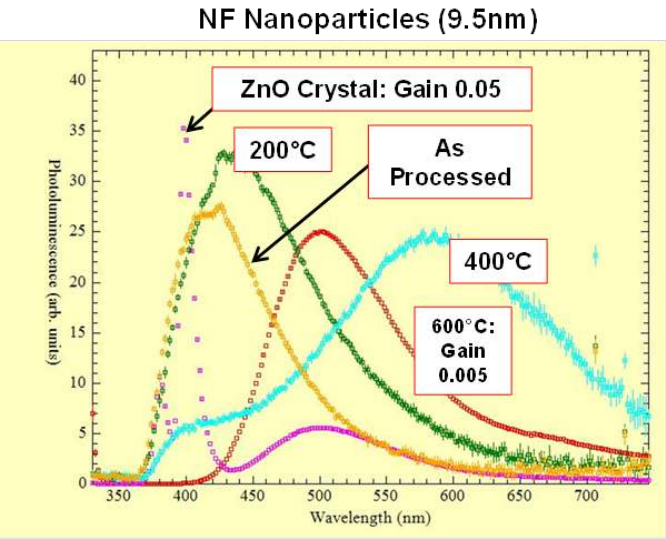

Figure 1.62. The PL response of as-deposited and annealed NF ZnS particles.

XRD measurements were also made to establish a correlation between the PL response and the phase-evolution. The NF ZnS sample was annealed in a box furnace in flowing N_2 atmosphere. As shown in Figure 1.63, the ZnS sample changed to ZnO after annealing at 600°C possibly due to residual oxygen in the atmosphere. The nitrogen partial pressure was not sufficient to suppress oxidation. Based on the XRD results; further annealing studies were carried out in a tube furnace with controlled atmosphere. The impact of the annealing in inert gas and oxygen atmospheres on the NF ZnS properties was analyzed in detail as discussed in sections below, to understand and control the optical characteristics of NF ZnS nanoparticles.

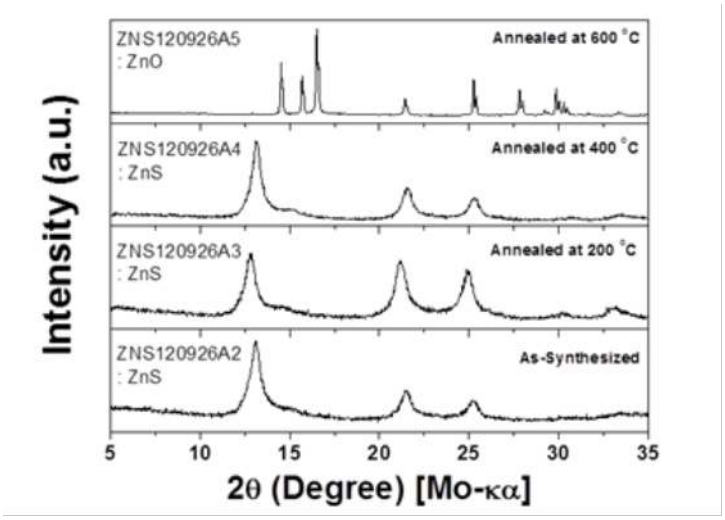

Figure 1.63. The XRD patterns of as-deposited and annealed NF ZnS particles (9.5nm).

2.3.4 NF ZnS Thin Films

An annealing study was conducted on NF ZnS (4.7nm) thin films to analyze the impact of temperature on the PL response and crystallinity. The films were annealed in a box furnace in flowing N_2 atmosphere. The performance of the thin film samples was very similar to the annealed

discrete particles. The XRD measurements, as shown in Figure 1.64, did not show the formation of ZnO phase up at 400°C. However, annealing at 600°C resulted in a well-defined ZnO phase indicating that residual oxygen was enough to effectively oxidize the ZnS material. The as-deposited ZnS thin films showed a PL signal peaking at around 440nm. After annealing, the PL peak shifted to longer wavelengths. The XRD and PL results indicate that a control of annealing atmosphere is critical for ZnS material. At the same time the possibility of converting ZnS nanoparticle into ZnO nanoparticle opens up the possibility of targeting novel electronic applications exploiting its unique electronic properties.

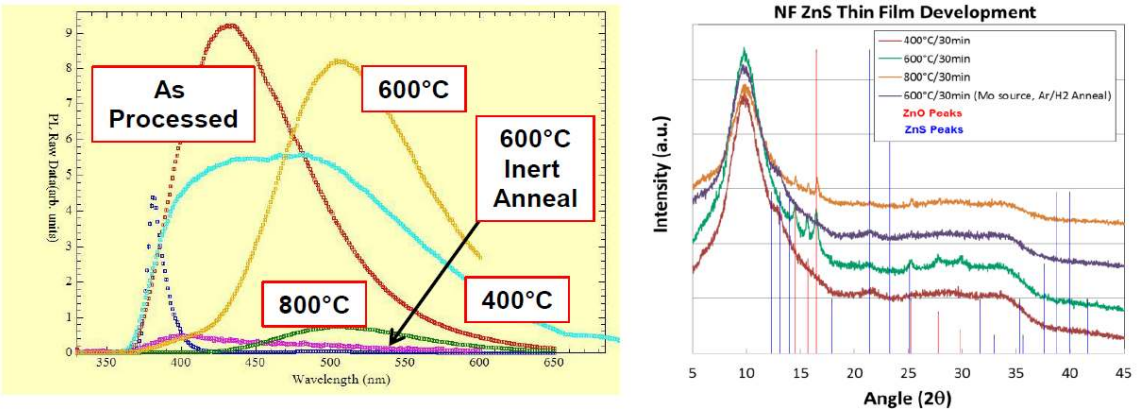

Figure 1.64. The impact of annealing on the (a) PL response and (b) crystallinity of NF ZnS thin films.

A number of ZnS thin film specimens were annealed in an inert atmosphere. The effects of the particle size on the microstructure and PL response were analyzed on the nanofermentation processed (<10nm) and commercial ZnS particles (~10µm). Figure 1.65 shows the PL response of the as-processed NF ZnS thin films (9.5nm). The NF ZnS thin films showed a broad PL signal peaking at around 410 nm which matches well with the PL emission (400-450 nm) wavelengths typically reported for ZnS particles processed by chemical methods. The large commercial particles did not show any appreciable PL response that could be used as a reference for the present study.

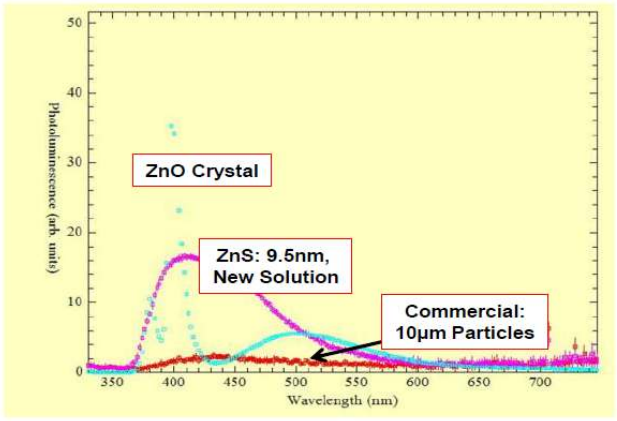

Figure 1.65. The typical PL response of as-deposited NF ZnS nanoparticles.

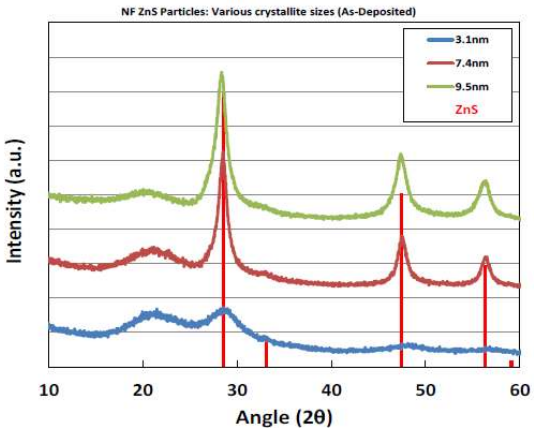

Figure 1.66. The XRD patterns of the as-deposited NF ZnS nanoparticle (3.1-9.5nm) thin films.

The NF ZnS thin films were annealed at various temperatures in a controlled inert and oxygen atmospheres to analyze the impact of annealing and particle size on the crystallinity and photo-response characteristics. Figure 1.66 shows the XRD patterns of the as-processed NF ZnS

nanoparticles (3.1-9.5 nm). The XRD patterns indicated the formation of a well-crystallized ZnS phase with no appreciable dependence on the particle size. The signal intensity was dictated by the material quantity exposed to the XRD beam rather than the material characteristics.

The NF ZnS thin films were also annealed in a pure oxygen atmosphere to analyze the impact of oxygen on the physical characteristics and crystallinity. As shown in Figure 1.67, the film color did not change appreciably after annealing in oxygen atmosphere. It may possibly be due to oxidation of the carbon and other impurities during annealing.

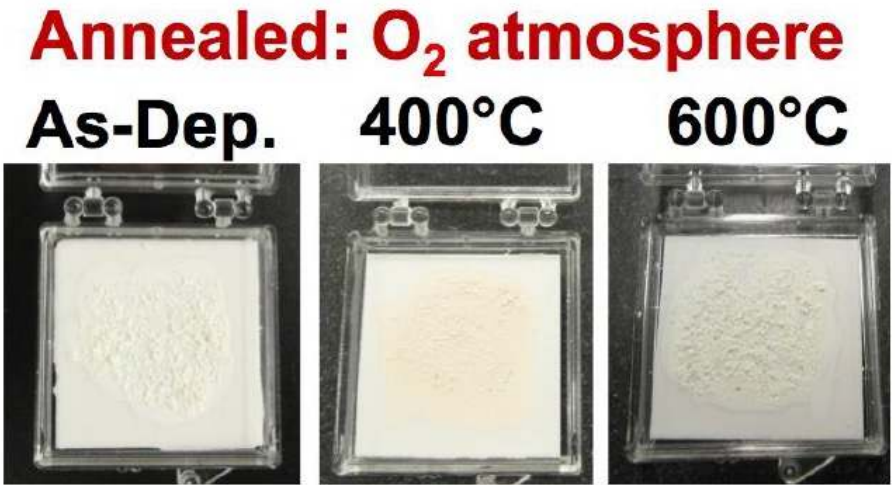

Figure 1.67. The NF ZnS thin films did not show any color change after annealing in an oxygen atmosphere as was observed after annealing in Ar atmosphere.

Figure 1.68 shows the XRD patterns of the films annealed in a pure oxygen atmosphere. The oxidation behavior of the NF ZnS thin film annealed in a 100% oxygen atmosphere appears to be similar to the films annealed in a box-furnace with residual oxygen. The ZnS phase is not significantly influenced by annealing at 400°C. However, a highly crystalline ZnO phase is formed after annealing at 600°C.

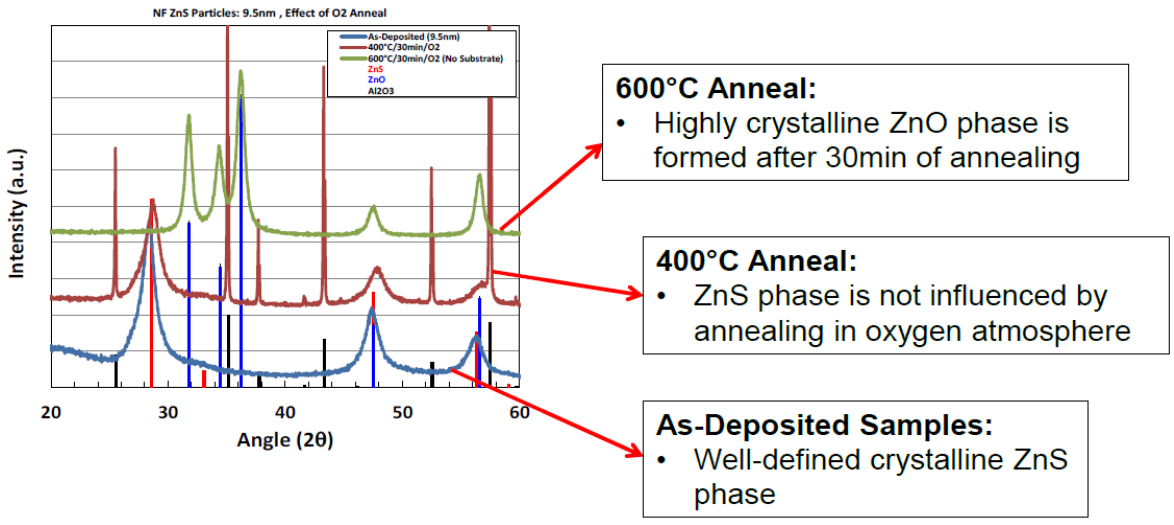

Figure 1.68. The impact of annealing in a pure oxygen atmosphere on the crystallinity and oxidation of NF ZnS thin films.

The absolute QE of the sample is determined by comparing similar measurements of the laser beam with no sample in place with the spectral relative QE with the sample in place. Figure 1.69 shows the spectrum near 325 nm for the system with no sample (blue) and with the sample. The number of 325 nm photons is then proportional to the integration of the above equation for QE over the line width. We also show the spectrum of the laser line with the sample in place. The reflectivity of the sample can then be determined as the ratio of the integrals of the two lines, and is 7.2% for this sample.

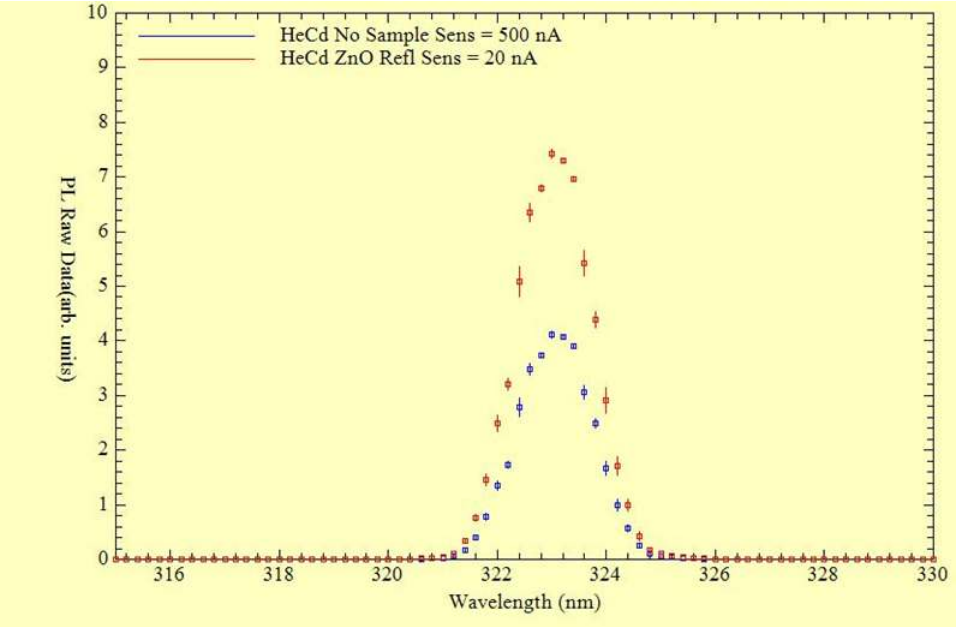

Figure 1.69. Photoluminescence spectrum with no sample (blue) and with a sample (red) in place.

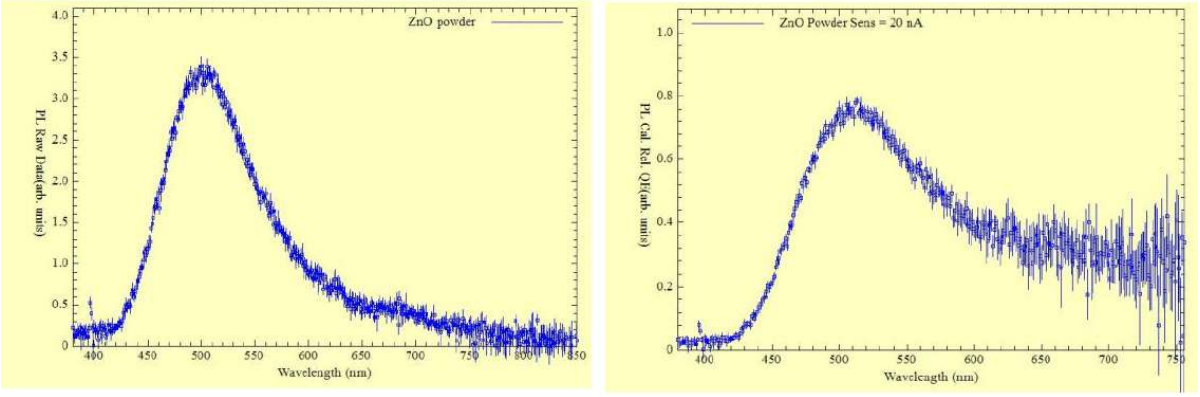

Figure 1.70. (a) – Raw photoluminescence data for ZnO sample, and (b) - Quantum efficiency data for ZnO sample.

Figure 1.70a shows the spectrum from the ZnO sample in raw data units and Figure 1.70b shows the same spectrum in relative QE units. The large errors in the data at long wavelengths are due primarily to the lower quantum efficiency of the PMT in this range, as well as the Wavelength multiplication factor in the equation above. By integrating the relative QE spectrum above from 400 to 750 nm and comparing with the integration over the HeCd spectral line (Fig. 1.69), we determine that the QE of the sample is 2.5%.

2.3.5 Preparation of the ZnO NFNP target for low temperature senor deposition

The deposition of NF ZnO was scalable with the pulse laser vaporization process, where the powder target was held in rotating holder in the vacuum chamber and laser pulses were used to remove material from the target and deposit it on preheated substrate. The deposition conditions were with a laser wavelength of 248 nm at 5Hz with a total of 5000 pulses, and the target positioned at a 5 cm distance from the substrate. The nanofermented NP ZnS was converted to ZnO under heating at 1100C in air for 1 hour resulting in the formation of stoichiometric oxide. The target was prepared from prewashed ZnO compressed using 6 ton press (see Figure 1.71). An optical image of the target is shown in inset photograph of Figure 1.71.

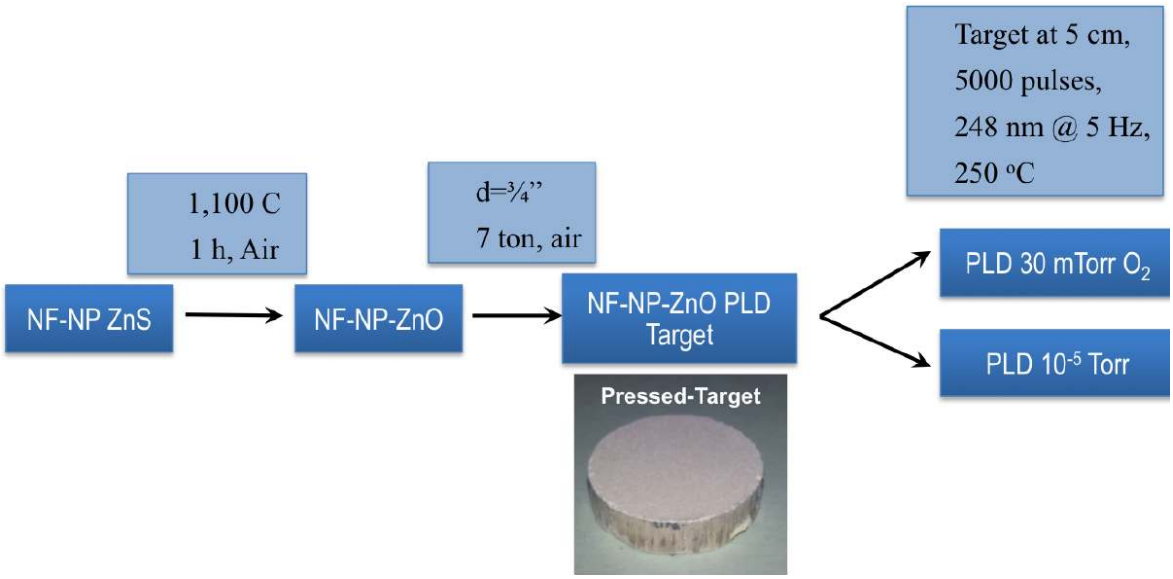

Figure 1.71. Flow chart of the sample preparation using a pressed target made from nanofermented NP.

The thin film of ZnO was deposited on the surface of pre-cleaned Si wafer with 150nm layer of thermal oxide to realize configuration of transistor with back gating. The films were deposited at two conditions (vacuum and 30mTorr of background oxygen. In both cases the substrate was preheated to 250 or 400 C to assist with formation of continuous film of ZnO. Figure 1.71 shows a flow chart of the sample preparation. Processing of NF-ZnO NP films is compatible with thin-film technologies (sputtering, PLD). This process is also compatible with low-cost, low-temperature processing thereby enabling flexible-electronics**.**

2.4 THIN FILM ANNEALING AND CHARACTERIZATION – ZN GALLATE COATINGS

The Zn Gallate coatings fabricated in the subtasks outlined above were annealed at various temperatures in normal air atmosphere. Figure 1.72 shows the x-ray diffraction (XRD) patterns of the various films annealed at 950°C. Both the Zn Gallate and substrate peaks are clearly visible in the XRD patterns. The Zn Gallate phase appears to be well-defined after annealing at 950°C. The doping did not appear to have any appreciable impact on the XRD patterns. The lattice constant value was found to be in the range of 8.340-8.341Å for all the samples.

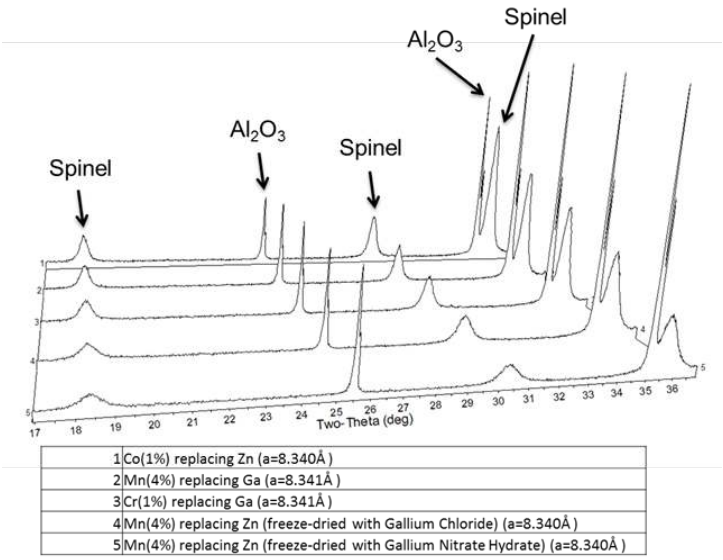

Figure 1.72. The X-ray diffraction patterns of the ZnGa2O4/Al2O3 coatings annealed at 950°C.

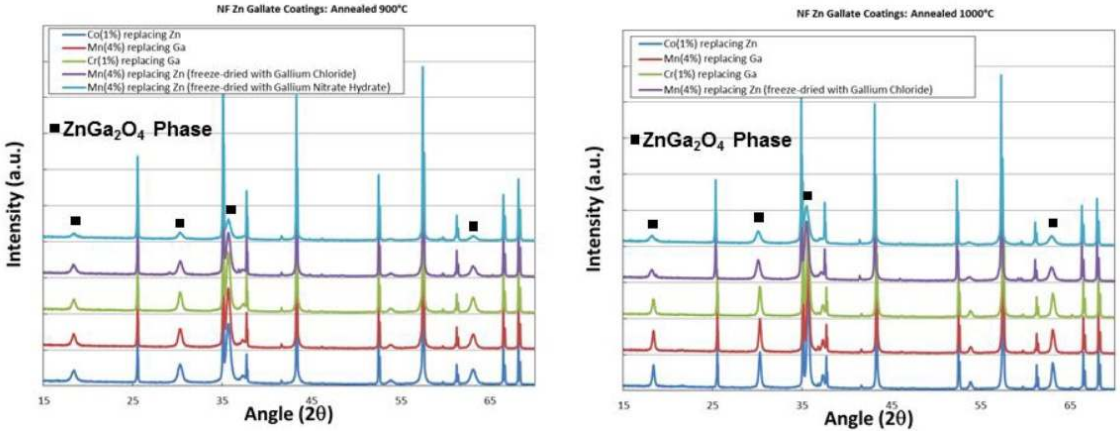

Figure 1.73. The X-ray diffraction patterns of the $ZnGa_2O_4/Al_2O_3$ coatings annealed at various temperatures: (a) 900°C, (b) 950°C, and (c) 1000°C. The unlabeled peaks are due to the substrate.

The XRD patterns of the coatings annealed at 900 and 1000°C are shown in Figure 1.73. The XRD patterns indicated the formation of a well-defined spinel phase at 900°C. Annealing at a higher temperature of 1000°C resulted in sharper peaks for all the samples indicating an increase in the crystallinity of the Zn Gallate coatings. Further annealing study will be conducted in the expanded temperature range of 600-1100°C to gain a clear idea of the factors influencing the Zn Gallate phase formation, and the impact of crystallinity on the optical and electrical characteristics of the thick Zn Gallate coatings.

2.4.1 Photoluminescence

The photoluminescence characteristics of the Zn Gallate coatings annealed at 900°C are shown in Fig. 1.75. The PL measurements were conducted at room temperature. The PL was excited by a 325nm He-Cd laser. The ZnO single crystal reference signal is also shown in Figure 1.74 for comparison. All the Zn Gallate coatings exhibited multiple peaks in the UV and visible part of the spectrum. The strongest PL response was observed for the Cr doped sample while the Mn doped samples showed the best response in the blue-green part of the spectrum, which is attractive for commercial applications.

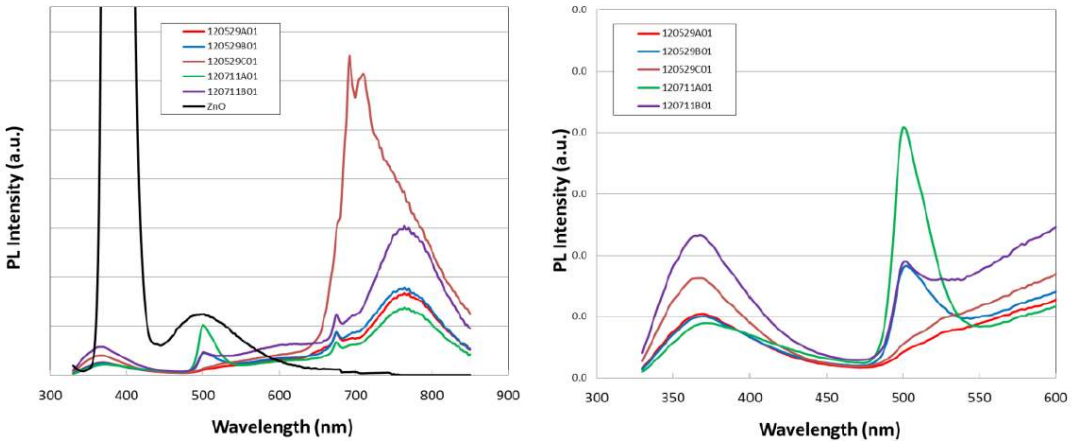

Figure 1.74. The PL response of various $ZnGa_2O_4$ coatings annealed at 900°C: (a) full spectrum (330-850nm), (b) expanded view below 600 nm. Sample details: • Co(1%) replacing Zn, • Mn (4%) replacing Ga, • Cr(1%) replacing Ga, • Mn(4%) replacing Zn (freeze dried with Gallium Chloride, •Mn(4%) replacing Zn (freeze dried with Gallium Nitrate Hydrate)

As shown in Fig. 1.75, the PL intensity was found to increase with an increase in the annealing temperature in the range of 900-1000°C. The observed results are consistent with the XRD patterns showing sharper peaks at higher annealing temperatures. The impacts of the annealing temperature and atmosphere will be analyzed in details to gain a clear understanding of the factors influencing the optical emission characteristics.

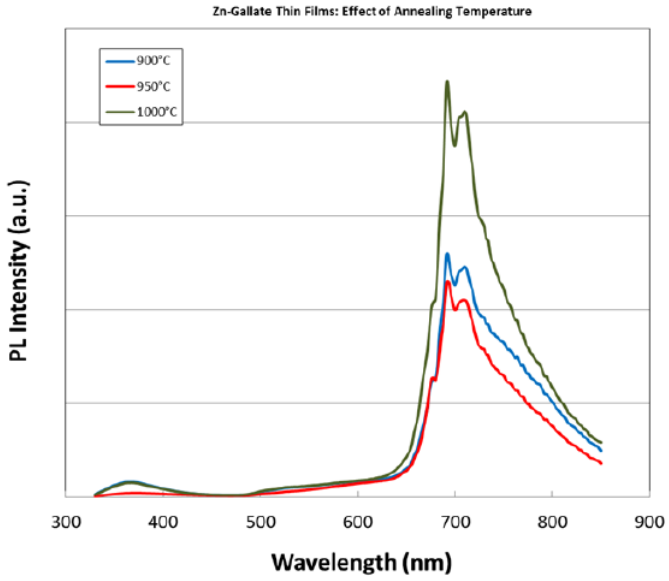

Figure 1.75. The effect of annealing temperature on the PL response of doped ZnGa2O4 (1% Cr

replacing Ga) coatings.

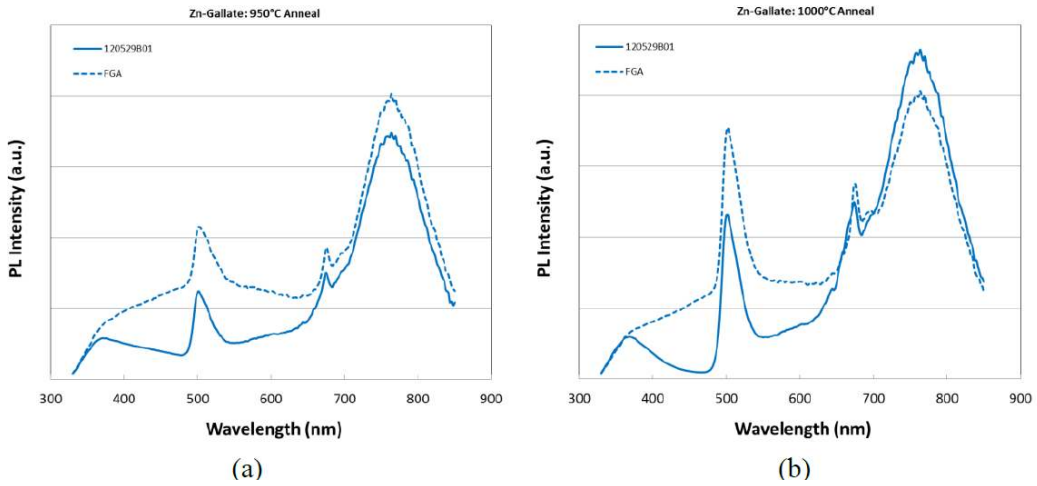

Figure 1.76. The effect of forming gas anneal on the PL response of doped $ZnGa_2O_4$ (Mn (4%) replacing Ga) coatings annealed at (a) 950°C and (b) 1000°C.

The effects of forming gas annealing (FGA) on the PL response of the Mn (4%) doped Zn Gallate coatings were also analyzed as shown in Figure 1.76. The FGA was conducted at 450°C for 60 minutes in a flowing Ar/H_2 (4%) atmosphere. The FGA at a significantly lower temperature than the annealing temperature was effective in improving the PL response of the Zn Gallate coatings indicating that material defects are influencing the optical emission characteristics. A systematic FGA study was conducted to find the optimum processing window for defect passivation without deteriorating the material quality in a reducing hydrogen atmosphere.

The impact of doping on the PL emission characteristics of Zn Gallate films were investigated in detail as shown in Fig. 1.77, to develop a wide-band phosphor material. Cr doped Zn Gallate films were selected for the present study as they exhibited the strongest PL response among various doped films. The Zn Gallate material performance was being evaluated in terms of the ink stability, coating quality control, particle crystallinity, PL response of intrinsic/doped coatings, and electrical conductivity. The sample splits for the annealing investigation are listed in Table 1.15. The Zn Gallate coatings were processed in order to analyze the impact of post-deposition annealing temperature on the material structure and photoluminescence characteristics. The results of our investigation are presented below.

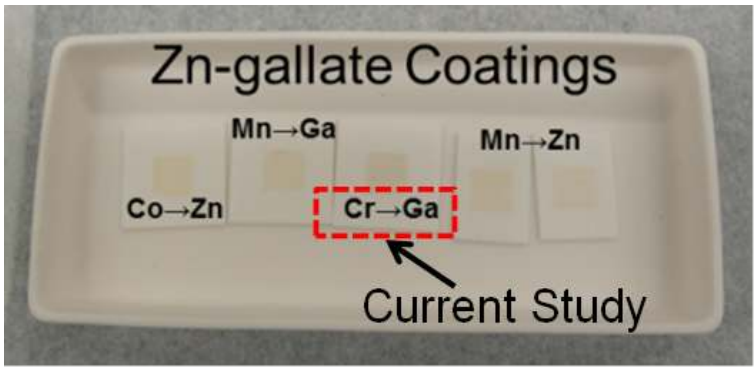

Figure 1.77. Various dopants under investigation for optical emission control for phosphor applications.

Table 1.15 Zinc Gallate sample splits for annealing investigation

Sample ID (Zn-Gallate, Cr replacing Ga (1%)	Annealing	Atmosphere	Forming Gas Anneal
ZCT100529C01_900CO	900°C/30min	O_2	450°C/60min
ZCT100529C01_1000CO	1000°C/30min	O_2	450°C/60min
ZCT100529C01_1100CO	1100°C/30min	O_2	450°C/60min
ZCT100529C01_1100CA	1100°C/30min	Air	450°C/60min

2.4.2 Crystallinity

The Cr doped Zn Gallate films were annealed in the temperature range of 900-1100°C in air and pure oxygen atmospheres to analyze the impact of annealing atmosphere on the material structure. As shown in Fig. 1.78(a); the Zn Gallate spinel phase was well-formed at an annealing temperature of 900°C. Only the stoichiometric Zn Gallate and substrate peaks were observed in the XRD patterns. The film crystallinity was found to improve with an increase in annealing temperature to 1000°C. Annealing at a higher temperature of 1100°C resulted in substantially sharper peaks in the XRD pattern indicating significant improvement in film crystallinity and grain growth. Similar XRD patterns were observed for the films annealed in air and oxygen atmospheres; as shown in Fig. 1.78(b), indicating that the as processed nanoparticle films have sufficient oxygen for a stoichiometric phase formation. The x-ray photoelectron spectroscopy (XPS) measurements will be conducted to further analyze the elemental composition of the films and correlate it to the observed XRD results for a clear understanding of the phase formation kinetics.

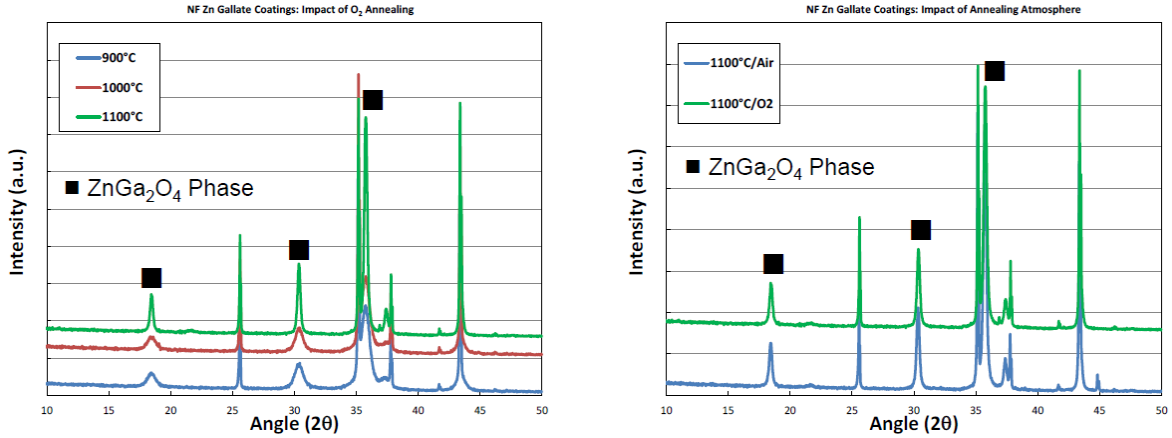

Figure 1.78. The x-ray diffraction patterns of the $ZnGa_2O_4/Al_2O_3$ coatings annealed at various temperatures: (a) 900-1100° anneal in oxygen atmosphere, (b) 1100°C anneal in air and oxygen atmospheres.

2.4.3 Photoluminescence of Annealed Coatings

The photoluminescence characteristics of the annealed Cr doped Zn Gallate coatings are shown in Fig. 1.79. The films were annealed in the temperature range of 900-1100°C in a flowing oxygen

atmosphere. The PL measurements were conducted at room temperature using a 325nm He-Cd laser for excitation. The Cr doped Zn Gallate films exhibited strong PL response in the red part of the spectrum. The PL response was not influenced by the annealing atmosphere nor the annealing temperature in the range of 900-1100°C, while the XRD patterns indicated a substantial improvement in film crystallinity. A correlation among the PL response, material crystallinity, and dopant concentration need to be established to further improve the photoemission characteristics; which will be the focus of our future investigation.

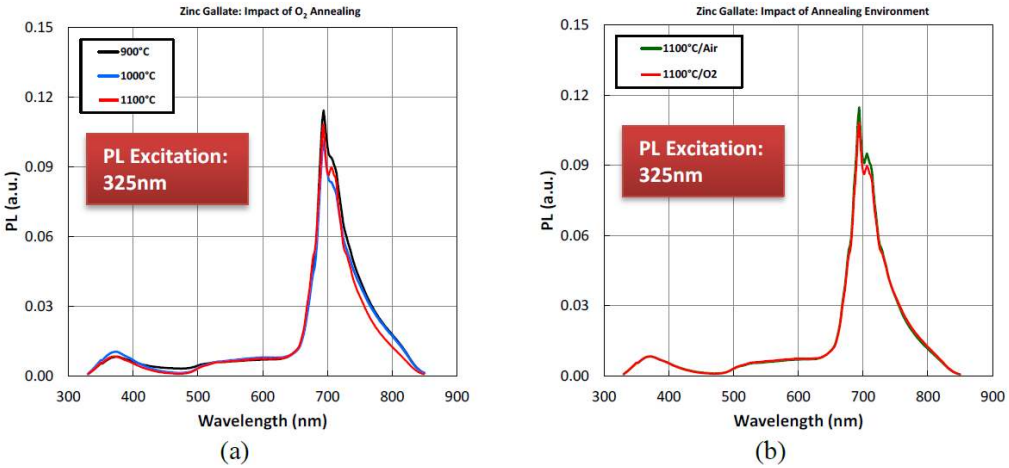

Figure 1.79. The PL response of the $ZnGa_2O_4$ coatings annealed at various temperatures: (a) 900-1100° anneal in oxygen atmosphere, (b) 1100°C anneal in air and oxygen atmospheres.

The effects of forming gas annealing (FGA) on the PL response of the Cr doped Zn Gallate coatings were also analyzed as shown in Fig. 1.80. The FGA was conducted at 450°C for 60 minutes in a flowing Ar/H_2 (4%) atmosphere. The FGA did not result in any appreciable improvement of the PL response of the Cr doped Zn Gallate films. The PL response was found to be similar for both the air and oxygen atmosphere annealed films. The observed PL response suggests that the optical emission characteristics were not limited by defect related absorptions in the bulk of the material. We will continue our investigation of the defect structure and defect-passivation in various intrinsic and doped Zn Gallate films for the development of an efficient phosphor.

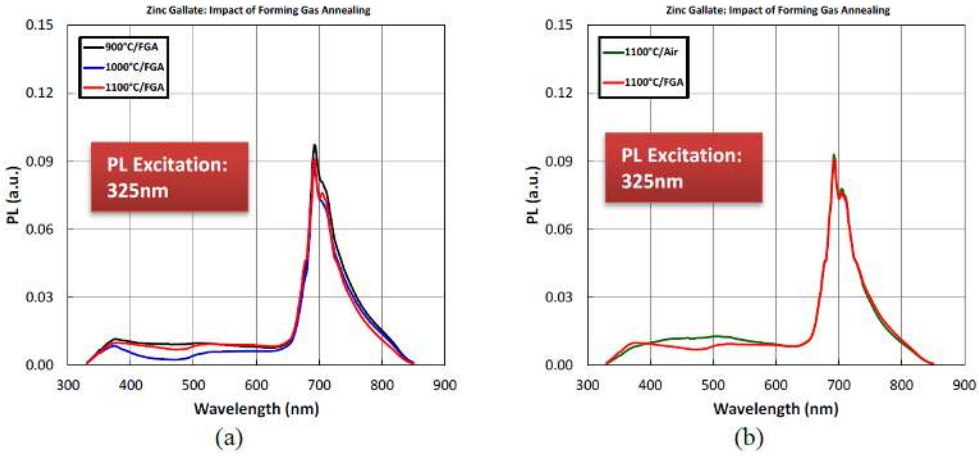

Figure 1.80. The impact of forming gas anneal on PL response of the $ZnGa_2O_4$ coatings processed at various temperatures: (a) 900-1100° anneal in oxygen atmosphere, (b) 1100°C anneal in air and oxygen atmospheres.

2.4.4 PL Quantum Efficiency

The PL quantum efficiency (PLQE) measurements were conducted both on Cr doped Zn Gallate films deposited on alumina and silica substrates and on Cr-doped Zn Gallate powders. The films were annealed at a temperature of 1000°C. The Cr doped Zn Gallate films deposited on alumina substrates exhibited appreciable background signal resulting from the PL from the substrate. As a result, the evaluation of the material PLQE was determined using Cr-doped Zn Gallate samples formed on fused silica substrates. The resulting PLQE (600-850 nm) was 0.95±0.07% using PL excitation of 325 nm. If Cr-doped Zn Gallate powder samples are examined, then a PLQE (600-850 nm) of 1.9±0.2% was obtained**.**

The photoluminescence measurements continued with 4 different samples of zinc gallate powder as listed in Table 1.16. All the samples were annealed at a temperature of 1100°C for 30 minutes in a flowing oxygen atmosphere. The impact of nanofermentation process on the zinc gallate particles quality was analyzed in terms of the photo-response characteristics. The photo-response of the zinc gallate material was evaluated in terms of the photoluminescence (PL) characteristics. The PL illumination wavelength was 325 nm and the optical configuration was without the integrating sphere.

Table 1.16 Zinc Gallate sample splits for PL investigation. All samples were annealed in O_2 atmosphere

Sample ID	Crystallite Size	Annealing Temperature/Time	NF Process Details
ZGT130716 A01	3.2±0.1 nm	1100°C/30min	All (Precursor +MOPS) at initial 2 weeks
ZGT130716 B01	3.0±0.1 nm	1100°C/30min	(precursor + MOPS) after 1 day for 1 week
ZGT130716 C01	3.0±0.1 nm	1100°C/30min	(precursor + MOPS) after 1 day for 2 week
ZGT130716 D01	3.4±0.1 nm	1100°C/30min	(precursor + NaOH) after 1 day for 1 week

The plot of the photoluminescence is shown in Figure 1.81. As can be seen, all samples show a strong PL around 500 nm, and another series of PL peaks in the 670 nm range. Note that the 670 nm PL is real and not due to second order diffraction of the 325 nm laser line, since a color filter is used to eliminate the second order light. Figure 5 documents the photoluminescence response for various annealing conditions of Zn gallate thin films.

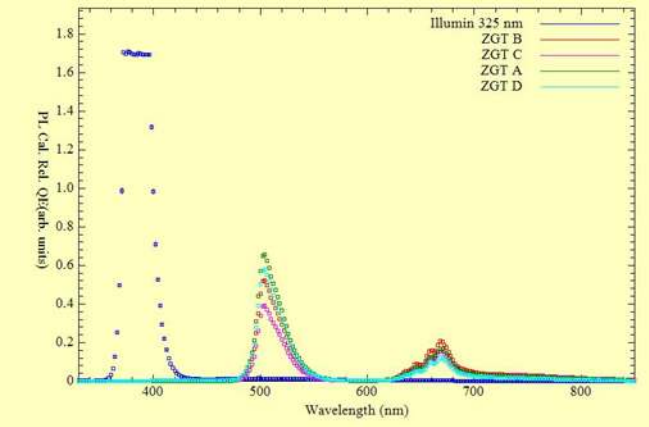

Figure 1.81. Photoluminescence from 4 different zinc gallate samples, and the photoluminescence from a standard ZnO sample (blue and off scale).

The PL system was then re-configured to obtain the quantum efficiency using the technique described in a previous report. Here, the 325 nm laser beam is used for illumination, but the sample powder is inserted into an integrating sphere so that all light emitted from the sample can be detected. As with all integrating sphere measurements, the signal was considerably less than the open-air experiments used for the data shown in Fig. 1.81. To improve the signal-to-noise, the slit on the monochromator was increased to 1 mm. Figure 1.82 shows the light intensity collected without the sample and with the sample near the 325 nm laser line. By integrating the intensities, the reflectivity of the powder was determined to be 38.0±0.1%.

Figure 1.83 shows the PL of zinc gallate in the integrating sphere. The signal strength of the data shown in Fig. 1.83 was considerably less than that of Fig 1.81 by a factor of 10^4, resulting in the increased noise as shown in Fig. 1.83. By taking the ratio of the integrated intensity of the data in Fig. 1.83 compared to the intensity of the laser light (Fig. 1.82), we get the quantum efficiency (QE) of 1.02±0.01%.

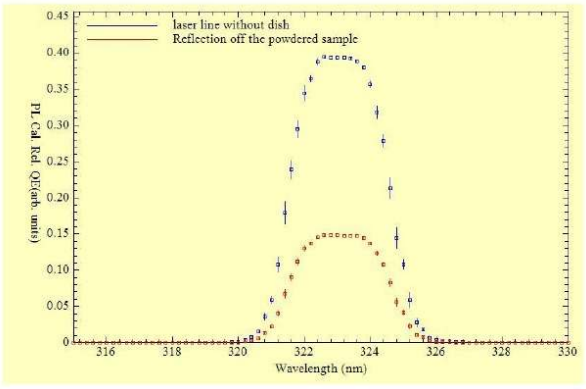

Figure 1.82. The impact of sample reflectivity on the collected PL excitation signal.

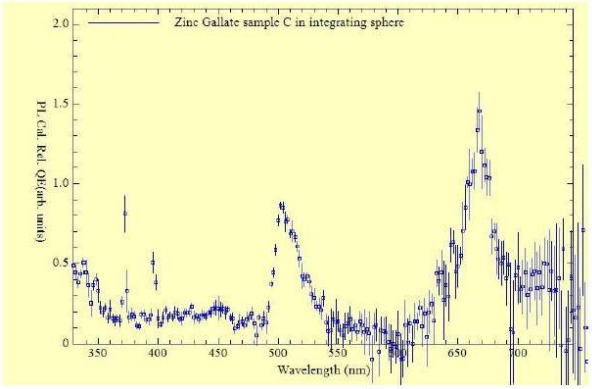

Figure 1.83. Photoluminescence of Zinc Gallate taken in the quantum efficiency configuration.

2.4.5 Effect of Annealing on Zinc Gallate Crystallinity

The samples listed in Table 1.17 were annealed at 1100°C for 30 minutes to enhance crystallinity and PL response characteristics. For the present batch of samples, the Zn/Mn/Ga ratio was varied to analyze the impact of divalent cation concentration on the microstructure and PL response. As shown

in Figure 1.84, all the samples exhibited a well-defined crystallized $ZnGa_2O_4$ phase. The XRD peak intensity and sharpness were found to improve significantly as a result of annealing. The Ga-O and GaO(OH) phases were also observed for the present samples.

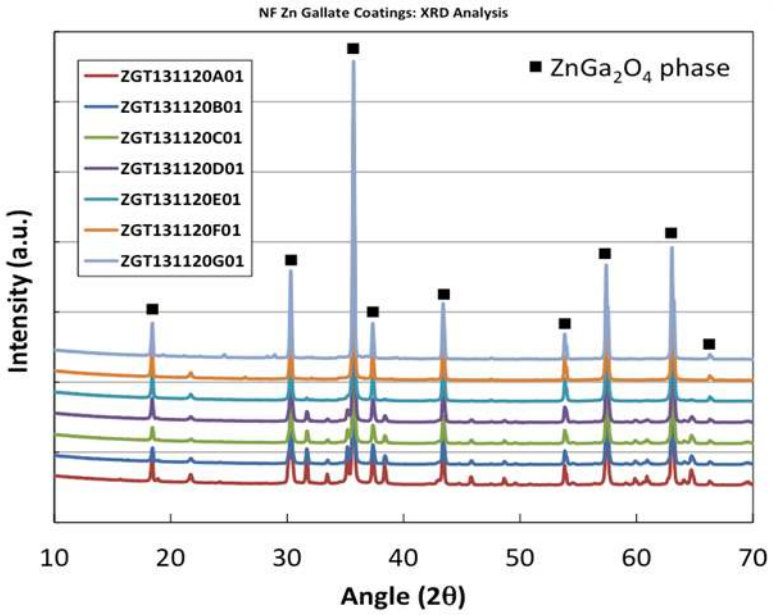

Figure 1.84. X-ray diffraction patterns of annealed zinc gallate particles with various ([Zn]+[Mn])/[Ga] ratios.

2.4.6 Photoluminescence of Zinc Gallate Powder Made by Nanofermentation

Photoluminescence (PL) studies were performed on several zinc gallate (ZGT) samples ZGT131120A-G, where the last letter indicates a variation in the composition of the samples. The primary compositional variation in samples A-G is the zinc to gallium ratio ($Zn_{1\pm0.3}$:Ga_2), where all samples are doped with ~4% Mn All samples had been annealed at 1100 °C for 30 min. These are briefly described in Table 1.17 with a more complete description given below. For comparison purposes, the PL from a trichromatic phosphor (used in fluorescent lamps) was also examined. All samples were in the form of a powder.

Table 1.17 ZGT131120 samples examined using photoluminescence

Sample	Stoichiometry	Ave. Size (nm)
A	$Zn_{0.7}Ga_2$	2.5±0.1
B	$Zn_{0.8}Ga_2$	2.8±0.1
C	$Zn_{0.9}Ga_2$	3.0±0.2
D	$Zn_{1.0}Ga_2$	3.0±0.1
E	$Zn_{1.1}Ga_2$	3.6±0.2
F	$Zn_{1.2}Ga_2$	3.5±0.1
G	$Zn_{1.3}Ga_2$	3.8±0.2

The ZGT samples as presented contained very little material, so it was not possible to perform variable excitation samples using the Fluorimeter at CNMS. Therefore, we performed the PL measurements using the system in the CATS lab. Two excitation sources were used; a HeCd laser (325 nm) and a white light HgXe arc lamp. The HgXe arc lamp emits a broad spectrum of light with

significant intensity in many of the standard Hg lines. We used standard narrow-pass interference filters (10 nm full width at half max band width, ~15% maximum transmission) to select out the specific wavelengths used to illuminate the sample. The HeCd laser emits ~20 mW of light energy, while the energy of the light from the filtered HgXe lamp was nearly 3 orders of magnitude less. Four Hg lines were examined: 1) 254 nm (11 μW), 2) 313 nm (56 μW), 3) 365 nm (61 μW), and 4) 405 nm (18 μW).

The small amount of sample also precluded us from performing integrating sphere measurements to determine the quantum efficiency (QE) of the emitted PL. As a result, we compared the PL from the ZGT samples with the trichromatic phosphor, and report the QE relative to the trichromatic phosphor. No corrections were made for reflection losses.

Figure 1.85 shows the PL for the trichromatic sample using the 4 different illumination energies from the HgXe lamp, normalized for the number of illumination photons. The spectra were taken from 330-850 nm, so the 254 nm and 313 nm data do not show the excitation source, but the 365 nm and 405 nm spectra do show a significant peak at the illumination wavelength (this is just the reflected light from the powder). The trichromatic phosphor was designed to operate using 254 nm excitation, and it contained Y_2O_3:Eu, which emits at 611 nm and several other red wavelengths when illuminated with 254 nm light. These emission wavelengths were not present when the trichromatic was illuminated using longer wavelengths, since the Y_2O_3:Eu component was not excited. The broad blue PL is strongly excited by both 313 nm and 365 nm light.

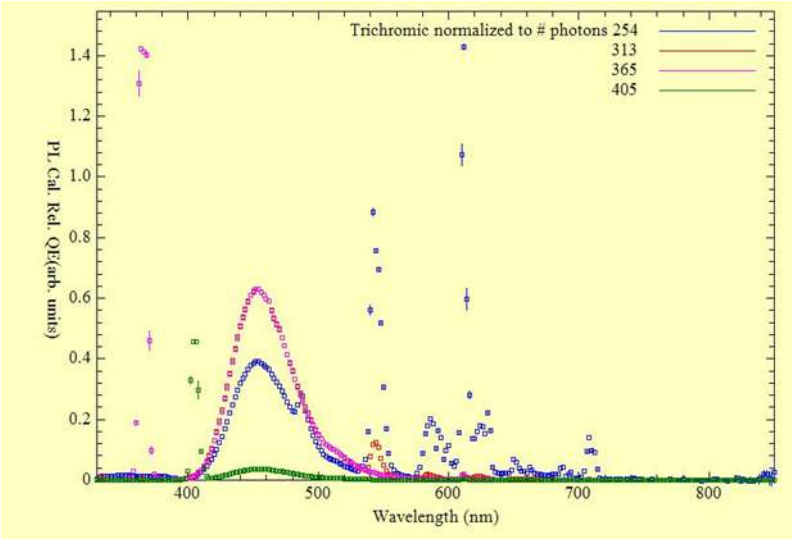

Figure 1.85. Photoluminescence spectra from the trichromatic phosphor using 4 different excitation wavelengths.

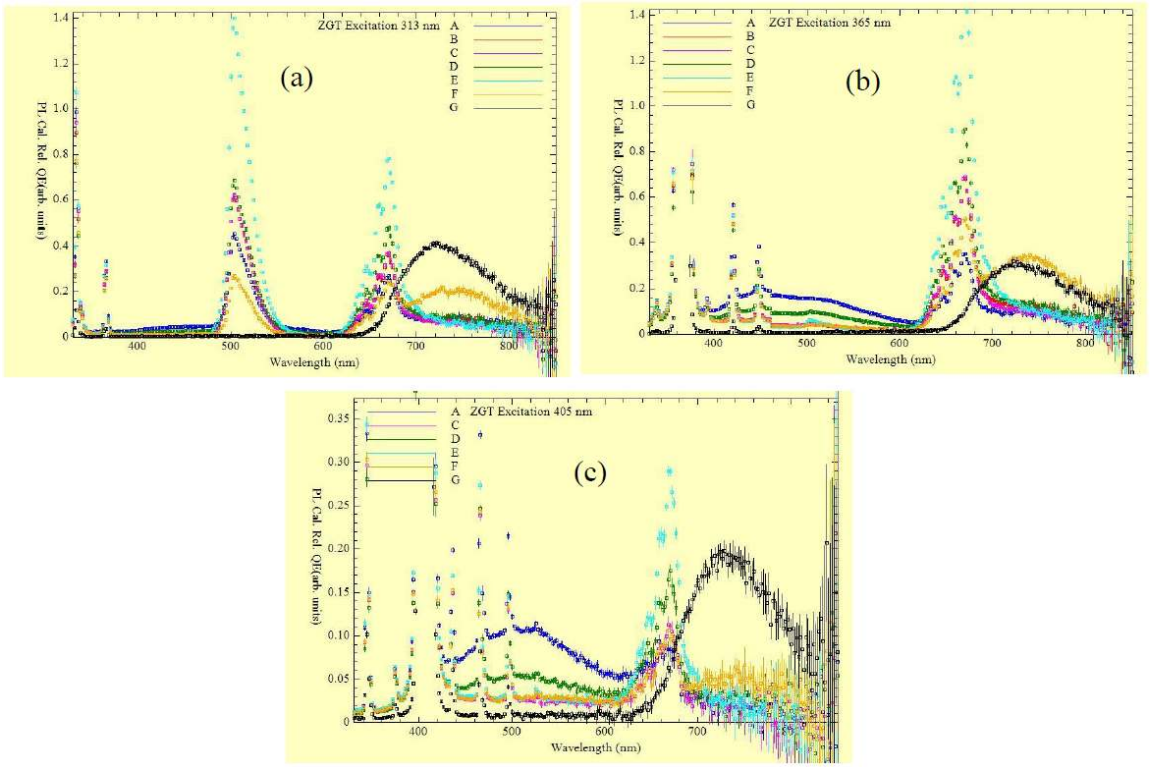

Figure 1.86. Photoluminescence from the various ZGT samples when illuminated using various wavelengths from the HgXe lamp. Illumination using the 254 nm wavelength showed no observable PL, so it is not shown.

No observable PL was observed from the ZGT samples when excited by 254 nm light, but significant PL was observed when excited using 313 nm, 365 nm, and 405 nm light. This data is shown in Figure 1.86a. When illuminated using 313 nm excitation, all samples exhibited a strong peak near 338 nm (A-F; 334 nm for G) and 365 nm (A-F, weak for G). Strong broad transitions were observed near 505 nm and 670 nm arising from transitions in Mn^{+2} in samples A-F, while samples G and F exhibit a very broad transition at 730 nm. Sample G did not show the broad transitions at 505 nm and 670 nm.

If the samples were illuminated using 365 nm light (Figure 1.86b), the broad transition at 670 nm was still observable for samples A-F, but the 505 nm transition was absent. Sharp transitions were also observable at 420 nm and 448 nm (weak for sample G). Interestingly, samples A-F show a transition at higher energy (lower wavelength) at 338 nm for samples A-F, while this transition was weaker and at slightly lower energy for sample G. The broad transition at 730 nm was still observable for samples F and G. Samples A and D also showed a very broad PL centered at ~450 nm.

If the samples were illuminated with 405 nm light (see Figure 1.86c), the 670 nm transition was still observable for samples A-F, and the 730 transition is observable for sample G. Two higher energy transitions were observable at 344 nm and 374 nm, while lower energy transitions were observable at 436, 466, and 496 nm. A broad PL at 500 nm was observed in samples A and D, but weak or absent in the other samples.

Clearly, sample E with the zinc to gallium ratio of $Zn_{1.1}Ga_2$ showed the largest PL response for all excitation wavelengths. Moreover, only the PL using the 313 nm excitation exhibited the broad 505 emission. Therefore, we used this excitation and 325 nm excitation from the HeCd laser to determine

the relative quantum efficiency of the Zinc gallate powder. As mentioned above, the amount of sample and the weakness of the observed PL using the HgXe illumination source precluded using the integrating sphere for quantum efficiency measurements. Therefore, a comparison was made with the trichromatic sample to get the relative quantum efficiency. These data are shown in Figure 1.87. The relative quantum efficiencies were 1.3% for 313 nm illumination and 1.1% for 325 nm illumination.

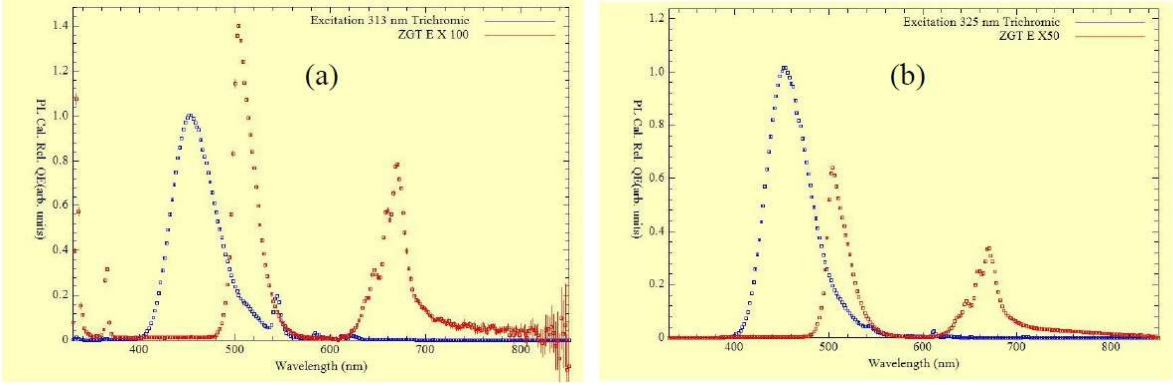

Figure 1.87. Comparison photoluminescence of the trichromatic phosphor and ZGT131120E ($Zn_{1.1}Ga_2$) using (a) 313 nm excitation from a HgXe lamp and (b) 325 nm excitation from the HeCd

Two primary broad transitions at 505 nm and 670 nm (probably due to Mn^{2+}) were observed in zinc gallate powder made by nanofermentation. The 505 nm transition was only observed when the sample was illuminated by 313 nm light, and the intensity of both transitions depended on the sample composition, with the largest photoluminescence occurring for sample E ($Zn_{1.1}Ga_2$). We also found that some samples showed a very broad photoluminescence at 450-500 nm, probably related to defects in the sample.

For these samples the maximum observed relative QE was 1.3% for 313 nm illumination and 1.1% for 325 nm illumination. Previous measurements of the relative QE versus excitation energy for ZGT:Cr^{3+} and AGT:Eu^{3+} showed that the peak excitation occurred for 288 nm illumination. As a result, it may be possible to get a slightly higher QE at lower wavelengths, but it is uncertain whether the increase would be significant.

The NF technique was developed to synthesize ZGT particles for optoelectronic applications. The wide bandgap of ZGT makes it attractive as host material for dopant induced optical emission control. We were successful in tuning the optical wavelength in the visible part of the spectrum (400-700 nm). However, the optical QE of the samples remained in the range of ~ 2% for all the samples indicating inefficient activation of dopants or nanoparticle defect structure dictating the net optical output. The observed low PLQE in ZGT nanoparticles indicates that the more detailed investigation of the particle size effects, surface characteristics, and defect structure is critical to understand the factors dictating the optical and electrical characteristics. A PLQE>20% is critical to define a path towards practical applications. The present QE results on ZGT nanoparticles indicate that we need to further evaluate the impact of novel NF process on the particle growth and properties. Binary nanoparticle materials offer a much simpler system than ZGT material to analyze the impact of NF process on the microstructural, optical, and electrical properties of the nanoparticles and thin film coatings.

2.3.5 Zinc Gallate Annealing and Characterization

Photoluminescence (PL) measurements were made from different samples of zinc gallate powder as discussed earlier. All the samples were annealed and the impact of nanofermentation process on the

zinc gallate particles quality was analyzed in terms of the photo-response characteristics. The results of structure-optical properties of Mn doped zinc gallates are summarized in Figure 1.88. As produced zinc gallates are mostly composed of 5-10 nm nanocrystals (Figure 188a,c), showing weak photoluminescence (Figure 188e) that we attribute to the host matrix of zinc gallate (weak bands at 450 nm and 520 nm for 350nm and 500 nm excitation respectively). Annealing at 1000^{o}C leads to the formation of facetted, large crystals which show strong luminescence from the dopant Mn^{2+} due to the ^{4}T-^{6}A 3d intrashell transition. [see: S.G. Kim et al., "Optical and Electrical Properties of $ZnGa_2O_4/Mn^{2+}$ Powder Electroluminescent Device," *Materials Letters*, **58**, 1354 (2004)].

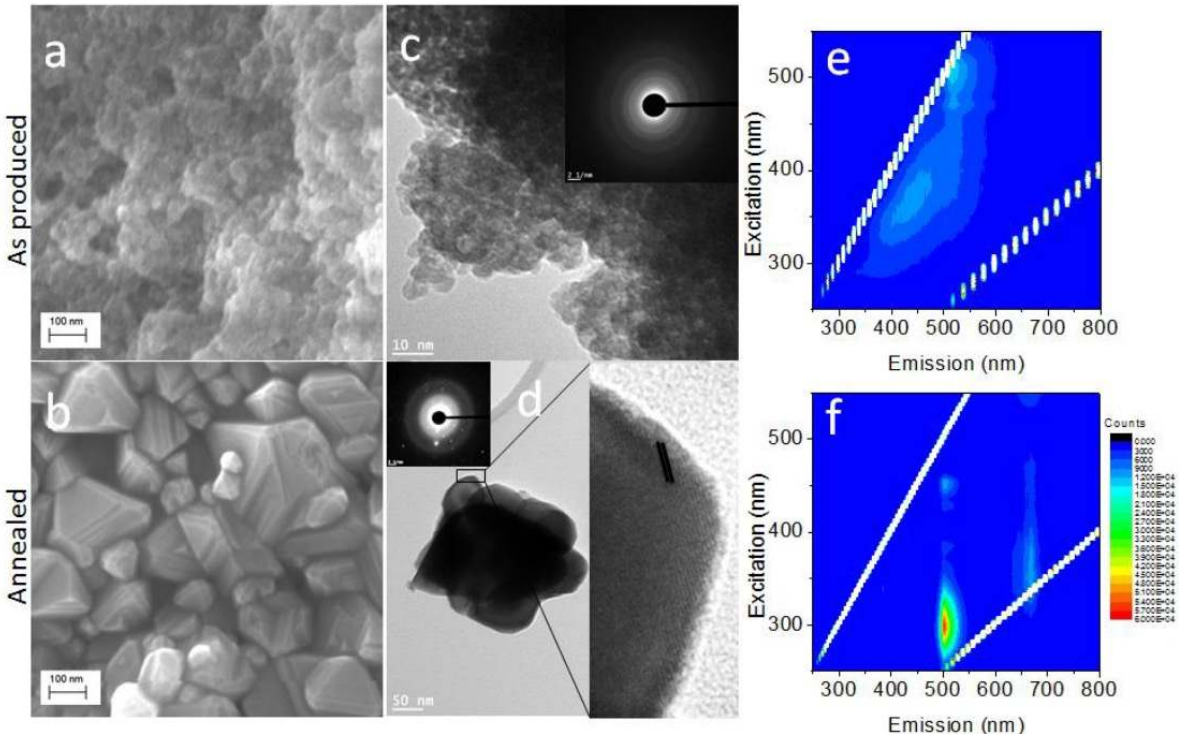

Figure 1.88. Scanning electron micrograph images of zinc gallate.

Scanning electron micrograph images of zinc gallate (a) as produced and (b) after annealing at 1000^{o}C. Transmission electron micrograph images of (c) as produced zinc gallate showing (5-10 nm) particles with clear signature of polycrystalline rings in the diffraction pattern (inset) and (d) annealing at 1000^{o}C leads to the formation of >20 nm crystals with low defects and some polycrystalline/high defect particles of much smaller size, inset of DP and right image showing (111) lattice fringe. Photoluminescence map of (e) as produced and (f) sample annealed at 1000^{o}C, the weak signature of ~400 and 520 nm are common features in both samples while the relative intensity of these peaks is higher for as produced zinc gallate. The annealing leads to the activation of the radiative route as evident by 503 nm emission (300 nm excitation), which is assigned to the ^{4}T-^{6}A 3d intrashell transition of Mn^{2+}.

2.4.7 Resistivity measurements of ZnO films

This is an important step for the scale up efforts required to produce achieve large amounts of high quality nanofermentation nanoparticles. There is great potential for using nanofermentation to produce nanofermentation nanoparticles for optoelectronics and sensor applications. In order to demonstrate this we have prepared and characterized several ZnO samples prepared by a PLD. Cross sectional SEM images of PLD-deposited ZnO films ion SiO2/Si substrates are shown in Figure 3. We

achieved the thickness of ZnO of about 300 nm and 100 nm for vacuum and 30 mTorr O_2 deposition conditions Figure 1.89 (a), (b). The in-plane impedance spectra of these films are shown in Figure 1.90). It indicates a transition from pure resistive behavior for frequency range <10kHz to capacitive one for higher frequencies for vacuum deposited ZnO film. Interestingly, the 30 mTorr ZnO film shows much higher impedance and low frequency resistance, and the transition to capacitive behavior occurs at much higher (>100kHz) frequency. Initially the samples we prepared using nanofermented ZnO NP were characterized by measuring the electrical impedance as a function of frequency. We found that the resistivity of the samples can be reduced to a few mOhm-cm therefore providing an excellent opportunity to develop low cost sensors using easily fabricated nanofermented thin film sensors.

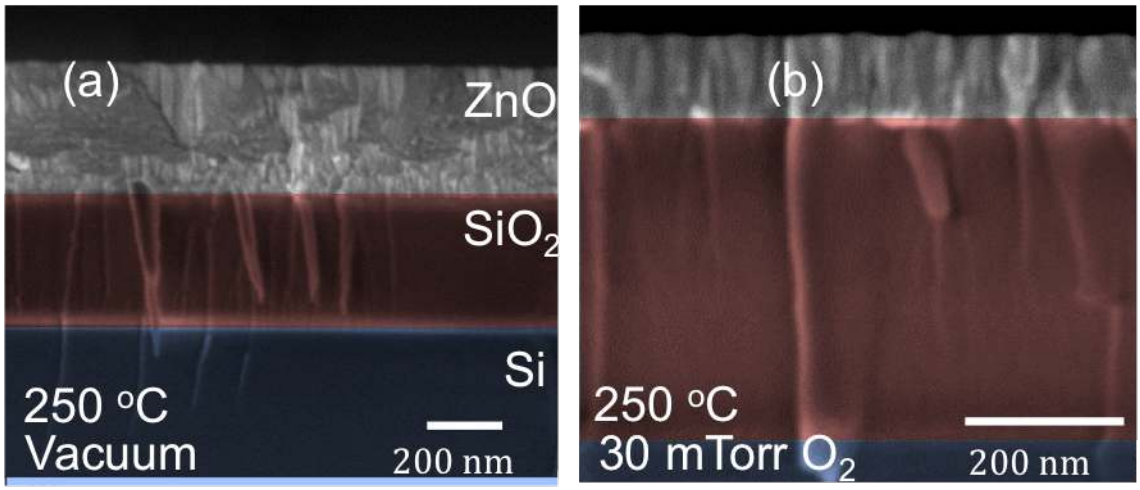

Figure 1.89. Cross sectional SEM images of PLD-deposited ZnO films ion SiO_2/Si substrates.

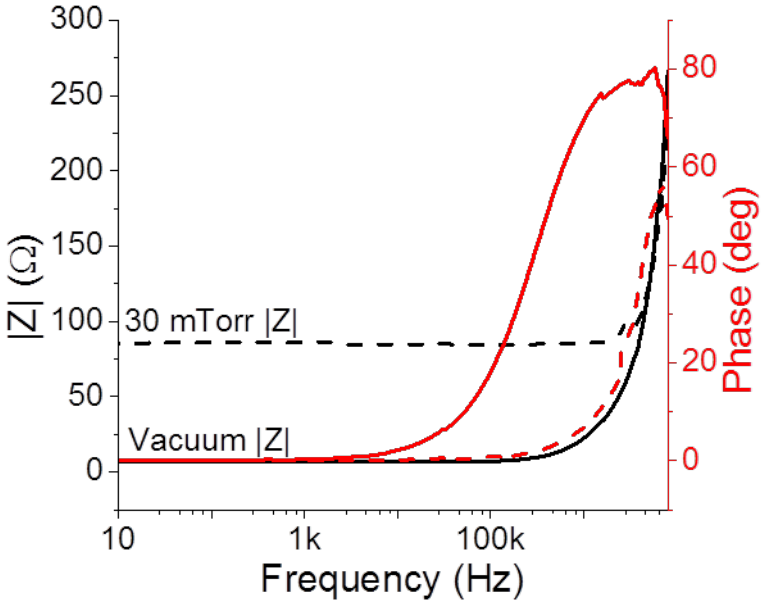

Figure 1.90. In-plane impedance spectra of PLD-deposited ZnO films ion SiO_2/Si substrates as a function of frequency.

The different parameters are summarized in Table 1.18 for the PLD-deposited ZnO films including the thickness, impedance, resistivity and mobility of the ZnO thin film prepared using pulse laser

deposition. The nanofermented ZnO is referred to the film prepared from nanofermented nanoparticles. The samples labeled ZnO and Al-ZnO were commercial samples of pure ZnO and ZnO doped with 1% Al. The lowest resistivity was achieved with intrinsically doped NF NP ZnO (S1) and 1% Al:ZnO. The resistivity was calculated from the value of the low frequency impedance, thickness of the film and the distance between the electrodes. The value of the resistivity of NFNP film suggests that it can be used for sensing application as well as transparent conducting substrate in PV and LED applications.

Table 1.18 Electrical performance of NF ZnO films prepared using pulse laser deposition

Sample	Temp °C	O_2 Torr	Electrode Dimensions			Impedance Ω	Resistivity Ω·cm	Mobility cm^2/Vs
			Gap µm	Width mm	Thickness nm			
NF-ZnO S1	250	~ 10^{-5}	25	2	315	6.7	16.8 x 10^{-3}	1.04
NF-ZnO S2	250	30 x 10^{-3}	25	2	88	87	61.2 x 10^{-3}	1.3
Al-ZnO S1	250	~ 10^{-5}	50	2	220	3.3	5.8 x 10^{-3}	.003
Al-ZnO S4	250	30 x 10^{-3}	25	2	362	4.3	12.5 x 10^{-3}	.009
ZnO	400C	0.5	25	2	300	11.2 x 10^{6}	26.7 x 10^{4}	

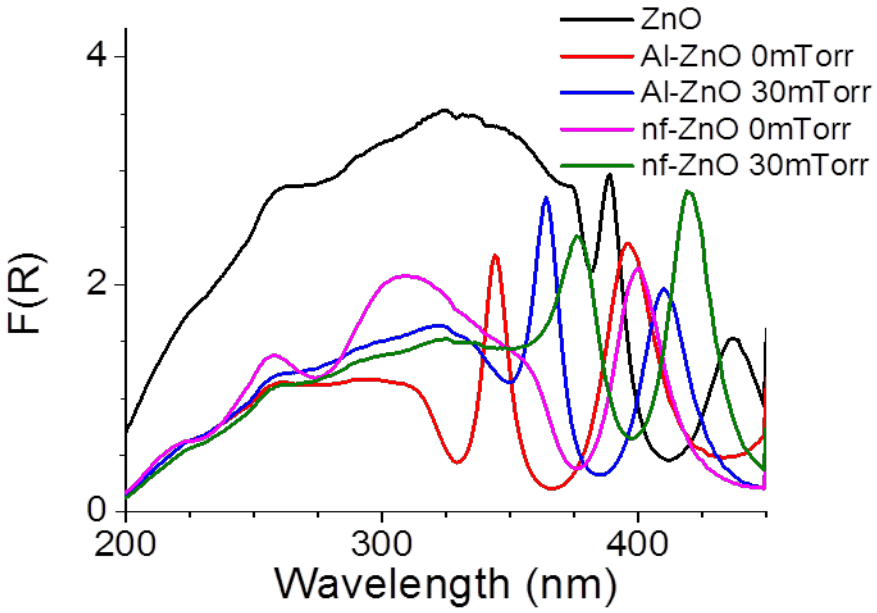

Figure 1.91. UV-Vis diffuse reflectance as a function of wavelength for PLD ZnO films, the reference and nanofermented deposited on Si/SiO_2 substrate.

Figure 1.91 shows the measured optical properties of PLD ZnO films, and the reference and nanofermented films deposited on Si/SiO_2. The films were measured in a diffuse reflectance configuration. While precise calculation of the optical band gap was obscured by the interference fringes, the estimated the band gap was obtained from the edge of unobscured absorbance. We found that Al and NF ZnO films show upshift in the energy of the band gap, which was also confirmed by

the band gap energies reported by others, e.g. (ZnO)=3.31, e.g.(Al:ZnO)=3.4eV (see Table 1.19).

Table 1.19 Thin-film Energy Band Gaps

System	Bandgap Energy (eV)
ZnO	3.31
Al-ZnO	~ 3.40
S-doped ZnO	~ 3.1
ZnS	3.74 eV

3.0 TASK 2: DRYING AND SINTERING OF SILVER INKS

The main focus of this task was the evaluation of aqueous and solvent based conductive inks developed by NovaCentrix for electronic device applications. The goal was to deposit silver inks on plastic substrates by roll-to-roll compatible inkjet printing and screen-printing techniques. A goal was to use the PulseForge tool to combine the drying and sintering processes into a single pass for high throughput commercial applications – potentially reducing processing time by 2-3 orders of magnitude. The printed metal coating quality and electrical performance was to be evaluated for roll-to-roll printed electronic applications.

3.1 CONDUCTIVE METAL INKS

The main goal is to identify a rapid, single-pass route to drying and sintering of printed silver inks on flexible plastic substrates using the NovaCentrix PF 3300 pulse thermal processing system. High speed, low cost printing and processing of metal-based inks on low temperature flexible substrates is essential for the advancement of innovative new products in photovoltaics, displays, RFID, sensors, batteries, capacitors, and smart packaging. Because the factors that influence drying and sintering of printed inks place limits on the speed and cost of ink processing and production, a solid understanding of these factors is required. At the same time, ORNL's unique pulse thermal processing technology was exploited to minimize the thermal budget for ink curing, which is a major limitation of the current furnace based annealing approach. Initially, we focused on the curing of silver inks. The main steps in our development and evaluation of conductive metal inks for flexible electronics are highlighted in Figure 2.1.

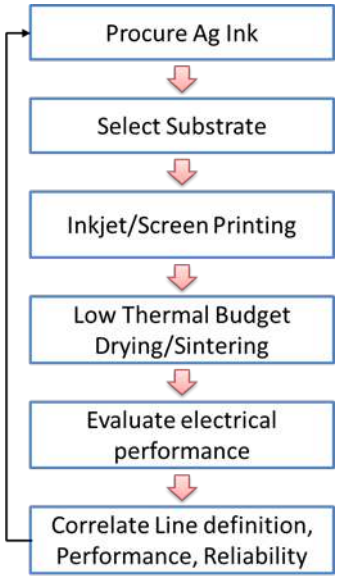

Figure 2.1. General steps in the development and evaluation of the conductive metal inks for flexible electronic applications.

The task encompasses the following focus areas:

- A focus on the evaluation of aqueous and solvent based commercial inks.
- Substrates included porous and non-porous flexible plastics with roll-to-roll potential.
- Printing techniques included inkjet printing and screen printing.
- Sintering techniques included furnace and pulsed thermal processing.

The initial activities in this task related to the photonic curing of the Ag inks, and were as follows:

- Ink formulations and an experimental matrix were finalized in discussions with NovaCentrix,
- Pulse thermal processing conditions for initial investigation of the simultaneous drying and sintering were identified.
- Substrate materials (125µm sheet thickness) were identified and acquired.
- Non-porous substrates included PET, ABS, Polycarbonate (PC), Ultem and Kapton.
- Porous substrates used in this study were Novele™ IJ-220 coated PET.
-

Printable commercial silver inks were identified and acquired.

- Water-based Ag ink: Novacentrix JS-B25HV
- Alcohol-based Ag Ink: Cabot CCI-300
- Equipment to measure the electrical conductance of printed lines were assembled.

Initial efforts to print and furnace process water-based Novacentrix ink were conducted. The results suggest that:

- Substantial drying (~10-30%) of the printed lines occurred within minutes of printing. This observation impacted the choice of conditions for subsequent pulsed thermal processing. Coupling the Dimatix printer with the Pulse Forge would be desirable but is presently impractical.
- Lines printed on porous flexible substrates (Novele™ and paper) are conductive when furnace processed at ~120-160°C.

Lines printed on non-porous flexible substrates are not conductive when furnace processed at <~200°C. This may require ink reformulation.

- Lines are conductive when printed on glass or alumina and processed at ~450°C.

3.1.1 Inks on flexible substrates

Commercial silver conductive inks, both aqueous-based and alcohol-based, were acquired. These inks were successfully printed on several flexible substrates including porous coated PET and non-porous polycarbonate, Ultem, and ABS. Initial attempts to understand the printing, drying and sintering of these inks revealed significant differences in performance. Figure 2.2 shows typical drying results for the alcohol-based silver ink printed on an Ultem substrate. The resistance for similarly printed and furnace dried water-based ink is nearly infinite (non-conductive) for all drying times and temperatures.

The original milestones defined for this project were to achieve a sheet resistance of < 5mΩ/Sq. However, after further consultation with our industry sponsor, NovaCentrix, it was determined that the original milestone was not sufficiently specific. Sheet resistance alone is not sufficient to define the performance of a thin film electrical circuit because the thickness of the printed line is not specified. In order to more accurately define the conductivity of a printed circuit, the industry standard measurements must include both sheet resistance and resistivity, which is typically defined in terms of multiplier of bulk silver. Therefore, the following milestones were proposed and approved for Task 2 during a DOE program review at ORNL on September 11, 2012.

- MS 2.1.2 (6/30/12) Define benchmark oven cure performance for ink-jet printing (Rs < 160mΩ/Sq, ~3x bulk Ag) and begin PTP study for ink-jet printed inks
- MS 2.1.3 (9/30/12) Achieve Rs < 210mΩ/Sq, ~4x bulk Ag* for ink jet printed materials processed by PTP, initiate study on screen printed materials
- MS 2.1.4 (12/31/12) Achieve Rs < 2.5mΩ/Sq, ~3x bulk Ag* for screen printed materials processed by PTP

- MS 2.2 (12/31/13) Demonstrate PTP processed ink jet printed metal lines with Rs < 180 mΩ/Sq, ~4x bulk Ag
- MS 2.3 (12/31/14) Demonstrate PTP processed ink jet printed metal lines with Rs < 100 mΩ/Sq, ~1.5x bulk Ag

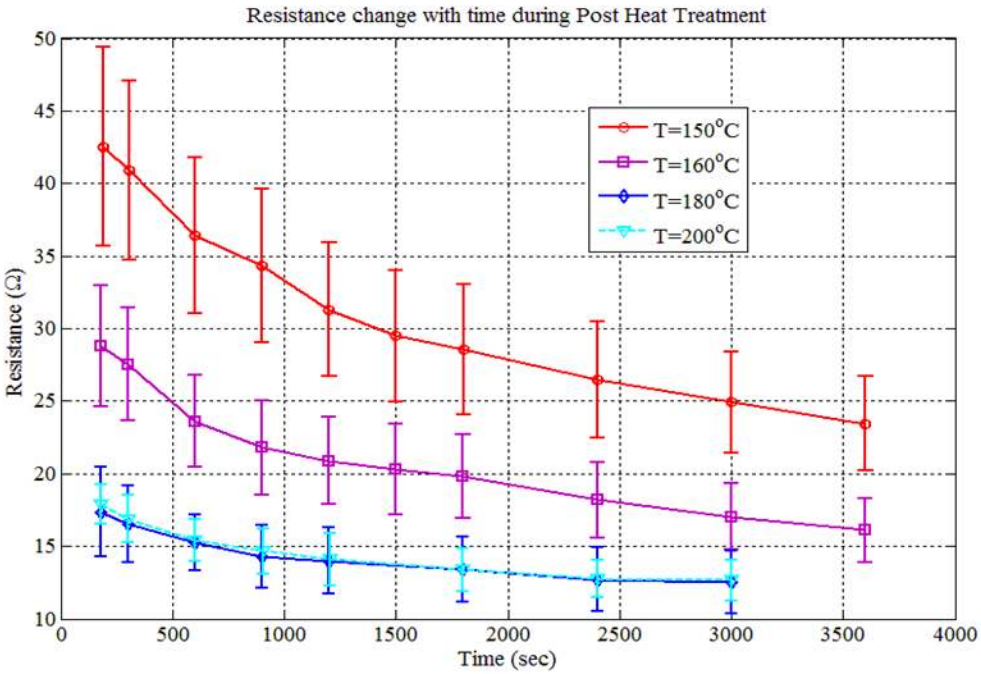

Figure 2.2. Drying results for alcohol-based silver ink on Ultem substrate.

3.1.2 Sintering and electrical performance of ink jet printed materials

Evaluation of silver conductive inks subsequently focused on the sintering and electrical performance of ink jet printed materials. Two commercial inks, one water-based and the other alcohol-based, were each inkjet printed on two flexible substrates, one porous (Novele® coated PET) and the other non-porous (Kapton® polyimide).

To establish a baseline for sintering, printed samples for the four combinations of ink and substrate were first furnace sintered in air for various times at a temperature that is compatible with the substrate (150°C for PET and 300°C for polyimide). The resulting resistivity ($\boldsymbol{\rho}$), sheet resistance (R_s), and minimum furnace sinter time are shown for the four combinations in Table 2.1. Electrical performance was observed to be good, especially for the non-porous Kapton® substrate, but the minimum furnace sintering times are long (5-100 minutes).

Table 2.1. Results for furnace sintering of inkjet printed silver ink.

Substrate	Ink	Thickness (µm)	Furnace $\rho/\rho_{Ag\ bulk}$	Furnace R_s (mΩ/□)	Furnace Sinter Time
Novele® (porous)	Cabot (alcohol)	1.27	4.1	51	5 min
Novele® (porous)	Novacentrix (water)	1.99	5.2	42	10 min
Kapton® (non-porous)	Cabot (alcohol)	1.27	1.8	22	40 min
Kapton® (non-porous)	Novacentrix (water)	1.99	1.8	14	100 min

The electrical performance for PTP sintered samples was generally good except for the alcohol-based Cabot silver ink on Kapton® where ink detachment from the substrate was observed (Table 2.2). The times for PTP sintering (5 - 20 seconds) were, however, substantially shorter than those for furnace sintering (5 - 100 minutes). Short sintering times are clearly desirable for high-rate, low-cost manufacturing processing and were demonstrated here using PTP methods.

Companion samples were sintered in air using a PulseForge 3300 pulsed thermal processing (PTP) tool. Best PTP results for the four sample combinations are shown in Table 2.2.

Table 2.2. Results for PTP sintering of inkjet printed silver ink

Substrate	Ink	Thickness (µm)	PTP $\rho/\rho_{Ag\ bulk}$	PTP R_s (mΩ/□)	PTP Sinter Time
Novele® (porous)	Cabot (alcohol)	1.27	1.35	17	20 sec
Novele® (porous)	Novacentrix (water)	1.99	3.5	25	10 sec
Kapton® (non-porous)	Cabot (alcohol)	1.27	detached	detached	detached
Kapton® (non-porous)	Novacentrix (water)	1.99	6.0	50	5 sec

In the continuing evaluation of silver conductive inks, studies were conducted on screen-printing, furnace and PTP sintering, and the electrical performance of thick silver lines. A commercial, small flake (D50 = 0.4µm, D90 = 0.8µm), Novacentrix ink was screen-printed using multiple coatings on two flexible substrates, one porous (ArjoWiggins coated paper) and the other non-porous (Kapton® polyimide). Figure 2.3 shows examples of printing for each substrate, and Figure 2.4 show profilometry results after thermal processing. Multiple coatings lead to thicker but generally rougher lines.

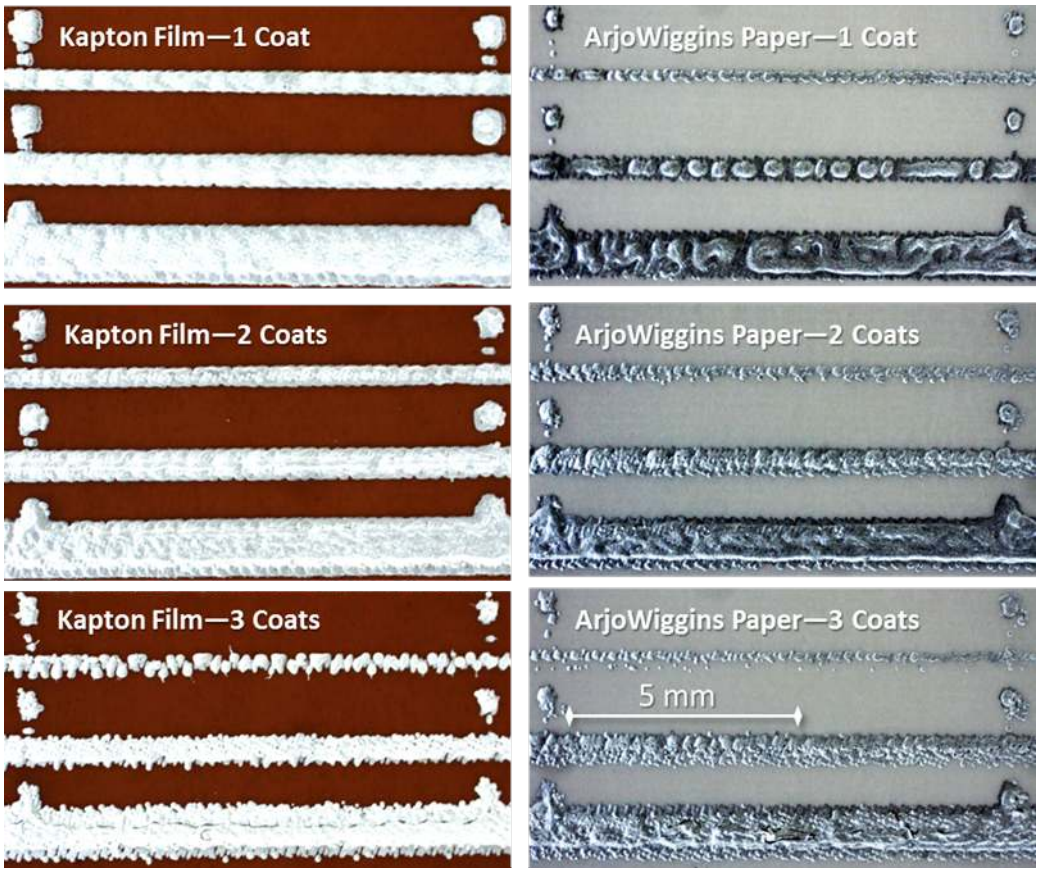

Figure 2.3. Optical micrographs showing typical multi-coat print quality for each substrate.

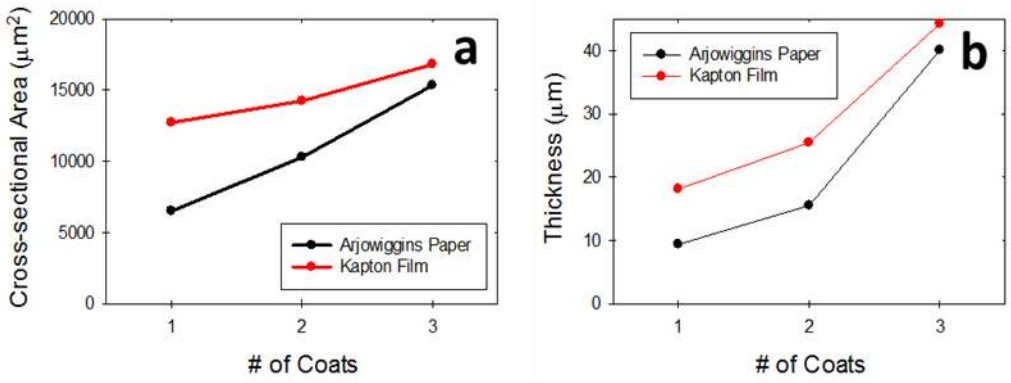

Figure 2.4. Stylus profilometer results showing a) cross-sectional area and b) thickness of sintered multi-coat silver lines.

Sintering was initially conducted in air using a PulseForge 3300 pulsed thermal processing (PTP) tool. The best PTP results for the six sample combinations are shown in Table 2.3. Electrical performance after the 8.6 minute PTP processing was generally good, especially for the 2-coat silver on the non-porous Kapton® substrate.

Table 2.3. Results for PTP and furnace sintering of multi-coat screen printed silver ink.

Substrate	# of Coats	Thickness (µm)	Resistivity $\rho/\rho_{Ag\ bulk}$	Sheet Resistance R_s (mΩ/□)	Sinter Time (min)
ArjoWiggins (porous)	1	9.3	3.1 (3.0)†	5.3 (5.1)†	8.6 (249)†
ArjoWiggins (porous)	2	15.5	3.6 (3.1)†	3.7 (3.2)†	8.6 (249)†
ArjoWiggins (porous)	3	40.0	5.3 (4.3)†	2.1 (1.7)†	8.6 (249)†
Kapton® (non-porous)	1	18.1	4.3 (3.8)†	3.8 (3.3)†	8.6 (249)†
Kapton® (non-porous)	2	25.4	2.8 (2.1)†	1.7 (1.3)†	8.6 (249)†
Kapton® (non-porous)	3	44.2	5.1 (4.0)†	1.8 (1.4)†	8.6 (249)†

† - PTP followed by 240 min. 200°C furnace anneal in air.

Following PTP processing, each sample was further furnace sintered in air at 200°C for 240 min. For all samples, this additional 240 min furnace treatment improved the electrical performance (see Table 2.4 in parentheses).

The results shown in Table 2.3 demonstrated the capabilities of PTP and screen printing to achieve a sheet resistance of 1.7 mΩ/sq and a resistivity of 2.8x bulk silver for a 25 µm thick silver film on Kapton®. The total PTP sintering time in this case was only 8.6 minutes. Additional furnace annealing in air at 200°C for 240 minutes led to further improvements in both sheet resistance and resistivity of nearly 25%.

In further studies, two commercial Novacentrix inks, one large flake (D50 = 2µm; D90 = 4µm) and the other small flake (D50 = 0.4µm, D90 = 0.8µm), were each screen printed on two flexible substrates, one porous (ArjoWiggins coated paper) and the other non-porous (Kapton® polyimide). Inks were printed using an AMI screen printer and a steel wire (0.0011" diameter) screen with a 230/inch mesh count and a 0.0014" emulsion thickness. Lines of ink were printed in widths ranging from 25µm to1 mm. Figure 2.5 shows examples of printing for each ink/substrate combination.

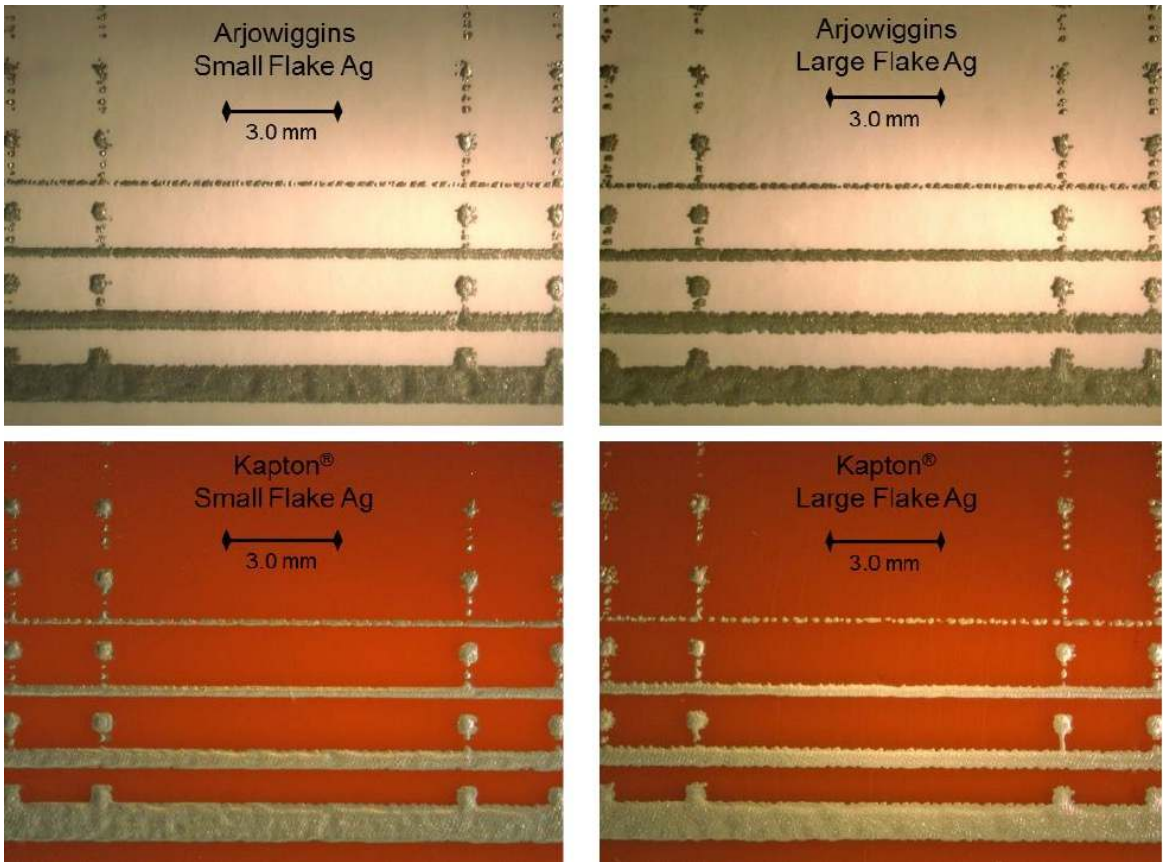

Figure 2.5. Optical micrographs showing typical print quality for each ink/substrate combination.

To establish a baseline for sintering, screen printed samples for the four combinations of ink and substrate were first furnace sintered in air for various times at a temperature that is compatible with both substrates (200°C). The resulting resistivity ($\boldsymbol{\rho}$), sheet resistance (Rs), and minimum furnace sinter time are shown for the four combinations in Table 2.4. Electrical performance was found to be good, especially for the non-porous Kapton® substrate, but the furnace sintering times were long (240 minutes).

Table 2.4. Results for furnace sintering of screen printed silver ink.

Substrate	Ink	Thickness (µm)	Furnace $\boldsymbol{\rho}/\boldsymbol{\rho}_{\text{Ag bulk}}$	Furnace R_s (mΩ/□)	Furnace Sinter Time
ArjoWiggins (porous)	Large Flake Silver	15.8	5.3	5.3	240 min
ArjoWiggins (porous)	Small Flake Silver	18.7	3.8	3.3	240 min
Kapton® (non-porous)	Large Flake Silver	18.0	4.0	3.5	240 min
Kapton® (non-porous)	Small Flake Silver	13.1	3.0	3.6	240 min

Companion samples were then sintered in air using a PulseForge 3300 pulsed thermal processing

(PTP) tool. Best PTP results for the four sample combinations are shown in Table 2.5.

Table 2.5. Results for PTP sintering of screen printed silver ink

Substrate	Ink	Thickness (µm)	Furnace $\rho/\rho_{Ag\ bulk}$	PTP R_s (mΩ/□)	PTP Sinter Time
ArjoWiggins (porous)	Large Flake Silver	15.8	8.2 (3.1†)	8.2 (3.1†)	8.6 min (249 min†)
ArjoWiggins (porous)	Small Flake Silver	18.7	13.7	11.7	8.6 min
Kapton® (non-porous)	Large Flake Silver	18.0	5.6 (3.6†)	4.9 (3.1†)	8.6 min (249 min†)
Kapton® (non-porous)	Small Flake Silver	13.1	3.1	3.7	8.6 min

† - PTP sintered followed by 240 min, 200°C furnace anneal.

The electrical performance for PTP sintered samples was also good except for the large flake silver ink on ArjoWiggins paper. This performance could likely have been improved with a subsequent 240 min, 200°C furnace anneal. Although the electrical performance of the PTP-only sintered samples are generally not as good as that for their furnace sintered companions, the times for PTP-only sintering (8.6 minutes) are substantially shorter than those for furnace sintering (240 minutes). The milestone selected as the goal for PTP samples was to achieve a sheet resistance < 2.5mΩ/Sq at approximately 3x bulk Ag for screen printed materials. Although we were able to achieve a high quality for the printed material (3x bulk Ag conductivity), the goal of < 2.5 mΩ/Sq was not met during these studies. The thickness of the screen printed lines could be increased significantly in order to meet this metric by adjusting various print parameters.

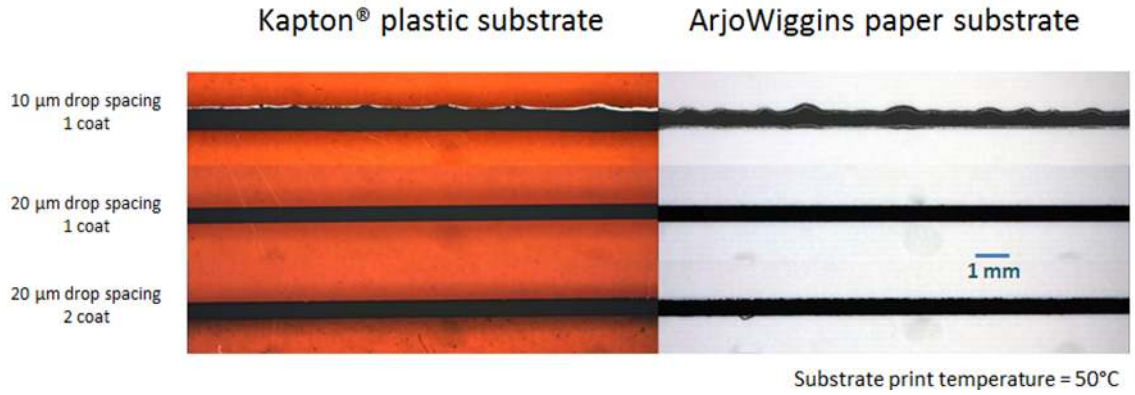

Figure 2.6. Optical micrographs showing typical print quality for each substrate.

To demonstrate the reduced resistance of increased line thickness, a commercial solvent based silver ink (Cabot) was printed using single and multiple coatings on two flexible substrates, one paper-based (ArjoWiggins coated paper) and the other polymer-based (Kapton® polyimide). Figure 2.6 shows examples of printing for each substrate. After printing, the substrates were furnace sintered at 200°C for 240 minutes. Figure 2.7 shows the results for the printed lines after printing and furnace sintering. In all cases the electrical resistance of the silver line printed on the paper-based substrate was less than the corresponding line on the polymer-based substrate.

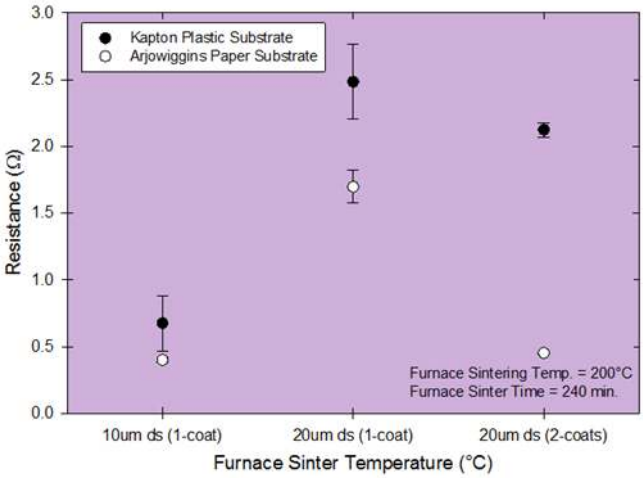

Figure 2.7. Electrical resistance for paper- and polymer-based substrates.

Table 2.6 shows a summary of the electrical results.

Table 2.6. Results for inkjet printing and furnace sintering on paper and polymer substrates

Sample	R (Ω)	A (cm^2)	ρ (μΩ· cm)	ρ/ρ_{Ag}	t (μm)	R_S (mΩ/sq)
Kapton 10 μm ds 1-c #3	0.6757	1.371 x 10-5	9.26	5.82	1.55	59.7
Kapton 20 μm ds 1-c #5	2.4840	4.18 x 10-6	10.4	6.54	0.735	141.5
Kapton 20 μm ds 2-c #7	2.1240	5.34 x 10-6	11.5	7.23	0.818	140.5
Arjo 10 μm ds 1-c #4	0.4000	1.371 x 10-5	5.48	3.45	1.55	35.4
Arjo 20 μm ds 1-c #6	1.6980	4.18 x 10-6	7.10	4.47	0.735	96.6
Arjo 20 μm ds 2-c #8	0.4522	5.34 x 10-6	2.41	1.52	0.818	29.5

The next task in demonstrating printable metal inks was to develop a printable insulating coating. The chosen ink was a Sun Chemical polymer-based ink, which required UV light for both setting and curing. UV setting must occur within seconds of printing to prevent the ink from spreading on the substrate. This was accomplished with the light guide of a UV source attached to the inkjet print head. The light guide was offset a distance from the ink nozzles to avoid UV exposure of the ink at the nozzles.

Figure 2.8 shows an example of a test print pattern for UV setting of ink. The two 5 x 5 arrays of squares are offset a distance equal to the distance between the UV light guide and the print nozzles. As the print head travels for left to right, first a portion of the left array is printed and then a portion of the right array is printed. While the right array is printed, the UV light guide passes over the left array. If the UV intensity and print speed are correct, the final result is a UV-set left array and an unset right array.

Figure 2.8. Two 5 x 5 arrays of printed squares.

The UV setting polymer was successfully printed and cured on both non-porous glass and flexible PET substrates. Controlling the intensity of the UV exposure varied the smoothness of the top surface of the cured polymer. Figure 2.9 shows the surface profile of six lines of polymer that were cured using different UV intensities. The surface smoothness increases monotonically with decreasing UV intensity.

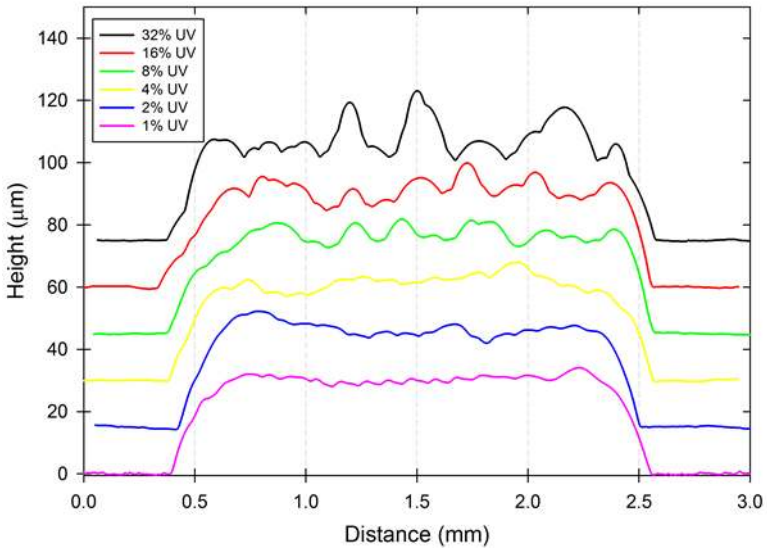

Figure 2.9. Surface profile of six lines cured using different UV light intensities.

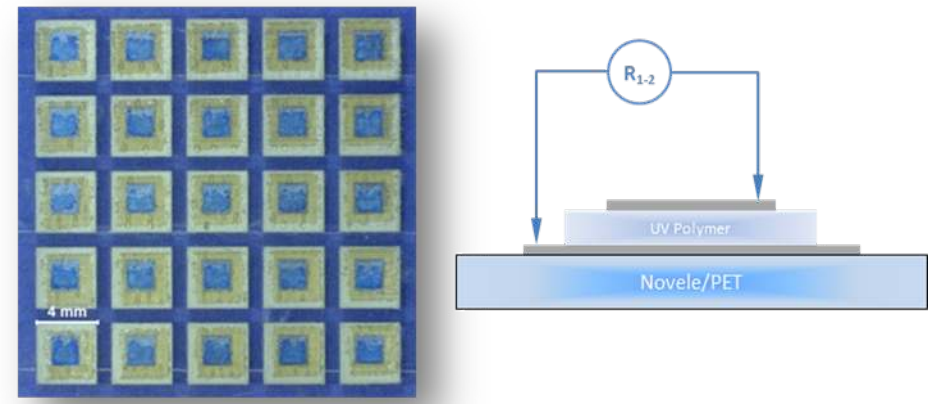

Figure 2.10. Example of a 5 x 5 array of 3-layer printed stacks.

A layer of UV polymer was printed between two layers of printed silver on a PET substrate to form a 3-layer printed stack (see Figure 2.10). A total of fifty such stacks were fabricated and electrically

tested. Low resistance for some of the stacks was attributable to pinholes in the polymer layer or printer misalignment.

The structures discussed above consisted of alternating layers of printed silver and printed UV setting polymer. The UV setting intensity for these structures was chosen to be 32%, and more than half of the printed structures exhibited low resistance (i.e., poor performance) that was attributed to either pinholes in the printed polymer or printer misalignment. To address the problem of pinholes, the intensity of the UV exposure was reduced from the 32% to 1% to allow the polymer ink more time to flow prior to being "set". Figure 2.11 shows a substantially smoother surface for the polymer cured at 2% than at 32%. Twenty-five additional multi-layer structures were printed using 2% UV intensity. Only 20% of these structures showed low resistance. This result suggests that control of the UV setting intensity reduces pinholes in the polymer and improves the performance of the multilayer structure.

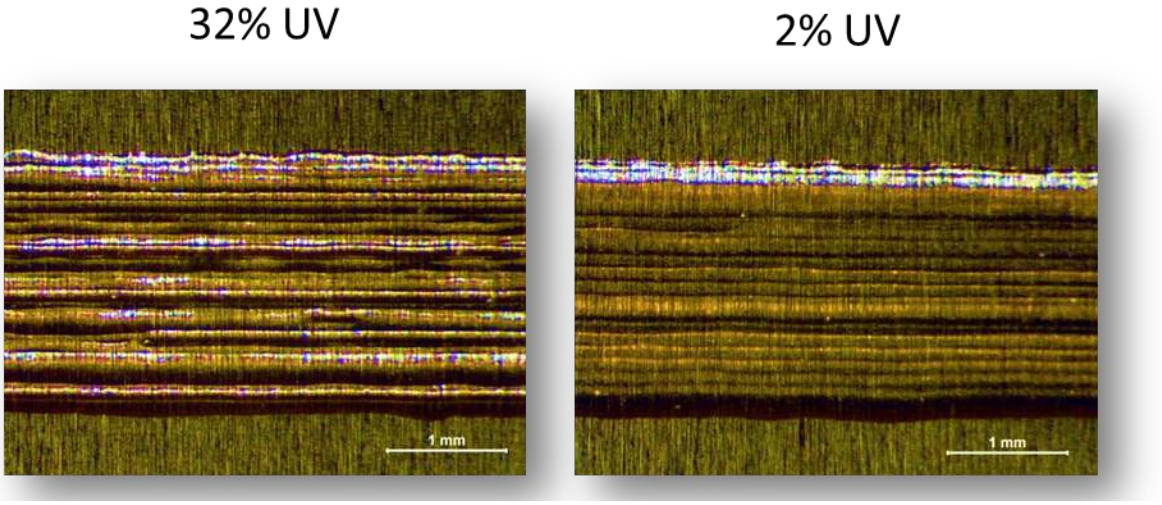

Figure 2.11. Images of a silver strain gauge printed directly on the FDM photopolymer substrate. The polymer was printed using UV intensities 32% and 2%.

A simple resistive strain gauge was designed for inkjet printing on Fused Deposition Modeling (FDM) substrates. A Stratasys Objet 30 Pro 3D printer was chosen to prepare the ~25 x 25 mm FDM substrates using a black rigid UV-curable photopolymer (VeroBlack Plus™). The Objet printing process includes a surface rolling/pressing step that tends to improve interlayer bonding, surface density, and surface smoothness. The smoother denser surface of the Objet substrate reduces some of the challenges associated with printing of conductors on FDM surfaces.

Figure 2.12 is an image of a typical silver strain gauge printed directly on the FDM photopolymer substrate. The higher magnification inset (upper right) shows the quality and fine features achievable for the ~250 µm wide printed silver lines. When printed directly on the photopolymer substrate, the strain gauge exhibited a resistance as low as ~50 Ω. To successfully demonstrate an embedded printed strain gauge within an FDM structure, the printed strain gauge (above) needs to be overlaid with FDM material and tested. Testing would include circuit resistance, gauge factor, and tensile strength of the FDM structure.

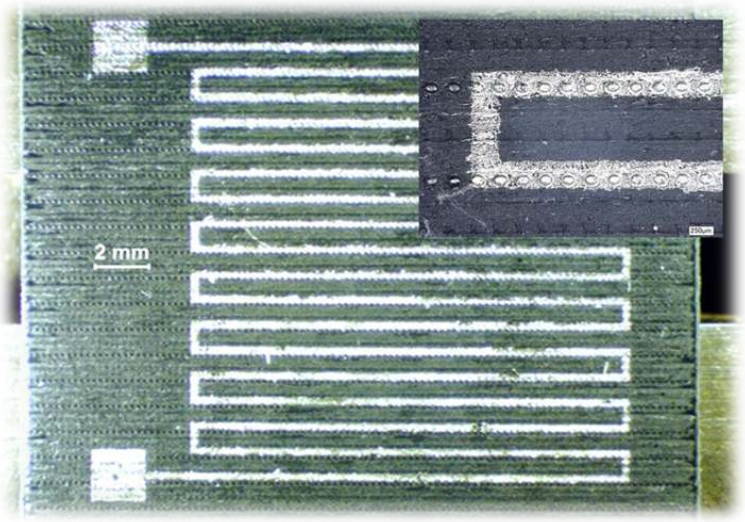

Figure 2.12. Silver resistive strain gauge printed on an FDM substrate. Inset shows higher magnification of the printed line.

The continuing work on this task next focused on curing the inkjet silver nanoparticles using photon pulses. The inks were from different sources (NovaCentrix and Cabot). Two different print thicknesses were used (i.e. 1.99 μm and 1.27 μm) on two different substrates. The sintering time was varied from 5s to 10s to 20s. In Table 2.7 we summarize the details for the curing process and the measured resistance. For the polyimide substrate, we observed in one case detachment of the ink layer. In Figure 2.13 we plotted the measured resistance for the four samples described in Table 2.6 as a function of sintering time. In Figure 2.14 we show the effect of the pulse frequency on the measured resistance as a function of sintering time for the four samples described in Table 2.6.

Table 2.7. Pulsed photonic curing of inkjet silver nanoparticles

Substrate	Ink	Thickness (μm)	Furnace ρ/ρ_{bulk}	Furnace R_s (mΩ/sq)	Furnace Sinter Time	PPC ρ/ρ_{bulk}	PPC R_s (mΩ/sq)	PPC Sinter Time
Oxide coated PET	Novacentrix	1.99	5.2	42	10 min	3.5	25	10 sec
Oxide coated PET	Cabot	1.27	4.1	51	5 min	1.35	17	20 sec
Polyimide	Novacentrix	1.99	1.8	14	100 min	6.0	50	5 sec
Polyimide	Cabot	1.27	1.8	22	40 min	detached	detached	detached

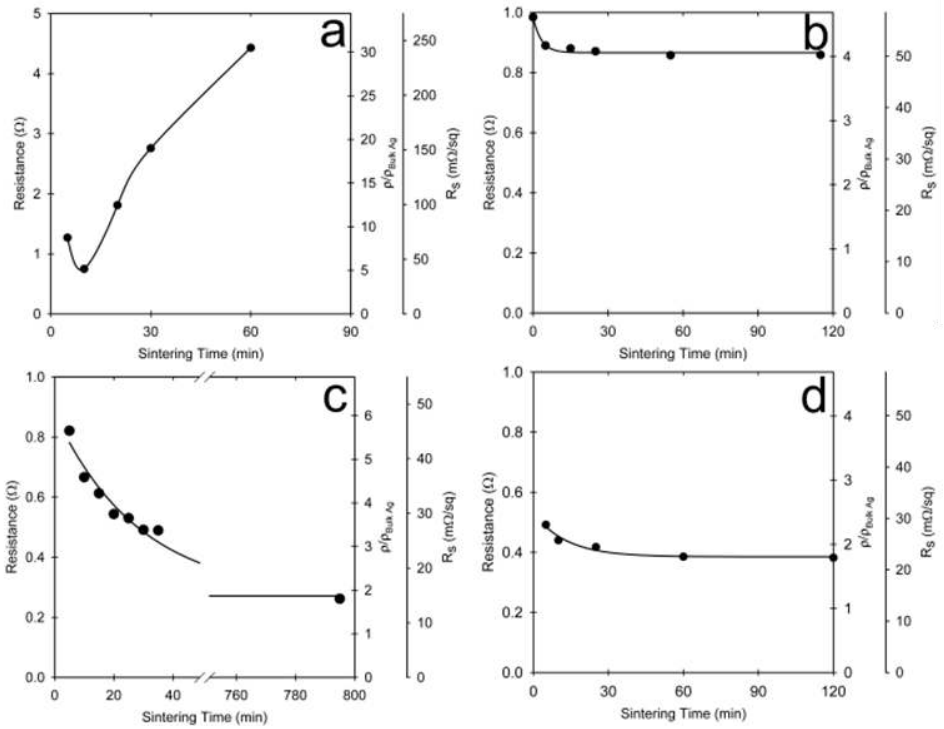

Figure 2.13. Resistance as a function of sintering time for the cured inks.

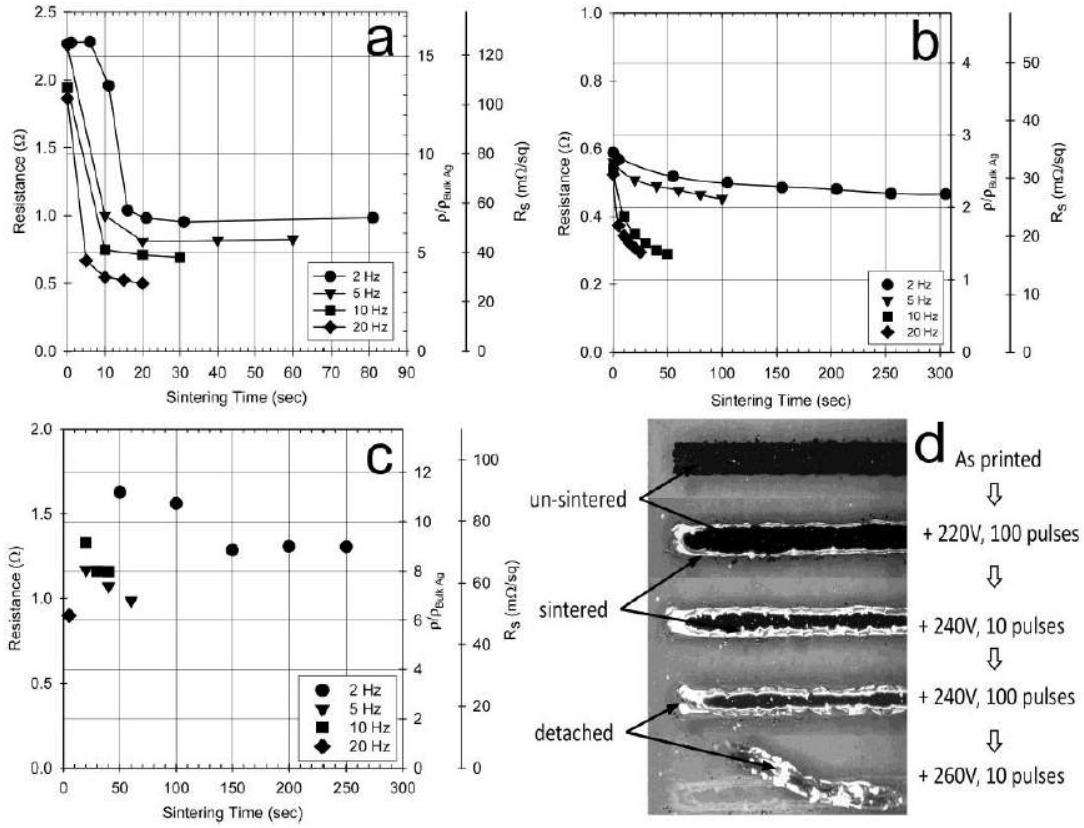

Figure 2.14. Resistance as a function of sintering time and pulse frequency rate for the cured inks.

In further studies we used inks to silver print FDM substrates with 1-mm thick FDM material. The FDM frame and printed substrate were used to fabricate an embedded strain gauge, and to successfully embed a printed strain gauge within a FDM structure using a frame that was fixed to the print bed of the Stratasys Objet 30 Pro 3D printer. Figure 2.15 shows a photograph of a prototype embedded strain gauge with the inkjet printed silver conducting line embedded between two 1-mm thick FDM layers.

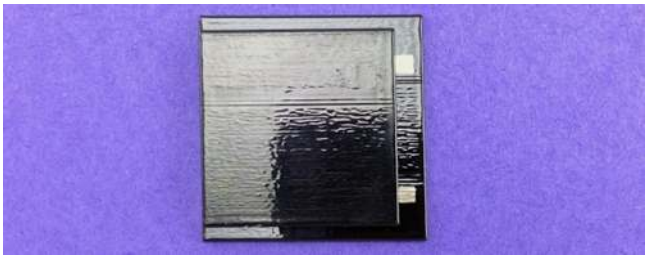

Figure 2.15. A prototype embedded strain gauge. Inkjet printed silver between two 1-mm thick FDM layers.

The process of embedding circuitry in the printed structure involved three distinct steps. In the first step, a Dimatix printer was used to print the conductive traces on the substrate. The second step involved embedding the traces while printing sockets for components using the Stratasys Objet 30 Pro 3D printer. In the third and final step, the components were inserted and overprinted using the Stratasys Objet 30 Pro 3D printer. Figure 2.16 shows schematically the three-step process.

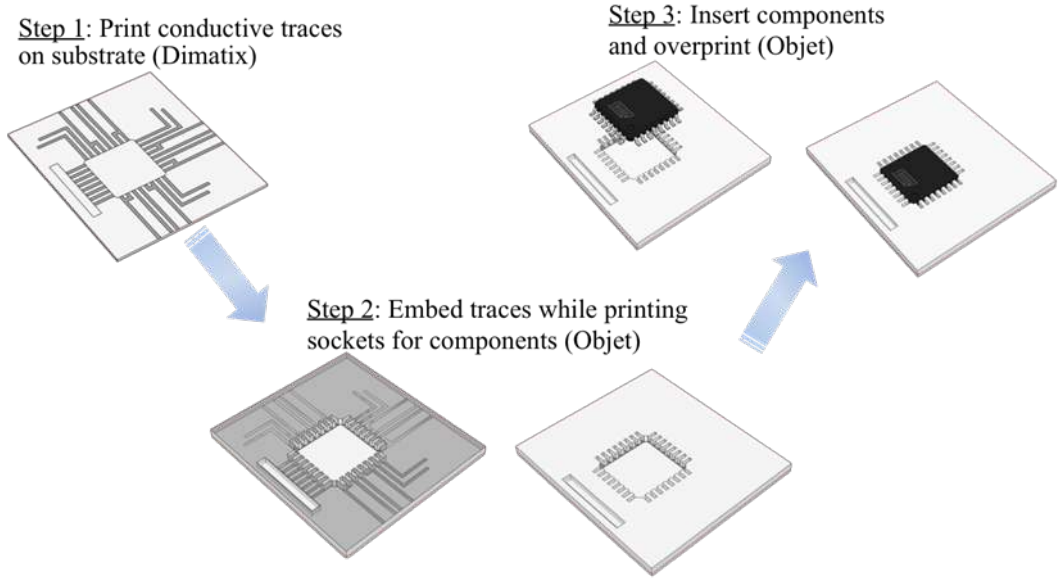

Figure 2.16. The three step process used to embed circuitry in printed structures.

One of the significant efforts in this project was to embed complex circuit geometries that would provide additional functionality at a reduced cost (see Figure 2.17). For example, implementing Arduino complex logic circuitry and incorporating a surface-mount microchip with various surface mount components such as LEDs, capacitors, resistors, memory and display would provide unprecedented functionality and control using roll-to-roll printable electronics.

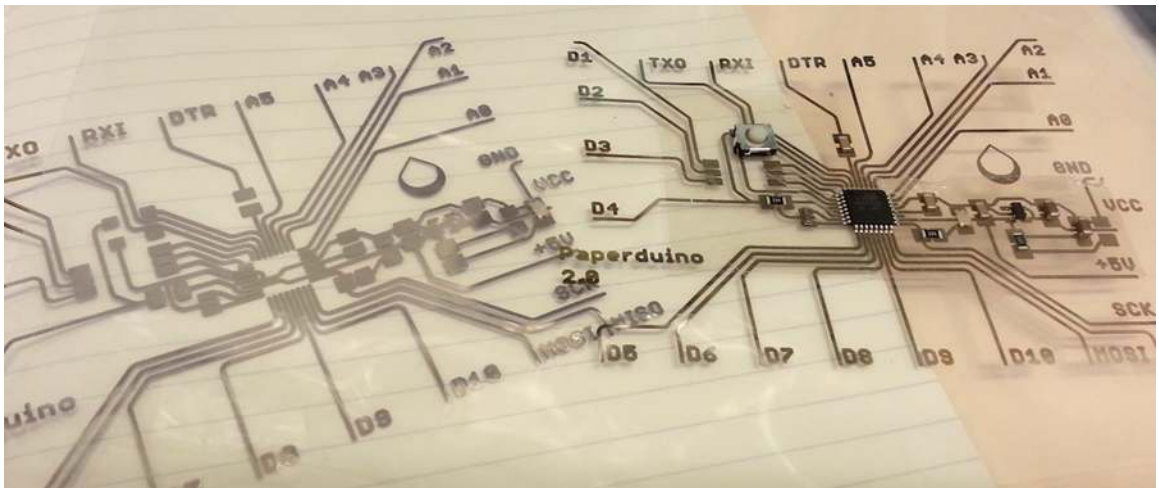

Figure 2.17. Examples of embedded complex circuit geometries in printed structures.

3.2 INKJET PRINTED METAL ELECTRODES

The combination of inkjet printing and low thermal budget photonic curing technology was explored for high performance metal contact development. The photonic curing system, as shown in Figure 2.18(a), is capable of delivering a high intensity, short duration (< 20ms) broadband light pulse (200-1400nm) from a directed xenon flash lamp, to generate the very high processing temperatures required for thin film densification, recrystallization and annealing, but without damaging the underlying temperature-sensitive substrates or co-integrated electronics. The photonic curing system is capable of delivering maximum peak power in excess of 20kW/cm^2 while the pulse width can be maintained as short as 30 microseconds.

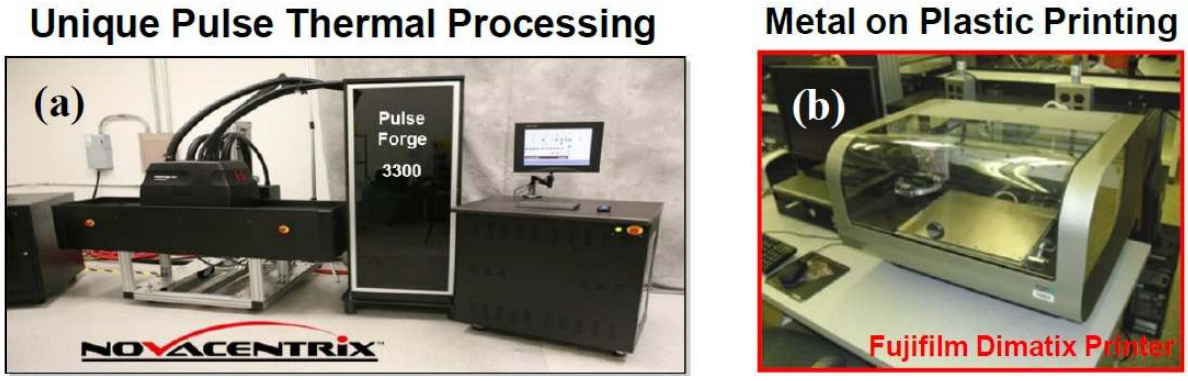

Figure 2.18. (a) PulseForge 3300 Photonic curing system and (b) DMP-2831 materials printer used for the development of silver electrode patterns on flexible plastic substrates.

The inkjet printer, shown in Figure 2.18(b), allows the deposition of fluidic materials on flexible substrates, utilizing a disposable piezo inkjet cartridge. The printer can create and define patterns over an area of about 200×300 mm and handle substrates up to 25 mm thick with an adjustable Z height. The temperature of the vacuum platen, which secures the substrate in place, can be adjusted up to 60°C. A waveform editor and a drop-watch camera system allows manipulation of the electronic pulses to the piezo jetting device for optimization of the drop characteristics as it is ejected from the nozzle. This system enables easy printing of structures and samples for process verification and prototype creation. The most unique feature of this table top printing system is the printhead

itself. To minimize waste of expensive fluids, each cartridge reservoir has a capacity of 1.5 ml. Cartridges can easily be replaced to facilitate printing of a series of fluids. Each single-use cartridge has 16 nozzles linearly spaced at 254 microns with typical drop sizes of 1 and 10 picoliters. In the present work, 10 pL ink-cartridges were used for the printing of silver electrode patterns.

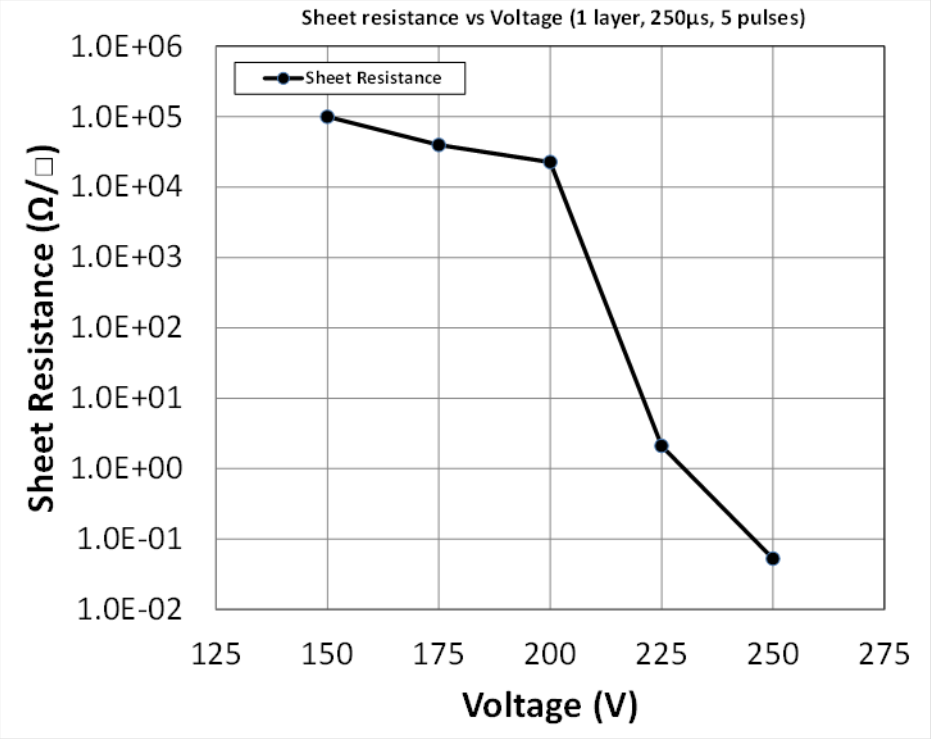

Figure 2.19. The impact of photonic curing on the electrical conductivity of printed silver electrodes.

The impact of photonic curing on the sheet resistance of a printed silver resistor is shown in Figure 2.19. The Ag patterns were printed on PET-based Novele substrates, which are suitable for low-cost and low-temperature applications. The photonic curing space was defined by the thermal-damage threshold of the flexible substrates. The impact of the 250µs wide photonic pulses on the sheet resistance of the Ag line was analyzed, and the results shown in Figure 2.20, over the applied voltage range of 150-250V. The sheet resistance remained high over the voltage range of 150-200V, while an increase in the applied voltage to 225V resulted in a significant reduction in sheet resistance to a value of $2.1\Omega/Sq$, which is suitable for interconnect applications. As the applied voltage was further increased to 250V, the sheet resistance value decreased by an order of magnitude to about 5.3×10^{-2} Ω/Sq.

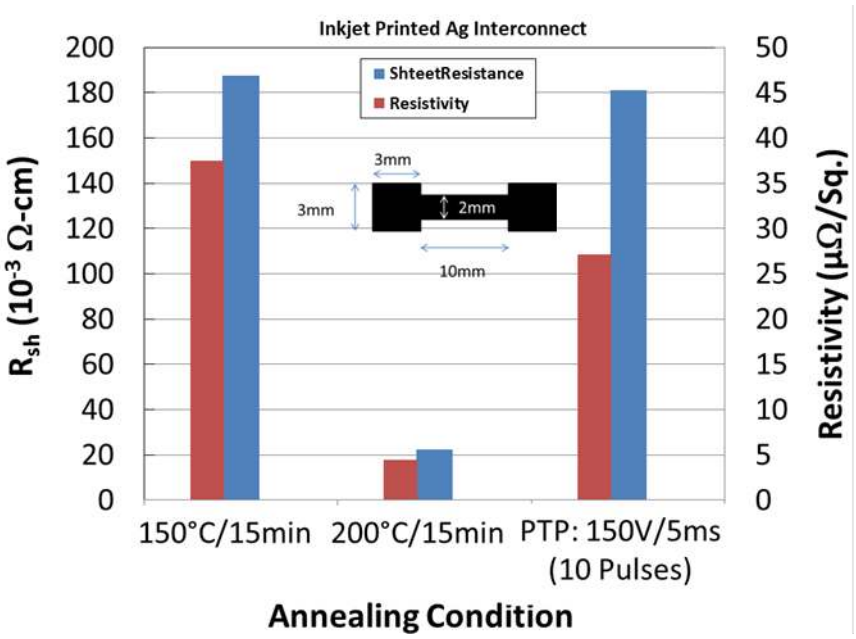

Figure 2.20. Impacts of photonic curing and conventional hot-plate sintering methods on the electrical properties of inkjet printed Ag electrode patterns.

The efficiency of the photonic curing process was evaluated by establishing a comparison with the convention hot-plate sintering method. Figure 2.20 shows the effects of photonic curing and hot-plate sintering on the electrical properties of a printed silver resistor. It was possible to achieve a sheet resistance value below 100 $m\Omega/Sq$ by photonic curing at a pulse-width of 5ms. The electrical properties were comparable to those achieved by conventional sintering at 150°C, and the observed electrical performance of printed silver patterns is suitable for flexible electronic applications. The photonic curing process was optimized for further reductions in the silver metal-line resistance, while the multi-layer printing option was also available to further improve the electrical performance of the interconnects in all-printed electronic applications.

The inkjet printing technique offers simple and inexpensive processing of interdigitated electrodes (IDEs) for advanced sensor and electronic-circuit integration on flexible substrates. The IDE geometry can be tailored to achieve the desired signal response from the integrated sensor or other electronic components and devices. The digital printing method, using a CAD file, eliminates the costly mask redesign step to accommodate the modified designs. Additionally, the printing process eliminates the deposition, photolithography, and etching steps that are typically required in a cleanroom environment to define similar electrode configurations.

Figure 2.21 shows well-defined IDE patterns printed on PET substrates. The optimum line-definition was achieved using a drop-spacing of 20μm. The electrical waveform and nozzle voltages were adjusted to achieve a consistent drop velocity of about 7.5 m/s. The platen temperature was maintained at 50°C during printing. The print quality and electrical performance of IDE patterns were evaluated in terms of the inter-electrode capacitance. A capacitance value of 17.5 pF was measured for the integrated capacitor design on low dielectric constant PET substrates indicating well-controlled finger spacing and metal line-width. The observed results show promise for the development of flexible electronic circuits employing inkjet printed interconnects, electrode patterns, and passive electronic components.

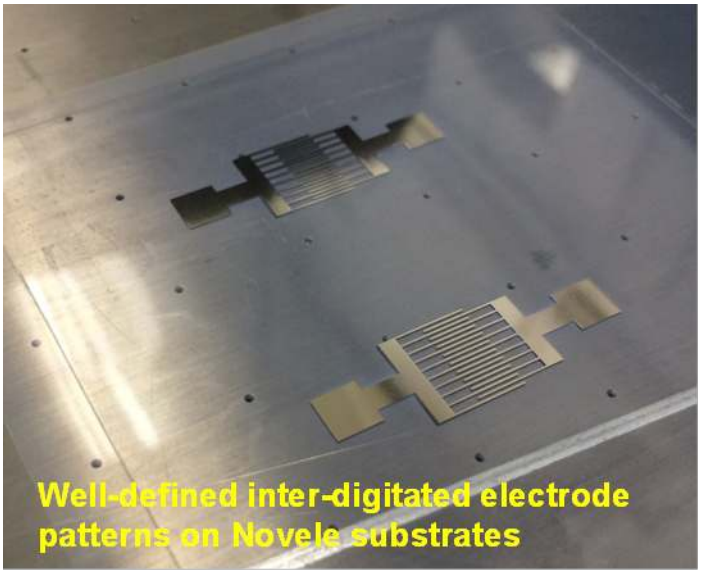

Figure 2.21. Inkjet printed interdigitated electrode patterns on flexible PET substrates.

3.3 INKJET PRINTED METAL PATTERNS

The low thermal budget of the photonic curing technology was explored for high performance metal contact development. Sheet resistance values below 100 $m\Omega/Sq$ were successfully achieved on flexible substrates using photonic curing. The electrical properties are comparable to those achieved by conventional sintering at 150°C. The observed electrical performance of printed silver patterns is suitable for flexible electronic applications. However, the flexibility and mechanical reliability of printed metals are critical considerations for advanced device development and manufacturing technology integration.

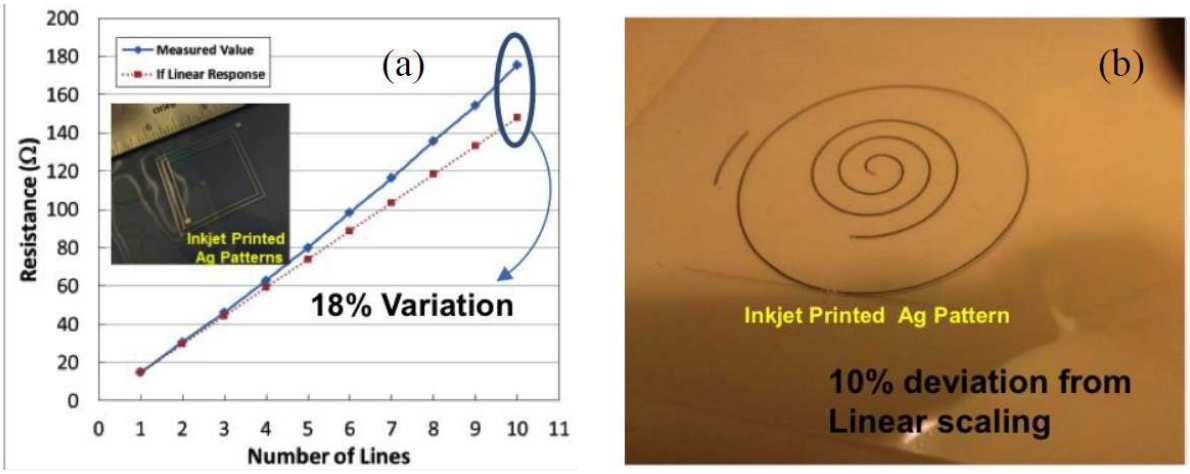

Figure 2.22. Printed Ag test structures to evaluate resistance scaling: (a) Rectangular and (b) Spiral.

Figure 2.22 shows an attempt made to analyze the impact of line definition on the scalability of line resistance. For 90° transitions in the printed pattern, a deviation of 18% from the expected linear response was measured for a test pattern with ten turns as shown in Figure 2.22(a). A spiral of the same length as the rectangular pattern with ten 90° turns was also printed, as shown in Figure 2.22(b),

to analyze the impact of line definition. The spiral pattern showed a significant improvement in the resistance scaling indicating that curved transitions lead to a better line definition. The observed results suggest that the spiral pattern design should also be considered when printing metal interconnects and electrode patterns.

3.4 PRINTED POLYMER SUBSTRATES FOR STRAIN GAUGES

Six polymer substrates were prepared by additive printing techniques, to conduct mechanical testing (Figure 2.23). These structures were printed using the Stratasys Objet24 3D printer using the polymer Vero White Plus FullCure 835 UV polymer.

Figure 2.23. Additive printed polymer substrates for strain testing.

The substrates were polished with several grit polish levels to obtain better secondary print surface before proceeding to encapsulate the gauge patterns (Figure 2.24). However, we found that this tends to promote print instabilities, especially for coarser final polishing.

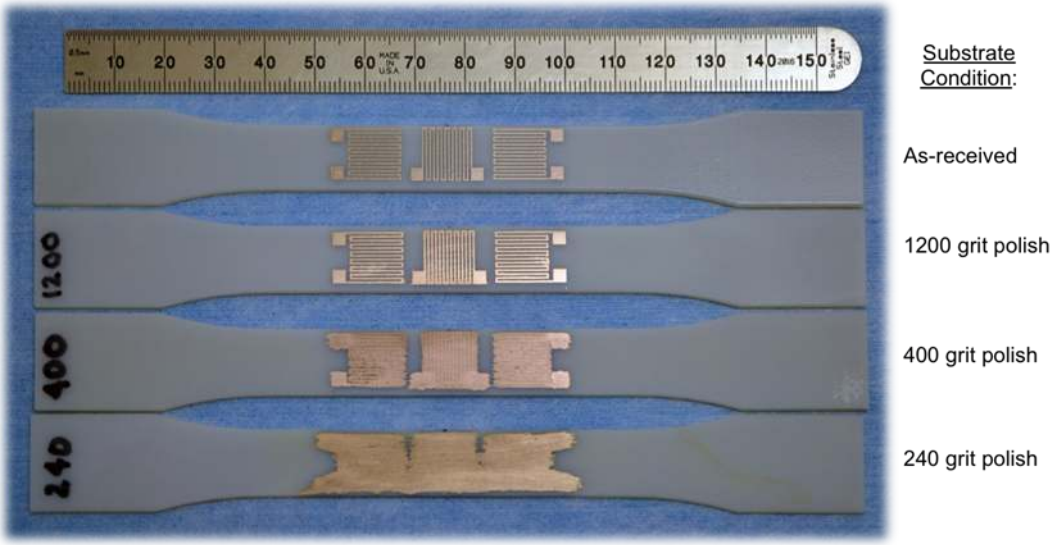

Figure 2.24. Polishing of the printed structures with several grit polish levels.

The printed lines were continuous but appeared to exhibit wrinkles, which might affect the performance of the strain gauge. A close up of the wrinkled structures is shown in Figure 2.25(a) and 2.25(b). Further analysis revealed that the wrinkles are folds several micrometer in height (Figure 2.25(c)), and wrinkles of this size and density could potentially distort the behavior of a gauge where unfolding rather than straining occurs upon elongation.

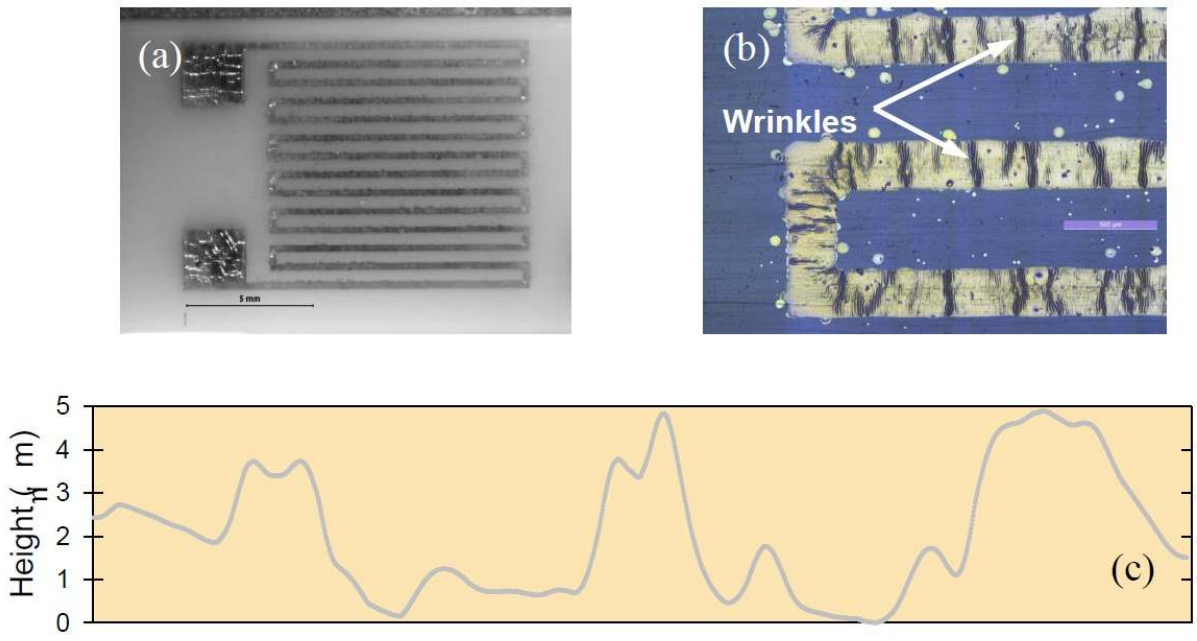

Figure 2.25. A close up of the wrinkled structure of the polishing of printed structures.

4. TASK 3: LOW COST PRINTED SENSORS

The objective of this task was to demonstrate low cost printed sensor development by non-vacuum deposition techniques employing low thermal budget photonic curing. This was to involve co-integration of metal and/or semiconductor layers to establish a diverse sensor technology platform. The initial application for the low cost sensor technology was to be a thin film temperature sensor for energy efficient buildings, defense applications, and manufacturing diagnostics. The sensor was to be passive thin film piezoelectric design, and was to communicate with local receivers using radio frequency surface acoustic wave technology (RF-SAW), with the goal of sensing temperature changes based on physical changes in the conductive lines. The research performed in this project was to characterize in-house fabrication methodologies available for direct-write sensors and radio frequency (RF) antennas that can be combined to produce a fully passive sensor that is readily reproducible by ink jet, screen, aerosol jet or other direct-write techniques.

4.1 COMPLETE SAW DEVICE STRUCTURE

A schematic of the complete device structure with typical dimensions of various components for a high frequency design is shown in Figure 3.1. A simple SAW device was designed and fabricated as a first step. A delay line structure was fabricated to demonstrate SAW operation and a simple transducer with reflector structure to demonstrate sensor operation. The first design template contained an array of RF-SAW structures of various feature sizes ranging from 9.8 to 500 microns. The change in reflector time delay due to external stimuli, such as temperature change, is tracked. Having two tracks allows one track to be used for temperature compensation while the other track may be used to sense another parameter. By fabricating this array of features, we were able to characterize the line width, line spacing (pitch) and coating thickness, and achieve reproducibly. Once the fabrication limitations were understood, various substrate materials and inks were explored to optimize device performance and minimize feature sizes with a line width goal of 0.8 microns or smaller.

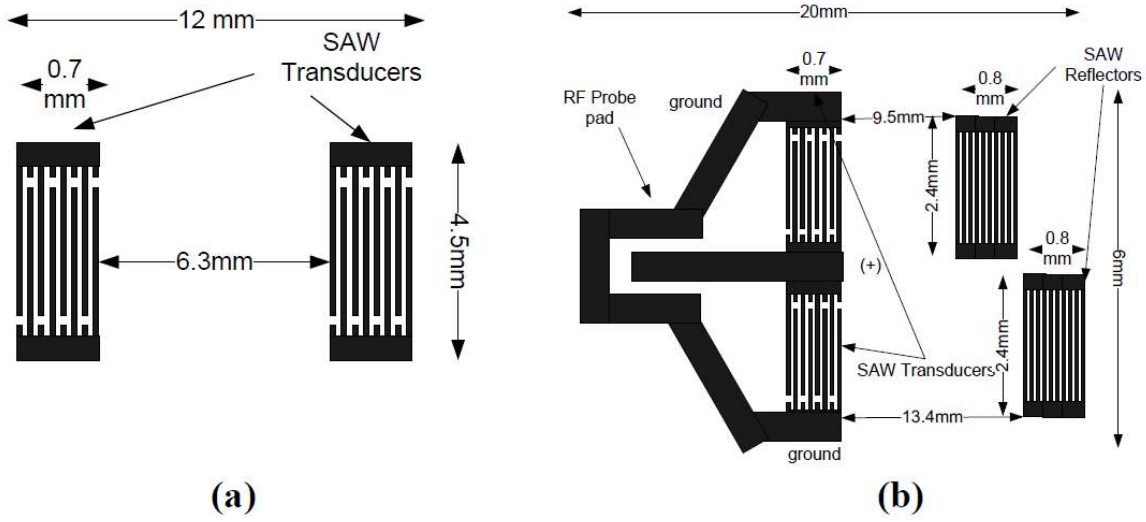

Figure 3.1. (a) SAW Delay line structure with two transducers (the electrode widths = 19.8um for 40 MHz operation on LiNbO3), (b) A simple single frequency sensor with two tracks, each having a reflector which will produce a reflection at a different time delay.

4.1.1 Thin Film Development

A simple delay line structure can be realized on suitable materials such as YZ-$LiNbO_3$, PZT, and ZnO. The SAW response depends on the substrate and metal electrode quality. The SAW coupling, velocity and reflectivity of the electrodes are the parameters that were considered for the sensor design. The focus was on the development of low temperature ZnO thin films as the first step. The films were deposited by a sputtering technique on Si and plastic substrates. The thin film properties and SAW device characteristics were correlated with modeling to establish the impact of dispersion characteristics for high performance device development. The metal thin film development focused on Ag and Al thin films, which were processed by e-beam evaporation and inkjet printing techniques.

4.1.2 Metal Electrodes

The e-beam evaporation process was optimized for low temperature deposition of metal thin films on flexible substrates. We targeted a process temperature of less than 150°C for the various metal films which was suitable for plastic substrates of interest. Figure 3.2 shows the Ag thin film patterns deposited on various plastic substrates under room temperature conditions. A sheet resistance of 0.096 Ohms/Sq. was measured on 300-nm-thick Ag films, which was suitable for diverse interconnect and electrode designs. The measured resistivity of the films was about 2.88×10^{-6} Ohm-cm indicating that the room-temperature metal deposition process was suitable for plastic integrated device development.

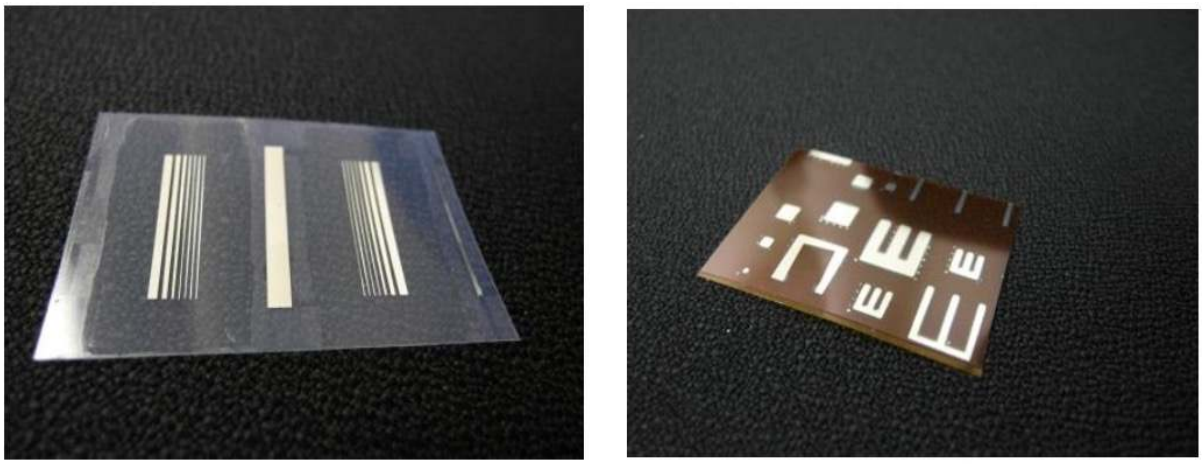

Figure 3.2. Room temperature Ag thin film patterns deposited on plastic substrates by e-beam evaporation technique: (a) Novelle® PET, (b) PET.

4.2 SENSOR DESIGN

The efforts in this phase of the Project involved the design, development, fabrication and performance validation/testing of passive wireless sensors that may be mass-produced using techniques developed within the Project. Such sensor development activities revolved around radio frequency surface acoustic wave (RF-SAW) techniques, which hold promise for fabrication using direct-write technologies.

The ORNL RF-SAW efforts focused on modifying and scaling RF-SAW designs that were provided by Prof. Donald Malocha (University of Central Florida) and his post-doctoral assistants. Investigations centered on a reference design set for operation in the 915 MHz (ISM band) frequency range and then scaling the design to the 250 MHz and 49 MHz frequency range. The implications for direct write sensor printing were driven by the fact that the RF-SAW's operating frequency is inversely proportional to the line widths of the interdigitated "fingers" of the SAW device (Figure 3.3). While ORNL has the capability of producing a wide range of line widths, thereby providing the RF-SAWs with a wide range of operating frequencies, the project efforts were concentrated on using the 50 micrometer conductive ink printing capability – meaning that the RF-SAW designs operated at a lower frequency range than what they were designed for.

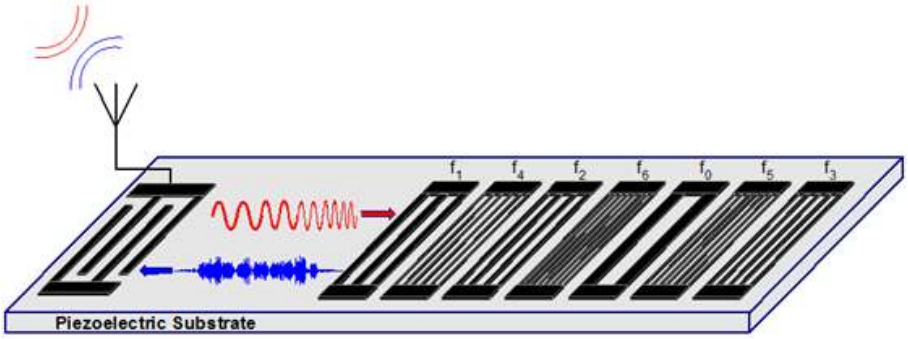

Figure 3.3. Representative 7-sensor element RF-SAW structure.

The broadband RF test and measurement equipment necessary to verify performance of the devices and components were assembled at ORNL, and a set of RF-SAW "reference" devices, designed to operate in the 915 MHz frequency range, were designed and fabricated. An annotated photomicrograph of one of the devices is shown in Figure 3.4. The "coded reflectors" are using an orthogonal frequency coding technique, which allows for easy signal discrimination in the interrogated signal from which the sensor reading is extracted.

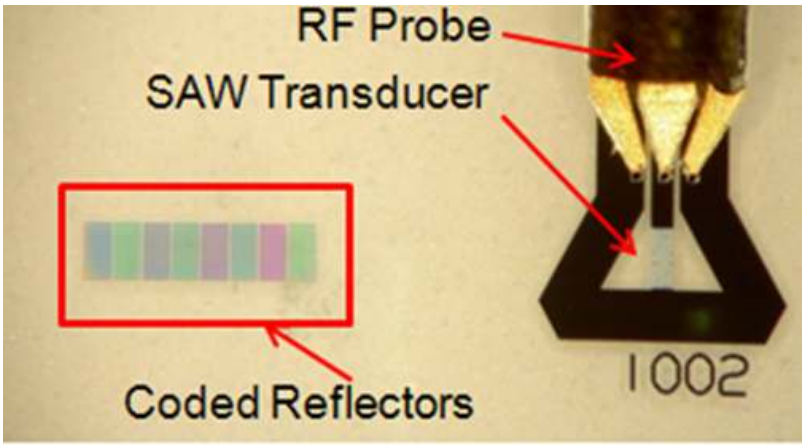

Figure 3.4. Photomicrograph of "reference" RF-SAW device.

Operation of the RF-SAW with sensors, either on-board (Figure 3.5) or off-board (Figure 3.6) relies on an interrogating RF signal (narrowband, pulsed, centered on the designed operating frequency) being received by the RF-SAW. The RF-SAW then generates a return signal that the test and measurement system receives and decodes.

"Interrogation" of the 915 MHz RF-SAW returned a frequency spectrum that was broad. FFT transformation of this spectrum revealed the temporal nature of the signal, from which the specific responses from the coded reflectors were observable, as shown in Figure 3.7.

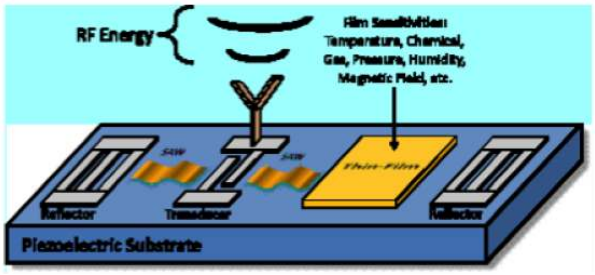

Figure 3.5. Design with on-board sensors.

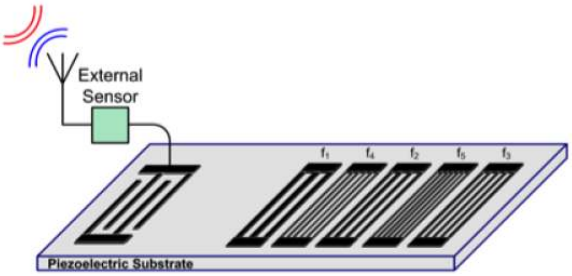

Figure 3.6. Design with off-board sensor.

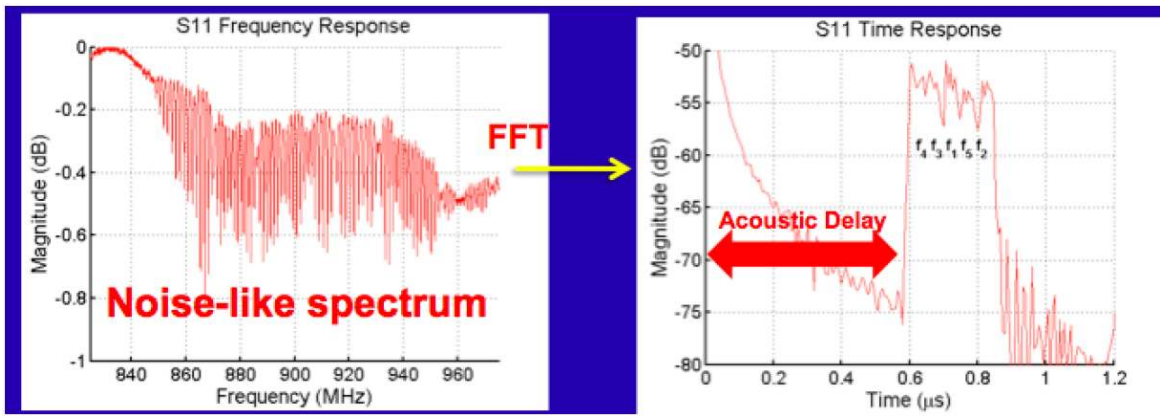

Figure 3.7. Broadband frequency and temporal response of the tested RF-SAW.

Deciphering the sensor signals occurs in either the frequency- or temporal-domain. Simulations were generated for the predicted response. A representative simulation and measured RF-SAW set of signals is shown in Figure 3.8.

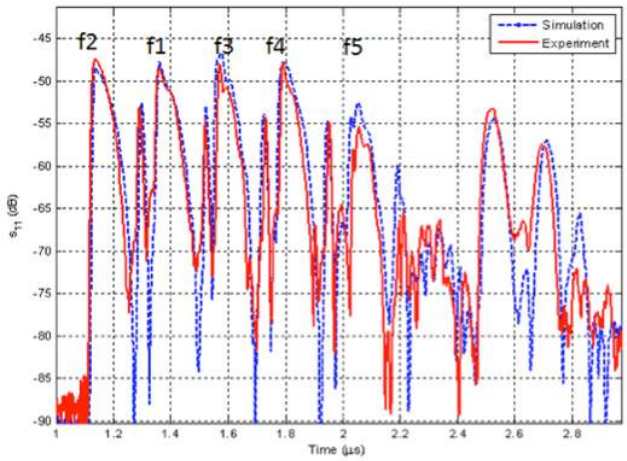

Figure 3.8. RF-SAW "readings" for configuration with 5 elements.

In collaboration with Prof. Malocha, we investigated the use of Langatate (LGT) as a substrate for high temperature RF-SAW operation (sensing and communications). Preliminary results revealed that a design capable of sustained operation at 1400°C is possible. A photograph of a fabricated device, with a photomicrograph insert of the actual SAW structure, is shown in Figure 3.9. This device was tuned for 915MHz operation, but can be scaled to the 50 micrometer line width of the aerosol jet printers used in the project. A photograph of an RF-SAW on LGT after it has been subjected to 1400°C for 2 hours is shown in Figure 3.10.

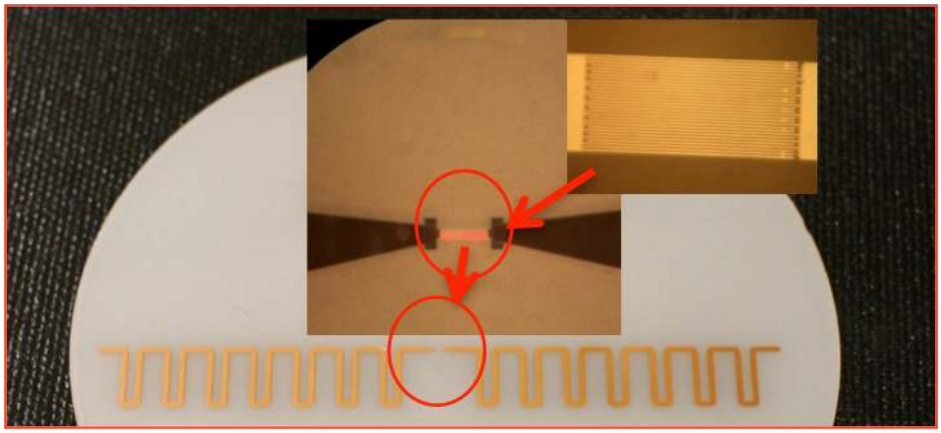

Figure 3.9. Annotated photomicrograph of an RF-SAW device capable of operation at high temperature.

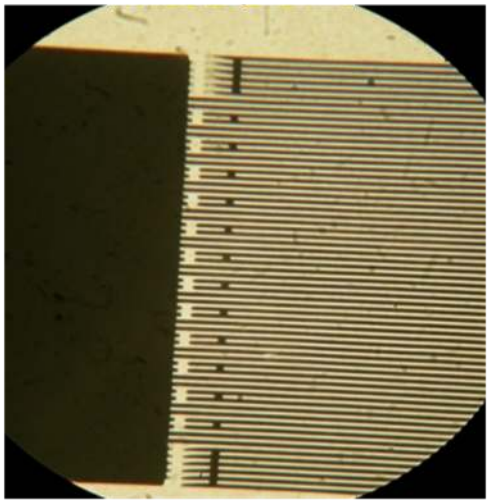

Figure 3.10. RF-SAW on LGT after 2 hours at 1400°C.

The key findings from this study are as follows:

- The film thickness is best if it is approximately 1-2% of the operating wavelength. There is significant degradation in performance if the film thickness exceeds 4% of the operating wavelength.
- When using aluminum electrodes, the denser the metal, the thinner the metal thickness for optimal performance. For example, in the device shown in Figure 3.9 with Al electrodes, the optimal line thickness is in the 800 nm to 1500nm range, but should absolutely not be more than 3 um thick.
- Examining layouts with differing positions for RF probe test points led to a reference dipole

antenna structure suitable for testing (and calibrating) the RF test and measurement system. This dipole layout had a minimum layout line size of 9.8 um, and fits within a 5" x 5" window. The reference dipole was not suitable for the 50 micrometer line width fabrication. Scaling of the system to this line width, with the accompanying decrease in RF operating frequency, is underway.

- Optimization of the RF-SAW in terms of overall performance was multivariate, with the most important parameters being antenna gain, fractional antenna bandwidth, and operating frequency. A representative tradeoff diagram is presented as Figure 3.11.

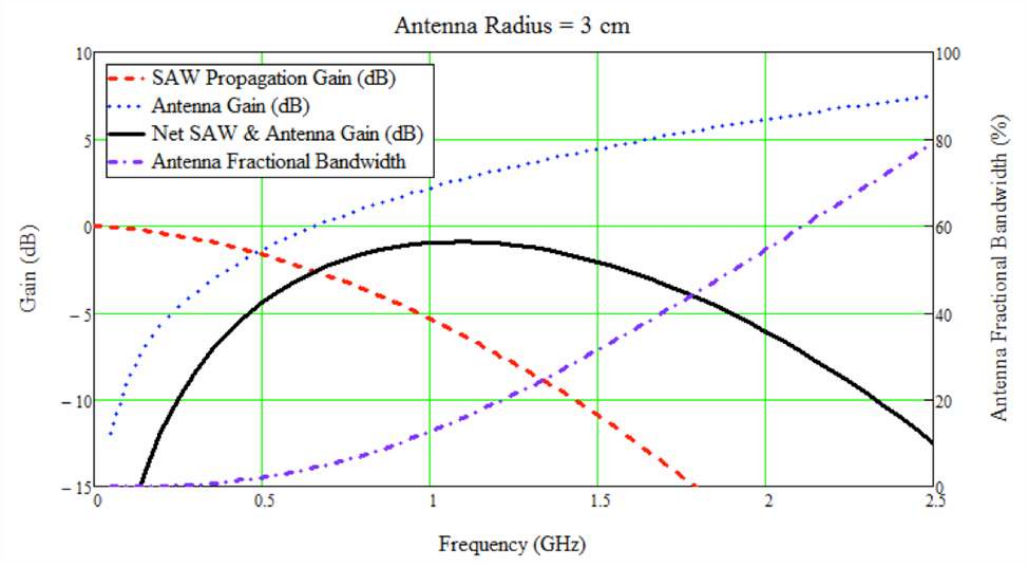

Figure 3.11. Optimization of an RF-SAW.

Given the line width limitations in the direct write devices, we have turned attention to harmonic operation. While this is suboptimal for realistic operation (antenna gains, etc.) it allows wider line width device fabrication while operating in higher frequency ISM bands.

4.3 LOW TEMPERATURE ZnO THIN FILMS

The low temperature semiconductor thin film development was focused on sputtered ZnO thin films. The pulsed-dc sputtering process was optimized to process high quality thin films at low temperatures suitable for integration on flexible plastic substrates. The sputtering process conditions for the investigation were as follows: RF Power=400W, Pressure=5 mTorr, Process Temperature=25-200°C, Ar/O_2 flow ratio=0.25, Pulsing Frequency=300kHz, Duty-cycle=0.76.

Figure 3.12 shows the properties of 78-nm-thick films deposited at a temperature of 200°C. The XRD results indicate the formation of predominantly c-axis oriented ZnO films, which are desired for high performance device development. A refractive index value of 2.066 was measured at 600nm by ellipsometry technique, indicating the formation of a dense ZnO microstructure at a low temperature of 200°C.

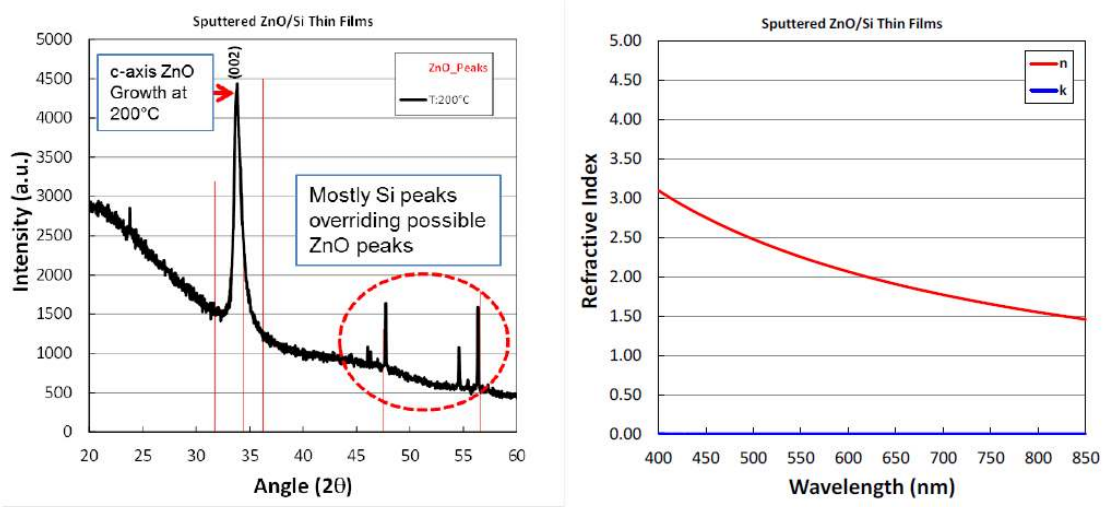

Figure 3.12. Properties of sputtered ZnO thin film processed at 200°C: (a) crystallinity, (b) optical n-k dispersion.

Figure 3.13(a) shows that the ZnO deposition rate was well maintained at around 0.76Å/s in the temperature range of 100-200°C. It decreased to about 0.60Å/s at a deposition temperature of 25°C. As shown in Figure 3.13(b), the pulsed-dc sputtering technique was effective in inducing c-axis orientation in the ZnO thin films even at a low temperature of 200°C. The c-axis orientation was well-maintained even at a deposition temperature of 25°C which is promising for device development on flexible substrates.

Temperature (°C)	Deposition Rate (Å/s)
25	0.60
100	0.76
200	0.76

(a)

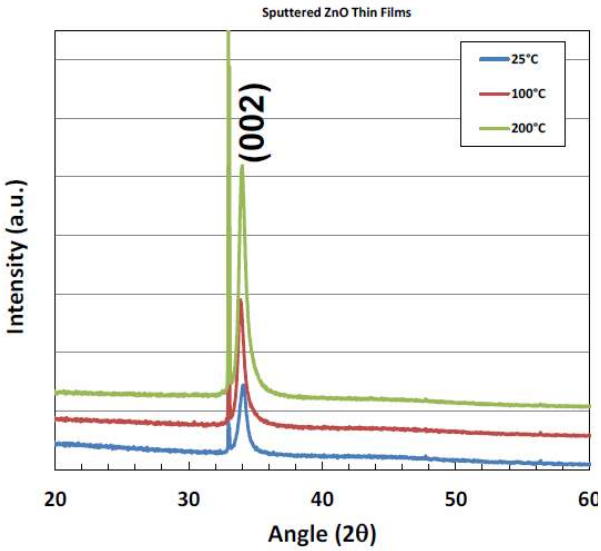

(b)

Figure 3.13. The effect of process temperature on the (a) deposition rate, and (b) crystallinity of ZnO thin films.

Figure 3.14(a) shows the optical transmittance of the films as a function of process temperature in the range of 25-200°C. The ZnO thin films were deposited on fused quartz substrates for the optical

transmission measurements. The optical transmittance of the film was greater than 80% in the wavelength range of 400-700 nm even at a deposition temperature of 25°C. The optical quality of the films was analyzed by spectroscopic ellipsometry. Figure 3.14(b) shows the n-k dispersion characteristics of the ZnO thin films deposited on Si substrates. A decrease in process temperature to 25°C did not influence the n-k dispersion characteristics appreciably indicating that the optical density of the films was well-maintained even down to a process temperature of 25°C. Overall, the pulsed-dc sputtering technique shows promise for the low temperature processing of the semiconducting ZnO thin films at plastic compatible process temperatures. The observed results suggest that a combination of the low temperature ZnO thin films and low-thermal budget pulse thermal processing technique is worth exploring for highly functional device development on flexible substrates.

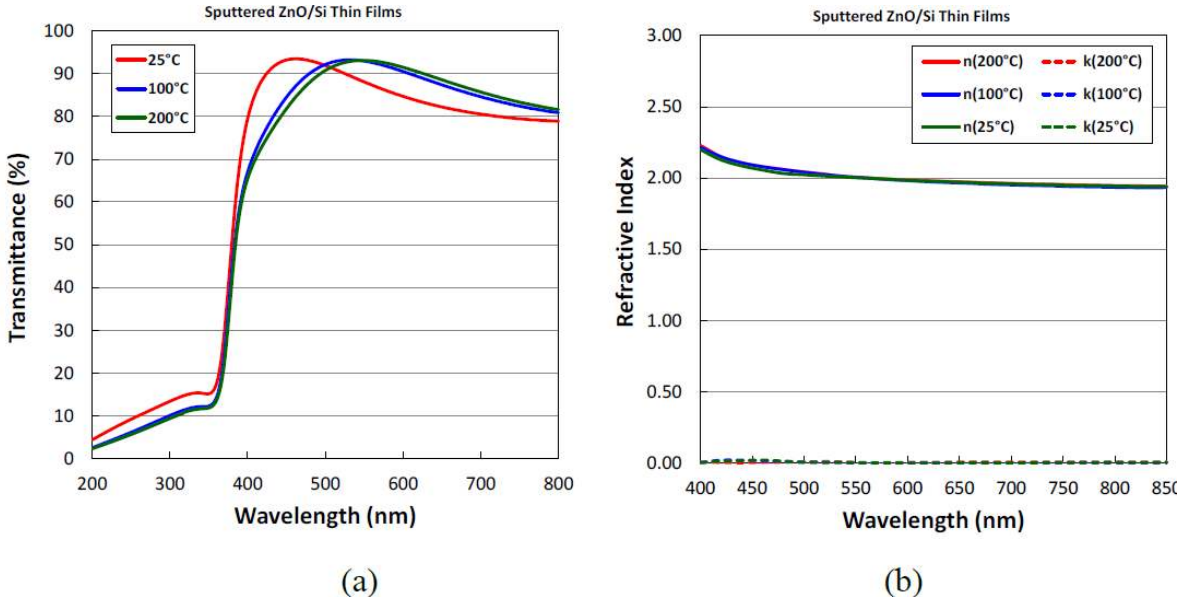

Figure 3.14. The impact of process temperature on the (a) optical transmittance, and (b) n-k dispersion characteristics.

Table 3.1. Various metal oxide thin film configurations under investigation for the flexible electronic applications

Metal Oxide Film Configurations	Characterization
• ITO/PI • ZnO/PI • ITO/ZnO/PI • ITO/ZnO/ITO/PI • (ITO or ZnO)/SiO_2/Si	• Microstructural • Optical • Electrical • UV Response

4.4 TRANSPARENT CONDUCTING OXIDE THIN FILMS

The focus for the next stage of the project was on the development of high quality transparent conducting oxide (TCO) thin films on plastic substrates. The details of various metal oxide thin film configurations under investigation are listed in Table 3.1. The initial investigation focused on room temperature processed ZnO and ITO thin films. The pulse thermal processing (PTP) technique was used for the low temperature annealing of the TCO thin films for plastic integration. The results of our initial investigation of the PTP technique are also discussed in the following sections.

4.4.1 Room Temperature ITO Deposition

Indium Tin Oxide (ITO) is a transparent conducting oxide suitable for electrical interconnects in diverse electronic devices. We attempted to process the ITO thin films on plastic substrate for low-cost sensor development. The ITO thin films were also deposited by pulsed dc sputtering technique to process high quality films at process temperatures below 100°C. Table 3.2 lists the typical sputtering conditions, and the corresponding ITO thin film properties. A low resistivity of the order of 1.26×10^{-3} was achieved for films deposited on quartz substrates at room temperature without any post-deposition thermal treatment. The observed results show the effectiveness of the pulsed dc sputtering mode in depositing high quality thin films at low process temperatures (<100°C).

Table 3.2. Room temperature deposition of ITO thin films by pulsed dc sputtering technique

Power (W)	Pressure (mTorr)	Dep-Rate (Å/s)	Resistivity (Ω-cm)
150	10	0.50	2.94E-03
150	5	0.63	1.26E-03
200	5	1.03	1.86E-03

The ITO thin films were also deposited on plastic substrates to analyze the impact of substrate on thin film quality. The films deposited on plastic substrates were also highly transparent as shown in Fig. 3.15(a). The ITO thin film transmittance was comparable on plastic and quartz substrates as shown in Fig. 3.15(b), indicating similar film quality. The intrinsic ITO thin film transmittance was greater than 75% in the visible part of the spectrum as confirmed by UV-VIS-IR spectrophotometer.

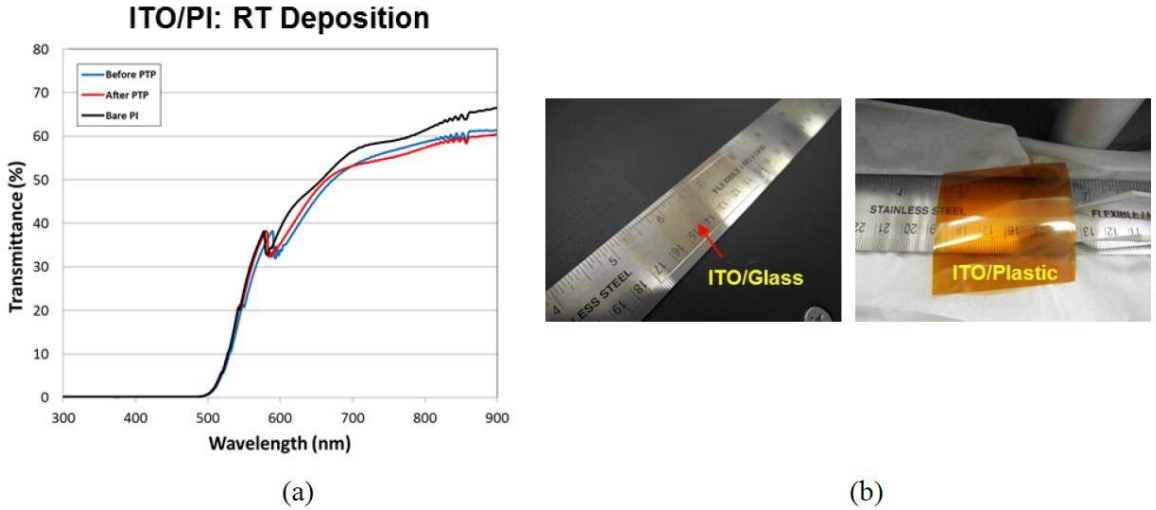

Figure 3.15. The optical transmittance of the room temperature deposited ITO thin films: (a) transmittance of ITP/PI thin films, (b) prototypes on quartz and plastic substrates.

The impact of the low thermal budget pulse thermal processing (PTP) on the electrical conductivity of the ITO/Plastic thin films was also analyzed. The PTP processing was carried out in the PulseForge 3300 system using 220V/5ms pulses. Figure 3.16 shows the impact of 10 pulses on the sheet resistance (R_{sh}) of the room temperature deposited ITO films. The R_{sh} values decreased substantially from 129 to 50 Ω//Sq. after PTP processing which is promising for processing high quality metal-oxide thin films on plastic substrates for advanced sensor development. Figure 3.16 also shows a resistivity below 10^{-3} Ohm-cm.

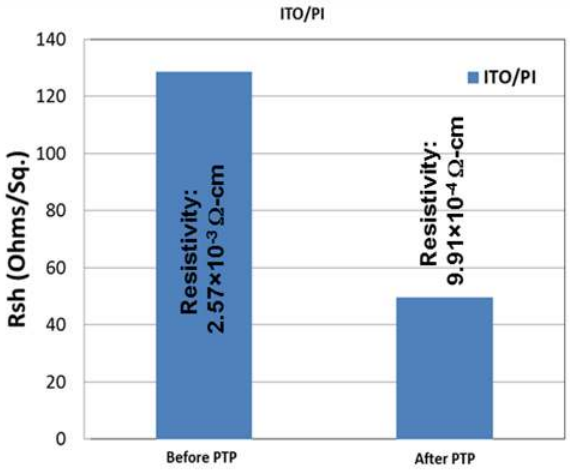

Figure 3.16. The impact of low thermal budget pulse thermal processing on the sheet resistance of ITO thin films sputtered at room temperature.

The impact of PTP processing on the electrical conductivity of room temperature deposited ITO thin films was further studied by depositing ITO films on SiO_2/Si substrates by the pulsed-dc sputtering technique. The results are shown in Fig. 3.17. The as-deposited ITO films showed a low sheet-resistance value of about 75 Ω/Sq showing the effectiveness of the pulsed dc sputtering mode in depositing high quality thin films at low process temperatures (<100°C).

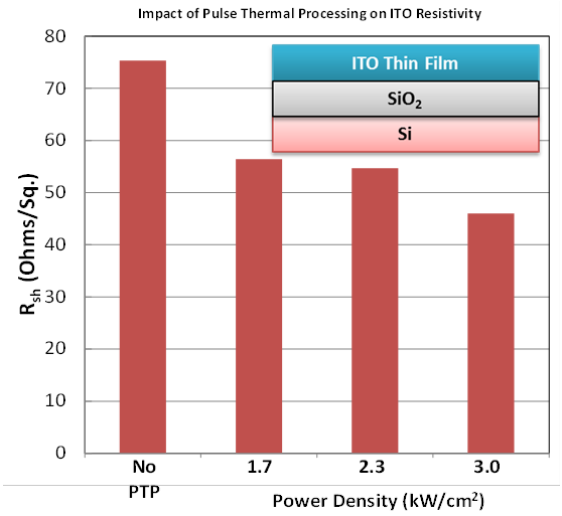

Figure 3.17. The impact of pulse thermal processing on the electrical performance of room temperature processed ITO thin films.

The ITO thin films deposited on plastic substrates showed high optical transparency (>75% in visible part of the spectrum – Figure 3.15). The PTP processing of the room temperature deposited ITO thin films was carried out in the PulseForge 3300 system at various power density levels as shown in Fig. 3.17. The sheet resistance value was found to decrease rapidly with an increase in the pulse power density level, and a value below 50 Ω/Sq was obtained at a power density level of 3.0 kW/cm^2. These results are promising for low temperature contact development for flexible electronic applications.

4.3.2 Room Temperature ZnO Thin Films

The room temperature sputtering process was extended to plastic substrates for high performance flexible sensor development. This development provides an alternate path for low-cost, high performance sensor development. Figure 3.18(a) shows the prototype device with ZnO thin film deposited on the inter-digitated electrode (IDE) pattern on a plastic substrate. The ZnO thin films were deposited by pulsed dc sputtering at room temperature. As shown in Fig. 3.18(b), the pulsed dc sputtering process was effective in depositing crystalline c-axis oriented films on plastic substrates. The observed results were promising for the integration of multifunctional sensors on plastic substrates.

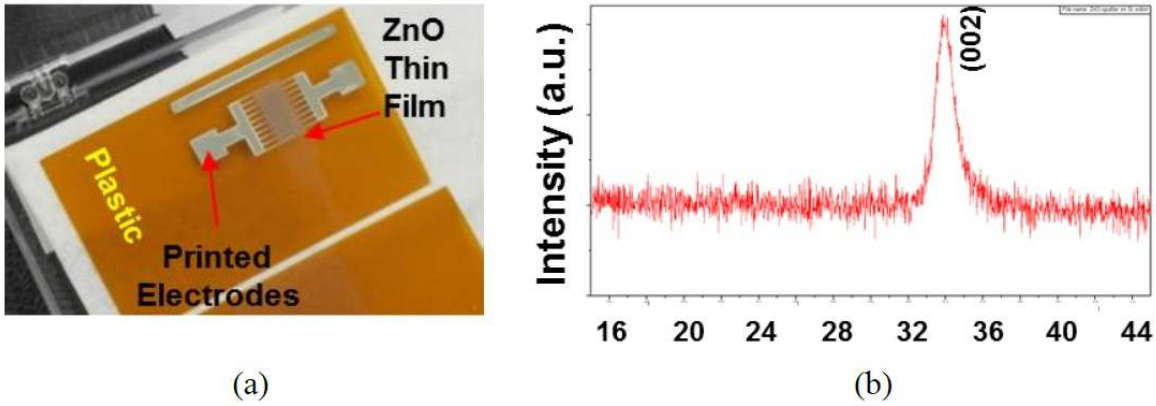

Figure 3.18. Room temperature deposited ZnO thin films: (a) thin film on inkjet printed Ag electrode pattern, (b) x-ray diffraction pattern showing c-axis orientation.

The impact of the PTP processing on the crystallinity of the ZnO thin films was also investigated. Figure 3.19 shows the impact of the PTP processing on the crystallinity of the ZnO thin films deposited on flexible polyimide (PI) substrates deposited at room temperature. The pulsed dc sputtering process was effective in depositing crystalline c-axis oriented films on plastic substrates. The PTP treatment at a power-density level of 3.0 kW/cm^2 was effective in enhancing the crystallinity of the ZnO thin films, which is promising for low temperature device integration. Detailed PTP investigation was carried out on ZnO thin films and devices for low-cost, high performance sensor development.

The impact of the PTP processing on the electrical conductivity of the ZnO thin films was also analyzed as shown in Fig. 3.20. The current-voltage (I-V) measurements were conducted on ITO/ZnO/PI structures processed at room temperature. The PTP treatment was carried out in the pulse power density range of 1.7-3.0 kW/cm^2 (220-275V applied voltage). The impact of the PTP fluence on the I-V characteristics is clearly evident in Fig. 3.20. The electrical conductivity of the ZnO thin films was found to increase with an increase in the pulse power density indicating an

improvement in the material quality, which is consistent with the XRD results showing an improvement in film crystallinity after PTP processing. Detailed PTP investigation were carried out to analyze its impacts on the crystallinity, electrical conductivity, and photo-response characteristics of ZnO thin films for flexible sensor development.

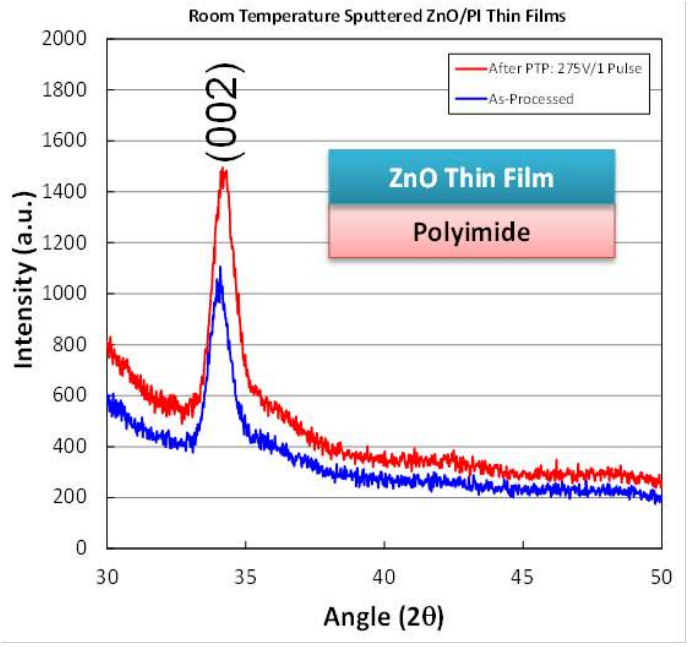

Figure 3.19. The impact of pulse thermal processing on the crystallinity of room temperature processed ZnO thin films.

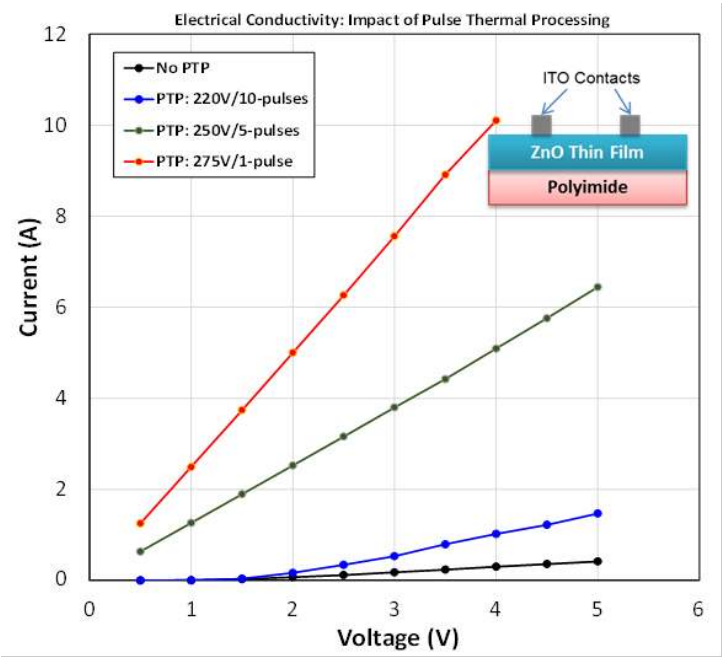

Figure 3.20. The impact of pulse thermal processing on the current-voltage (I-V) characteristics of room temperature processed ZnO thin films.

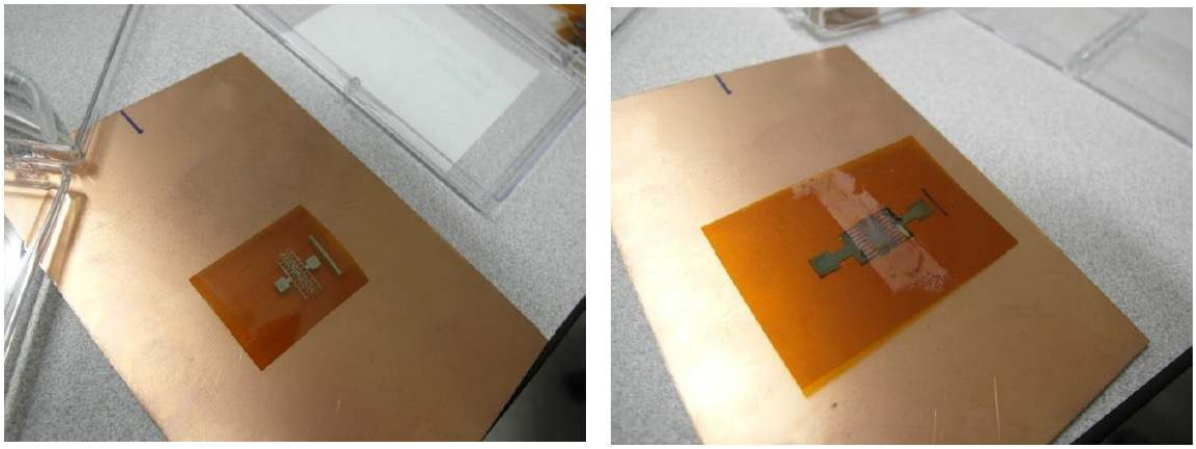

Figure 3.21. UV sensor with interdigitated Ag electrode pattern: (a) electrodes on top, (b) electrodes underneath ZnO film.

The UV response of the low temperature processed ZnO thin films on plastic substrates was evaluated using a 365nm excitation. The ZnO films were deposited at room temperature on polyimide substrates by pulsed dc sputtering. The film thickness was maintained at 200nm. The interdigitated silver electrodes were deposited on various films to evaluate the electrical and photo-response characteristics. Figure 3.21(a) shows a ZnO sample with inkjet printed Ag electrodes on the top surface of the film. The inkjet printed Ag electrodes had a low sheet resistance of 0.05 Ω/Sq on polyimide substrates. However, the Ag electrodes on top of the ZnO films showed high resistivity not suitable for electrical measurements. The observed high resistivity indicated a reaction between the Ag ink and ZnO film occurred during the curing process.

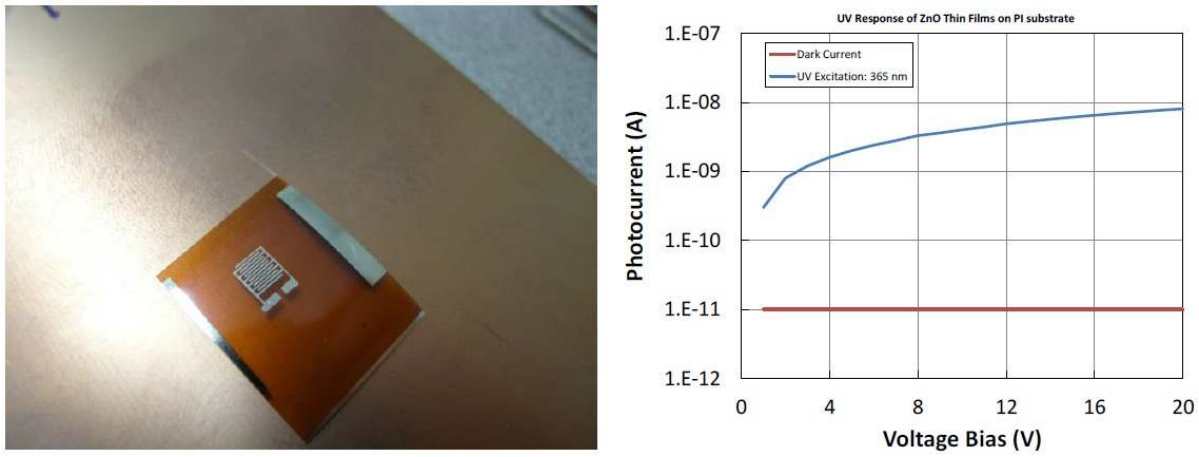

Figure 3.22. (a) ZnO UV sensor with IDE pattern, (b) Photo-response under 365nm illumination.

We attempted the deposition of ZnO thin film on an interdigitated Ag electrode pattern, as shown in Fig. 3.21(b), which was cured prior to ZnO deposition. The Ag electrode resistivity did not show any effect of ZnO deposition in this configuration, indicating the Ag ink and ZnO material did react in the top electrode configuration. The UV response of the room temperature deposited ZnO films was further evaluated in top electrode configuration as shown in Fig. 3.22(a). The top Ag electrodes were deposited by an e-beam evaporation technique at room temperature using a shadow mask. The electrode definition was well maintained on the ZnO film deposited on a flexible substrate. The UV photo-response of the ZnO films was evaluated using a 365 nm UV excitation. The UV power

density was 68μW/cm^2. As shown in Fig. 3.22(b), the ZnO films showed a very low dark current in the applied voltage bias range of 0-20V. It was not possible to measure the absolute dark-current due to the detection limit of the Keithley 2400 SourceMeter. The films showed high photoconductivity under UV excitation. The photocurrent increased by more than 2 orders at a bias voltage of 5V. The observed results are promising and a show path towards low temperature integration of sensor elements on flexible substrates.

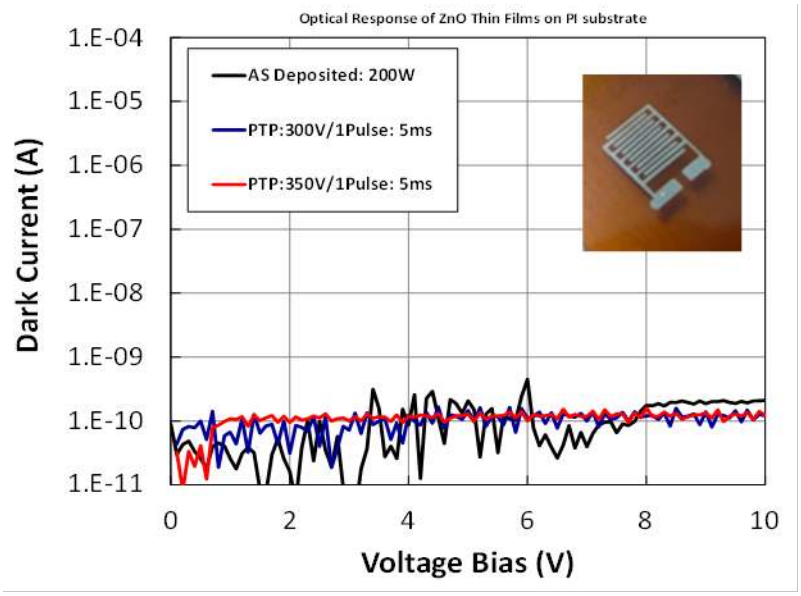

Figure 3.23. The dark-current characteristics of as-deposited and PTP processed ZnO thin films. The films were deposited on polyimide substrates at room temperature.

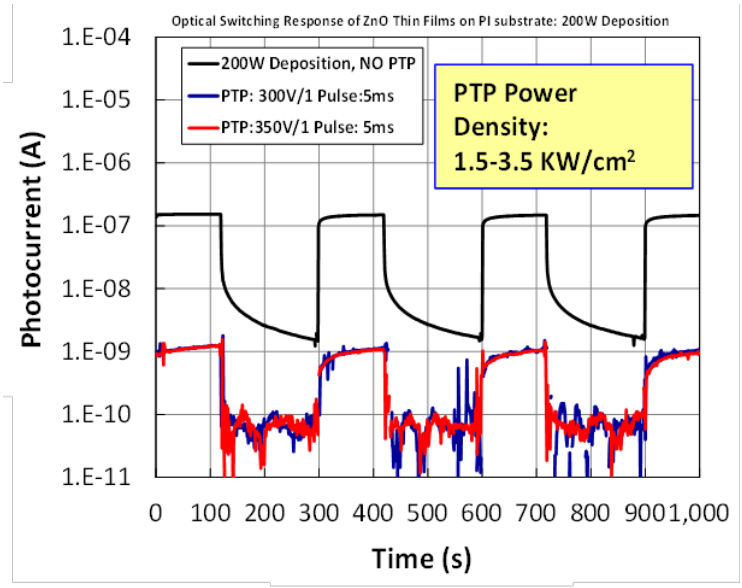

Figure 3.24. The photo response characteristics of as-deposited and PTP processed ZnO thin films. The films were deposited on polyimide substrates at room temperature.

The next step was to establish the photo- response of the ZnO thin film based UV sensor as a function

of PTP processing conditions. Detailed PTP investigation were carried out to analyze its impact on the structural, electrical, and UV photo-response characteristics. ZnO thin films were deposited on polyimide substrates by pulsed dc sputtering at room temperature for flexible UV sensor development. The impact of the pulse thermal processing (PTP) on the dark current and photo-response of 200-nm-thick films was also analyzed. Figure 3.23 shows the dark-current characteristics of as-deposited and PTP processed ZnO thin films. The room temperature deposited ZnO films exhibited low dark-current consistent with the x-ray diffraction results showing high crystallinity.

Figure 3.24 shows the pulsed photo-response of as deposited, and PTP processed ZnO thin films. The as-deposited films showed more than an order shift in the ON and OFF state current indicating good film quality. The rise time of the photocurrent was found to be much shorter than the decay time under UV excitation. The PTP processing resulted in significant improvement in the switching characteristics as shown in Figure 3.24. Both the rising and trailing edges of the pulsed current showed sharp transitions after PTP processing indicating further improvement in the film's density and crystallinity at a plastic compatible thermal budget. The observed results are promising for the low temperature integration of thin film sensors on flexible substrates using a combination of low temperature deposition processes and low thermal budget pulse thermal processing technique.

4.3.3 ZnO Particle Coatings

One effective way to deposit high quality material on low temperature substrates is to decouple the annealing step from the deposition step. High quality ZnO particles were created by high temperature oxidation of the NF ZnS particles in an oxygen atmosphere. As shown in Fig. 3.25(a), it was possible to achieve a well-crystallized polycrystalline ZnO phase by oxidation of NF-ZnS particles. The ZnO coatings were screen-printed on the plastic substrate to analyze their electrical conductivity characteristics.

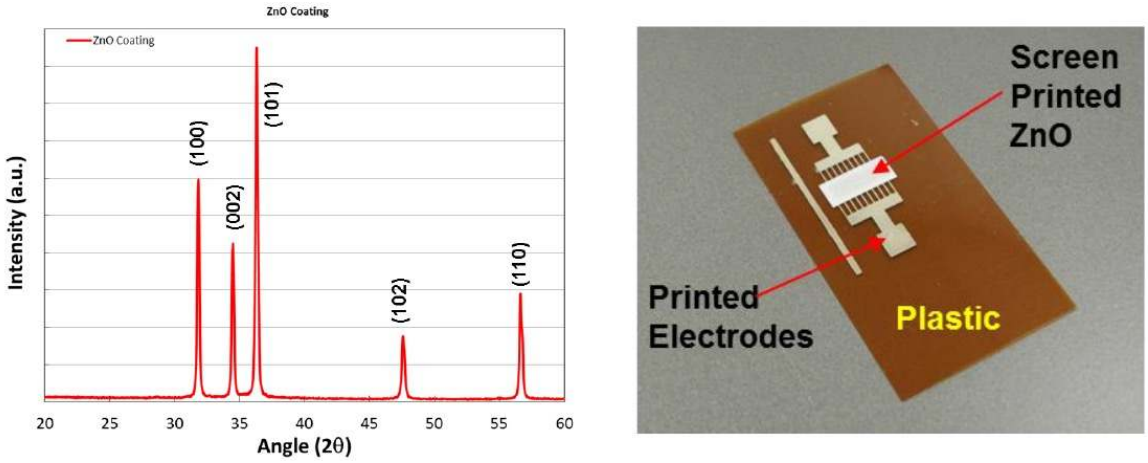

Figure 3.25. Screen-printed ZnO coatings: (L) x-ray diffraction patterns, (R) coating on inkjet-printed electrode pattern on plastic substrate.

In order to achieve large scale and low cost NF-nanoparticles for functional electro-optical devices the nanoparticles need to be stabilized in order to have the desired properties. As produced NF-nanoparticles aggregate (Figure 3.26a) and their solutions are not stable, optically highly scattering. The films are discontinuous and the observed photoluminescence appears to emerge from high energy states (surface defects). When we modified the nanoparticles (Figure 3.27b) with inorganic ligands we found that the solutions were stable, there no measurable light scattering and the optical properties of inorganic-ligated nanoparticles show well-defined band gap and photoluminescence. In addition,

the NF-nanoparticles tend to self-organize in one-two and three-layer assemblies and show smaller cluster size. In Figure 3.28 we show TEM images of the unmodified NF-nanoparticles cluster (Figure 3.28a) and stabilized NF-nanoparticles clusters Figure 3.28b).

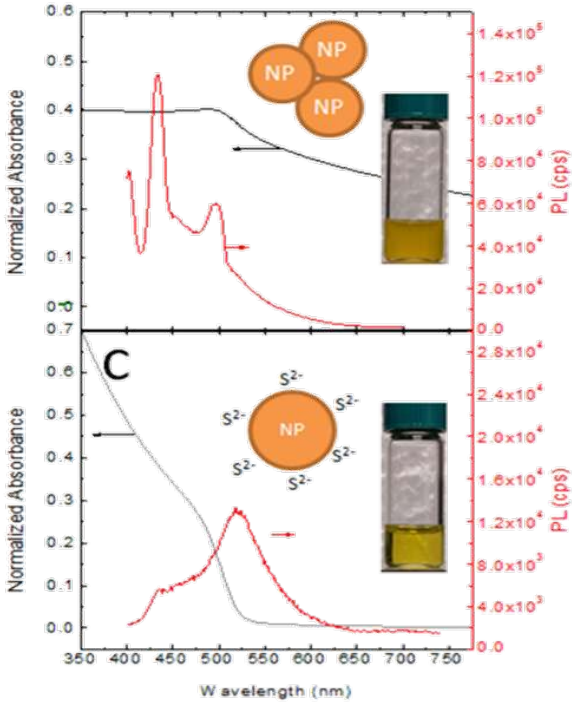

Figure 3.26. (a) Normalized absorbance of as produced NF-nanoparticles. The nanoparticles tend to aggregate, have solutions that are not stable, they are optically scattering and the photo-luminescence comes from high energy states (surface defects). (b) For the stabilized NF- nanoparticles there is no observable light scattering.

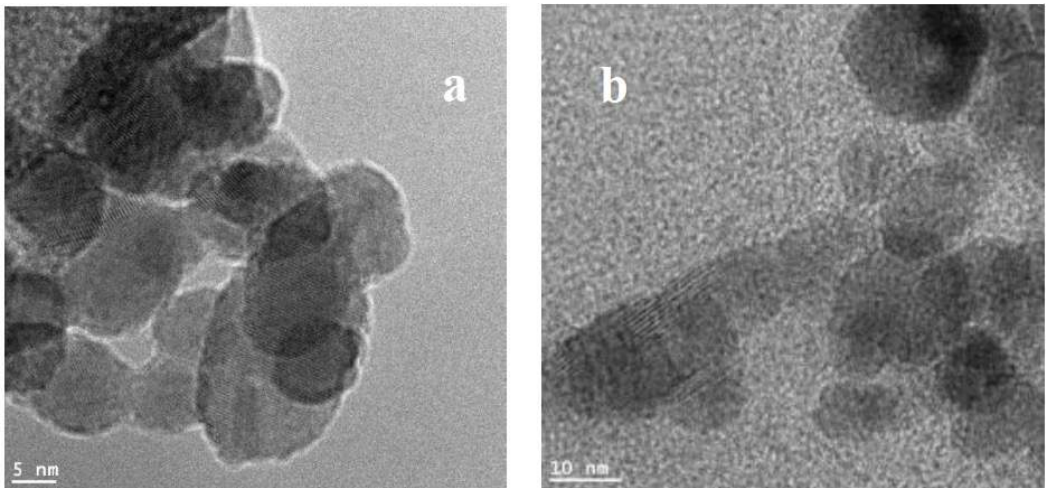

Figure 3.27. TEM images of (a) unmodified and (b) ligand stabilized NF-nanoparticles clusters.

4.5 LOW COST METAL OXIDE COATINGS

As a next step, nanofermented nanoparticles (ZnO, NiO, $SnO_{2)}$ thin films were deposited on stabilized polyimide substrates to measure the response of the film to humidity and temperature, with impedance measured as a function of frequency for different temperatures. The current as a function of applied voltage was also measured for several samples, as this information is crucial in the efforts to develop low cost sensors.

4.5.1 ZnO coatings

The ZnO coatings were developed on alumina substrates by screen-printing technique. Pt electrodes were also defined by the screen-printing technique. As shown in Figure 3.28, the Pt contact resistance was well-below 1Ω indicating its suitability for electrical measurements.

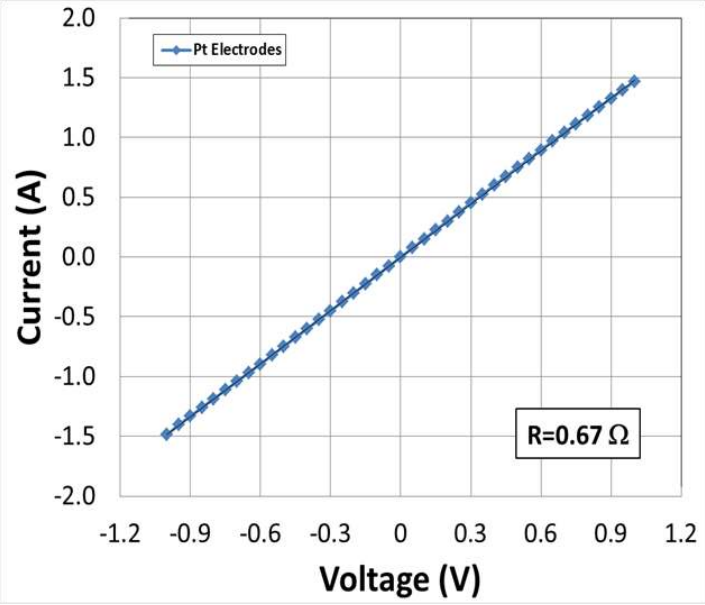

Figure 3.28. Current-voltage (I-V) response of Pt electrodes deposited on alumina substrates.

In order to optimize the line width, we screen printed ZnO on a polyimide substrate (Figure 3.29). We used this information to screen print ZnO lines between two Pt pads. This platform formed the basis for a low cost chemical sensor. In Figure 3.30(a) we show an optical image of the printed device. In Figure 3.30(b) we show the surface and depth profile of $ZnO/Pt/Al_2O_3$ structures as analyzed by optical microscopy.

The grain growth in ZnO coatings was analyzed by scanning electron microscope (SEM) as shown in Figure 3.31. Large grain growth was observed in NF particle based ZnO coatings sintered at 1100 °C. The SEM analysis indicated excessive stress in the ZnO coatings resulting in island formation and discontinuity in parts of the film. The SEM analysis was used to further optimize the chemical composition of the ZnO inks to improve the coating quality.

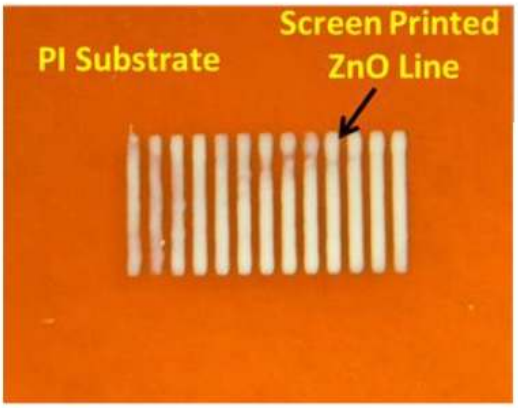

Figure 3.29. Screen printed ZnO lines.

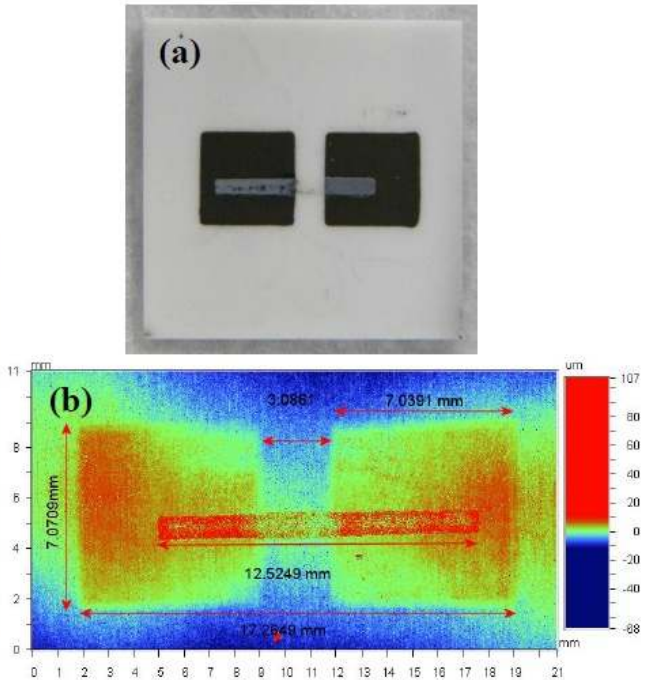

Figure 3.30. Surface and depth profile of ZnO/Pt/Al2O3 structures as analyzed by optical microscopy.

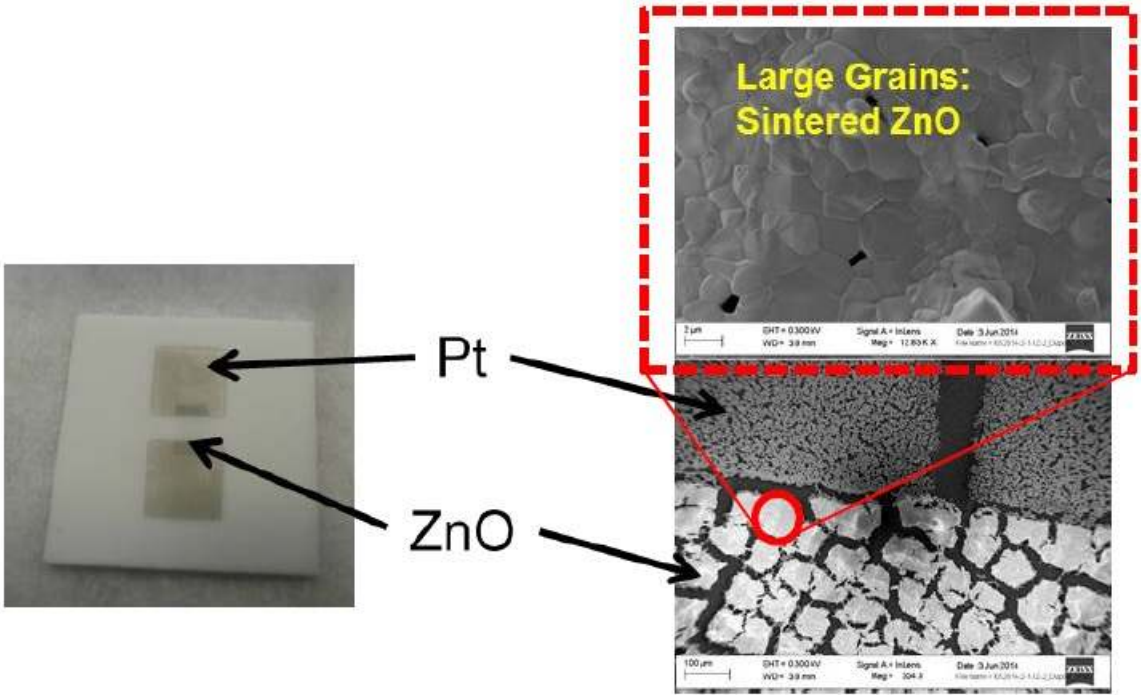

Figure 3.31. A scanning electron micrograph showing large grain growth in NF particle based ZnO coatings.

The electrical conductivity of the ZnO coatings was evaluated from the current-voltage (I-V) characteristics, as shown Figure 3.32, measured under room temperature conditions. A reference

ZnO sample was also prepared using commercial ZnO particles with an average size of about 10µm. The ZnO coatings sintered below 1100°C showed very low conductivity indicating poor grain connectivity and growth. The coatings sintered at 1100°C showed a significant improvement in electrical conductivity, however the conductivity-level was about two-orders of magnitude lower than the reference sample. The observed electrical conductivity characteristics indicated the presence of a large concentration of defects in the ZnO coating even after sintering at high temperatures.

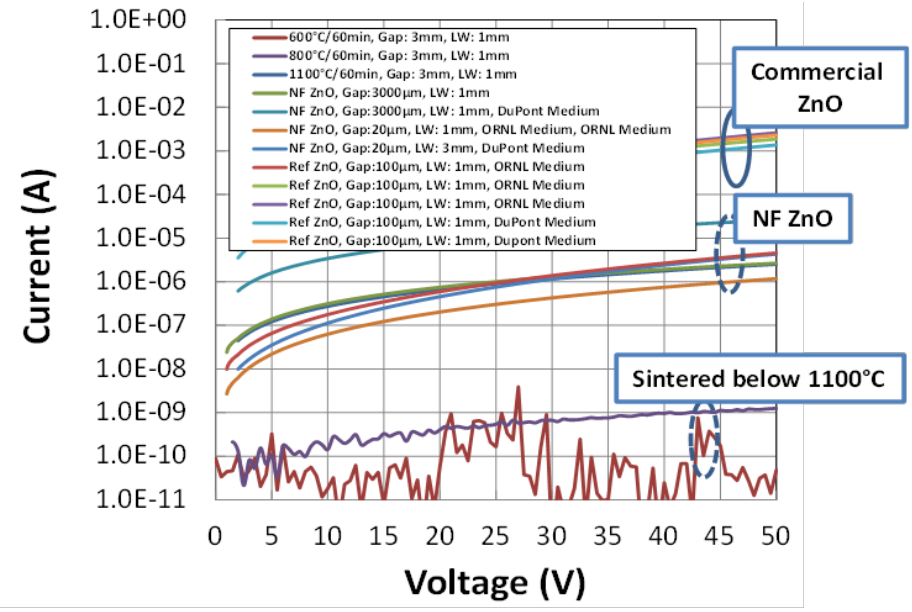

Figure 3.32. Current-voltage (I-V) characteristics of ZnO coatings sintered at various temperatures.

Forming gas annealing (FGA) was conducted to improve the electrical performance of the ZnO coatings. As shown in Figure 3.33(a), the electrical conductivity of the ZnO coatings improved by three-orders of magnitude after FGA, indicating effective passivation of the ZnO microstructure. A resistivity value of 0.45Ω-cm was calculated for these samples, which was suitable for analyzing the gas-sensitivity of the ZnO coatings. Based on these results, the path towards low-temperature coating development was still not clear, and further reductions in particle size below 200 nm was critical in reducing the processing temperature for low temperature electronic applications.

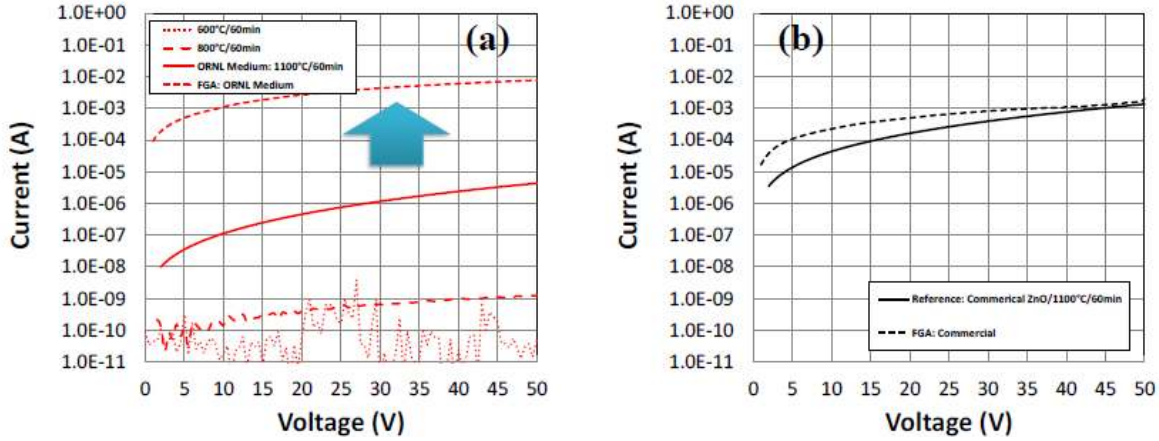

Figure 3.33. Impact of the forming gas annealing on the *I-V* characteristics of (a) NF ZnO particle coatings and (b) commercial ZnO particle coatings.

4.5.2 SnO_2 Coatings

The SnO_2 coatings were also developed for advanced sensor applications. A well-defined crystalline SnO_2 phase was observed after annealing at 400°C. The SnO_2 resistor configuration for the electrical measurements is shown in Figure 3.34. This device was annealed at 800°C and then at 1000°C. However, after annealing at 1000°C the Pt pads on the SnO_2 layer showed signs of delamination from the substrate, which prevented us from taking the measurements after annealing at 1000°C (Figure 3.35). The typical I-V characteristic of a coating sintered at 800°C is shown in Figure 3.36. The initial results indicate the formation of a highly resistive coating. A further annealing study as a function of ink formulation and NF process conditions was carried out to optimize the coating quality and improve the electrical characteristics.

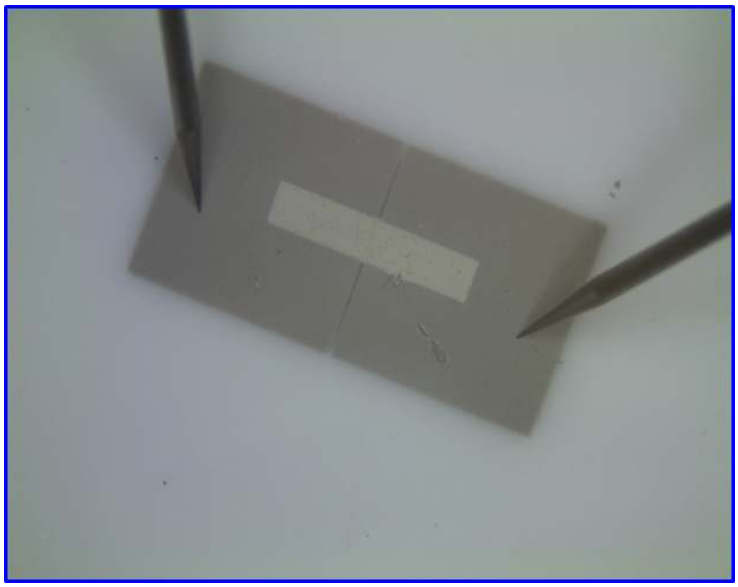

Figure 3.34. SnO_2 screen printed between two Pt pads.

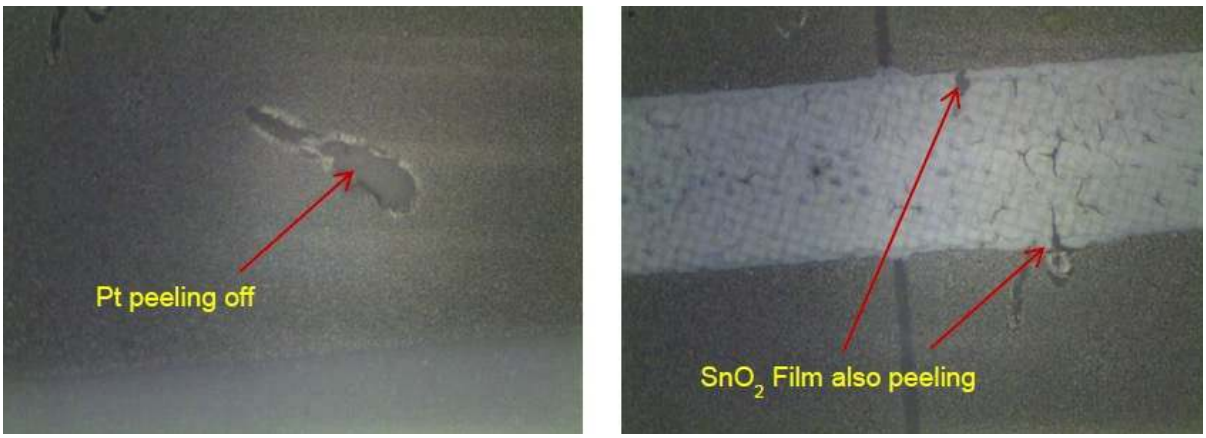

Figure 3.35. Pealing signs of the Pt layer (left) and the SnO_2 layer (right) after annealing at 1000°C.

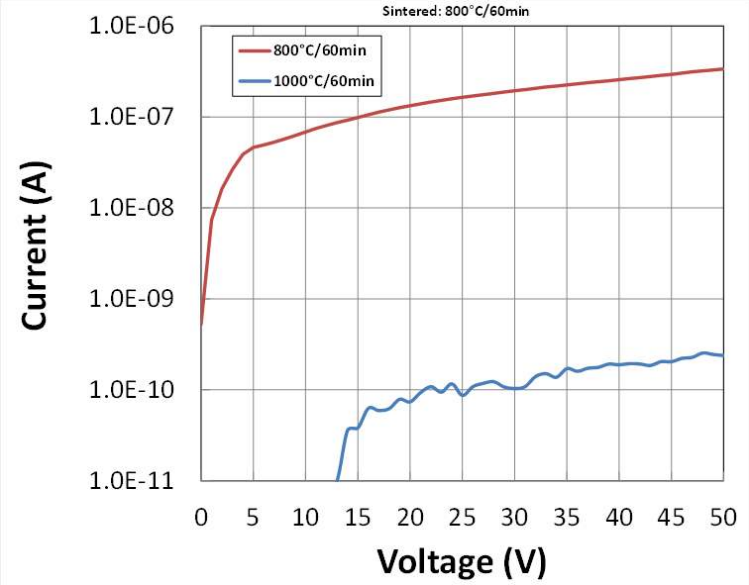

Figure 3.36. Current as a function of applied voltage for two annealing temperatures: 800°C and 1,100°C. Because the film developed discontinuities after annealing at 1000°C the conductivity could not be measured.

4.5.3 NiO Coatings

The NiO coatings have also been developed by screen-printing technique on Pt/Al_2O_3 structures using NF particle based inks. The as-processed NF particles were found to be quite large, as shown in Figure 2.14, with average size exceeding 10µm. The large size is possibly due to particle agglomeration, which calls for improved chemical processes for effective passivation of particle surface bonds. It was possible to reduce the particle size to the level of 1µm, which is still too large to exploit particle size effects for low temperature electronic applications.

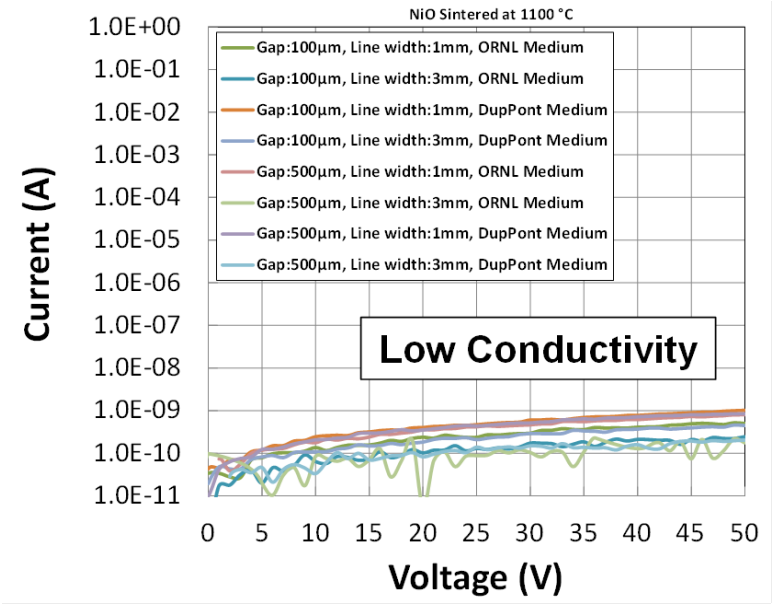

Figure 3.37. Current-voltage (I-V) characteristics of NiO coatings sintered at 1100 °C.

The electrical conductivity of the NiO coatings was found to be very low as shown in Figure 3.37. The effects of the NF process and the defect passivation annealing were investigated in detail to gain an insight into the factors controlling the electrical conductivity of NiO coating. Commercial NiO particle coatings were developed to establish a reference, and to analyze the key factors influencing the microstructure and electrical characteristics.

4.5.4 ZnO Sensors on Alumina Substrates

These metal-oxide-metal structures were employed, using inkjet printing, to demonstrate inter-digitized electrode printing, at 100 µm line width, on thin film metal-oxide at a low process temperature (<200°C). Figure 3.38 shows an optical image of a prototype sensor fabricated in this manner, and these structures were used for sensor characterization.

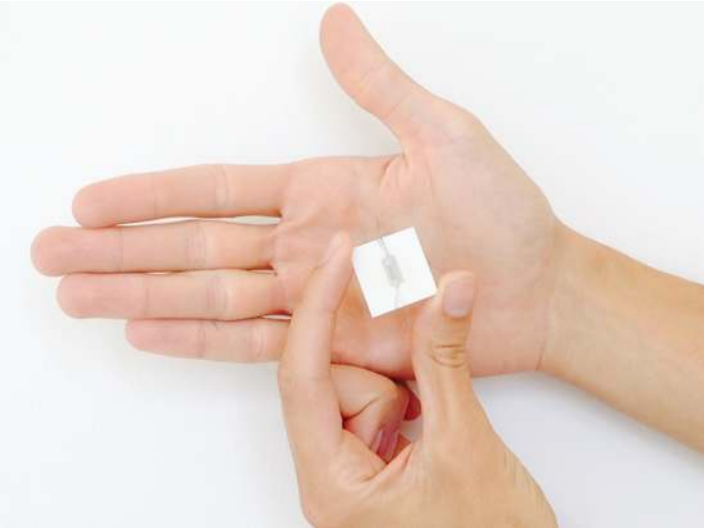

Figure 3.38. ZnO sensor made from 1 mm wide strip of screen printed ZnO on Alumina substrate. The electrodes were screen printed Pt 100 µm.

The sensors we have developed operate at 0.5 V compared to 5V of conventional sensors. It can be activated using UV light compared to conventional sensors that require 400°C for activation. Use of UV light is more energy efficient compared to using a high temperature system (see Figure 3.39(a)). The UV activation process improves sensor response by a factor of five, and the sensor response is directly proportional to the exposure time (amount of material). For the baseline sensor, the impedance was reduced by 55 kOhm under UV illumination, leading to a permanent change, and a 2x improvement in sensor impedance response to a single pulse. The sensor kinetics were 212 sec with UV activation and 23 sec partial recovery time (CO_2/H_2O).

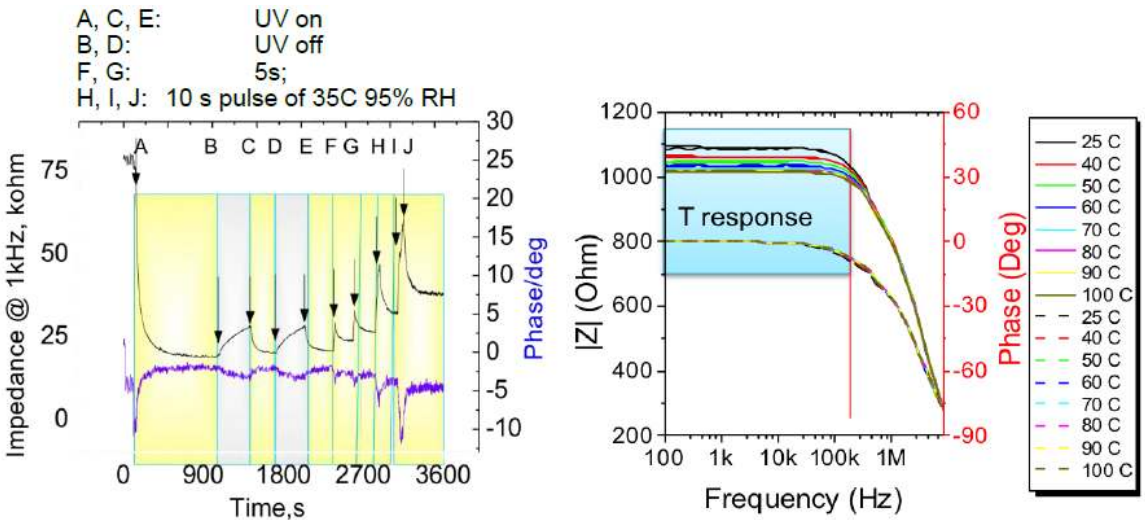

Figure 3.39. Response of ZnO thin film sensor to relative humidity under UV activation (a) as a function of UV illumination and (b) as a function of sensor temperature. The humidity response was measured at 35 C and 95% RH.

The complex impedance decreases as the temperature increases at frequencies < 200kHz (see Figure 3.39(b)). The temperature response is resistive up to about 200kHz and becomes capacitive above 200kHz on high purity, stabilized ZnO surfaces. On non-stabilized surfaces the response is capacitive. The response of the ZnO thin film sensor to temperature was also measured over the range of 25°C to 125°C, and we found the response to be linear (Figure 3.40) as a function of temperature

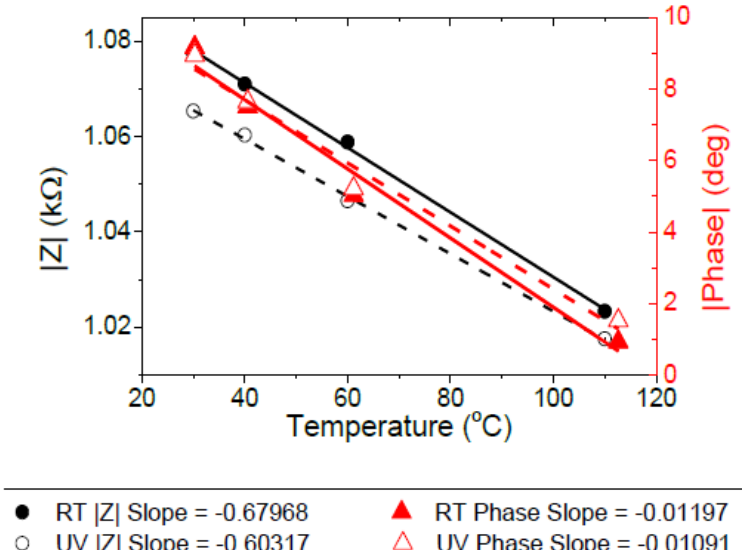

Figure 3.40. Response of ZnO thin film sensor as a function of temperature.

4.6 INTEGRATED SENSOR SUITE

As a final project task, a multi-sensor analysis suite was constructed that was used for the evaluation and testing of the low cost printed sensors that were fabricated using the nanofermented

nanoparticles. A user interface using LabView was designed and tested. This suite provided us with the ability to simultaneous detect several parameters. The software was modified to accommodate multiple sensors for testing as well as a low cost processor platform. Figure 3.41(a) shows a screen capture of the LabView based multi-channel software. Figure 3.41(b) shows a low cost processor prototype platform for mobile sensing which allows up to 5 sensors inputs, and was developed for implementation and testing of the nanofermented nanoparticles sensors. The readout of these sensors was through a Bluetooth connection.

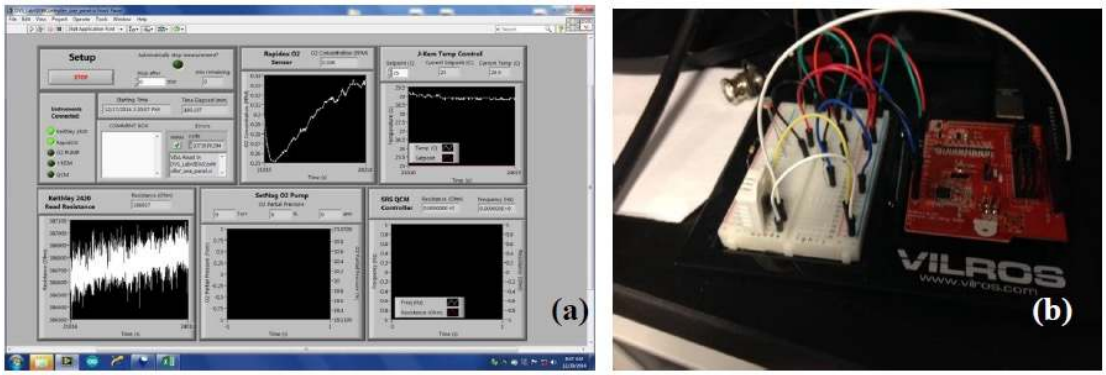

Figure 3.41. (a) Screen capture of the Labview based multi-channel software designed for tests of sensors manufactured from nanofermented nanoparticles, and (b) low cost processor platform for mobile sensing which allows to power up to 5 sensors is being developed for the implementation of the NF sensors.

We explored the effect of substrate temperature on the electrical properties of the ZnO films. The reference and NF ZnO films displayed similar trends. Namely, the low frequency impedance decreased significantly, by a factor of 4.5 and 6.9 for ref-ZnO and NF ZnO respectively, for samples deposited at elevated temperatures. The frequency dependence of the electrical properties for these samples was also measured. The measurements in Figure 3.42 are presented in the form of Nyquist plot of imaginary and real impedance of ZnO thin film sensors prepared using pulse laser deposition. The green and blue colored curves are data for reference ZnO samples and the black and red curves are measurements for the nanoferemented ZnO.

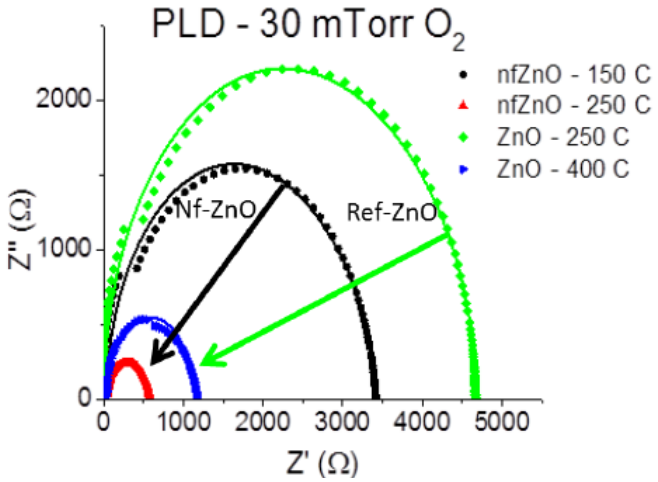

Figure 3.42. Frequency dependent electrical properties (presented in the form of Nyquist plot of imaginary and real impedance) of ZnO thin film sensors prepared using pulse laser deposition. The green and blue colored curves are data for reference ZnO samples and the black and red curves are measurements for the nanoferemented ZnO.

Table 3.3. Summary of the electrical properties of ZnO films prepared by pulse laser deposition.

Target	Temp (^oC)	Pressure 10^{-2} (Torr)	Gap (μm)	R_s (Ω)	L_1 10^{-6}(h)	R_1 (Ω)	C_1 (F)	R_2 (Ω)	C_2 (F)
NF ZnO	250	0.001	25	19.1	1.28	1.08 E $^{+4}$	1.17 E $^{-10}$	150.0	1.30 E $^{-10}$
NF ZnO	150		25	6.5	7.75	1.47 E $^{+3}$	1.32 E $^{-9}$	449.0	3.05 E $^{-6}$
	250		15	37.9	4.09	4.48 E $^{+2}$	1.07 E $^{-8}$	9.45	7.47 E $^{-7}$
ZnO	250	3.0	25	5.8		4.65 E $^{+4}$	3.09 E $^{-10}$	2.0 E $^{+4}$	5.23 E $^{-10}$
	400		25	43.4		2.07 E $^{+3}$	2.25 E $^{-10}$	197.0	1.29 E $^{-7}$

Table 3.3 summarizes the electrical properties of the ZnO films deposited on the Si/SiO_2 substrates. The deposition was carried at increasing substrate temperatures of 150^{o}C, 250^{o}C and 400^{o}C, and background oxygen pressures of 10^{-5} and 0.03 Torr. As the temperature of the substrate increased, the molecules move over longer distances to form a film like coating, whereas at low temperatures the mobility is limited, resulting in columnar structures on the film. The impedance spectra shown in Figure 3.42 were fitted using the model shown in Figure 3.43, which comprised a combination of R_S, L_1 and two parallel RC circuits, R_1, C_1 and R_2, C_2, connected in series. The physical model of the circuit consists of grain and boundaries of ZnO with additional contributions due to non-ohmic contact with platinum electrodes. Both resistances and capacitances changed from samples deposited at different temperatures, suggesting that either can be potentially implemented for sensing applications.

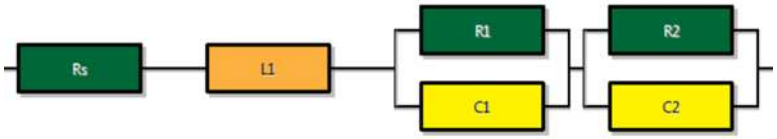

Figure 3.43. Model used to fit the measured data comprised by a combination of R_S, L_1 and two parallel RC circuits, R_1, C_1 and R_2, C_2, connected in series.

The sensing response of screen-printed ZnO sensor prepared from ZnS nanoferemented nanoparticles was also measured. The NF nanoparticles were first annealed in the air to convert them to ZnO, and then mixed with ORNL ink carrier for screen-printing. The screen-printing was on the alumina substrates with pre-deposited screen-printed platinum electrodes. After ZnO sensor line deposition, the sensor was annealed in air. The sensor was exposed to O_2 gas and the data collected through the Labview interface shown in Figure 3.41. The results are plotted in Figure 3.44. The black trace shows the unprocessed data for the original resistance the sensor, and the blue trace is the 200 point moving average. The ZnO sensor response was compared to that of a commercial automotive O_2 and its response is shown for comparison with the red trace. We found that that the NF ZnO sensor was responsive to < 500 ppm of oxygen.

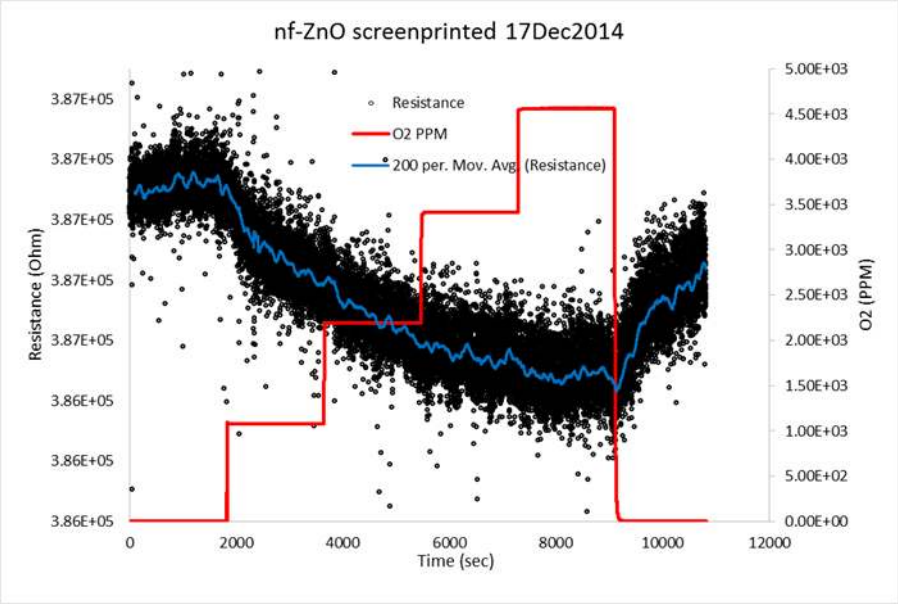

Figure 3.44. Oxygen response of screen printed ZnO sensor prepared from ZnS nanoferemented nanoparticles.

5. ACCOMPLISHMENTS AND CONCLUSIONS

The tasks making up this project had several successful outcomes. All the milestones associated with these tasks were successfully accomplished by the conclusion of the project. More specifically we have accomplished the following:

We have demonstrated Zn based opto-electronic sensors using low cost nanoparticulate structures manufactured using nanofermentation techniques from a related MDF project. We performed photoluminescence measurements and obtained and thin film coatings necessary for the several sensor and electronics applications.

We produced metal sulfide samples (ZnS, NiS, SnS, CoS, and Cu) which were studied over a temperature range in order to determine the optimum heat treatment conditions to convert the sulfide materials to their oxide forms. Using this approach we successfully developed functional metal oxide coatings and evaluated their performance in terms of crystallinity, composition, surface morphology, and mechanical integrity. These nanoparticles are extremely important in many areas of electronics and sensors. Some of the uses will be in p-type and n-type of semiconductor materials which will open up the opportunity for printed roll to roll electronics and sensors.

We used PTP to process high conductivity metallic traces. Silver strain gauges were printed directly on FDM photopolymer substrates. Using this approach we achieved sheet resistance <50 mΩ/sq for a 1.5 µm thick coating or ~5X silver bulk resistivity for PTP processed, printed silver on porous, rough surfaces such as paper or fibrous materials. We evaluated the use of silver based conductive inks developed by NovaCentrix for electronic device fabrication.

We developed metal-oxide-metal structures employing inkjet printing and demonstrated inter-digitized electrode (IDE) printing at 100 µm line width on metal-oxide thin film. We demonstrated a suite of low cost printed sensors developed using non-vacuum deposition techniques, which involved the integration of metal, and semiconductor layers to establish a diverse sensor platform technology.

We developed a multi-functional and low-cost resistive sensor integrated onto a flexible substrate and demonstrated low-cost ZnO sensor integrated for humidity and O_2 sensing.

We demonstrated a prototype humidity sensor on plastic substrates and identified an integrated sensor design scheme for multifunctional (gas, chemical, environmental) sensor platform

5.1 PATENTS

No new intellectual property was generated during this work.

5.2 PUBLICATIONS AND PRESENTATIONS

Publications:
G. Jang, C.B. Jacobs, I.N. Ivanov, Ilia, P. C. Joshi, H. M. Meyer III, M. Kidder, B. L. Armstrong, P. G. Datskos, D. E. Graham, and Ji-Won Moon, “In Situ Capping for Size Control of Monochalcogenide (ZnS, CdS and SnS) Nanocrystals Produced by Anaerobic Metal-Reducing Bacteria,” Chem Communications (accepted).

Presentations:
Chad Duty, “Roll-to-Roll Processing of Flexible Electronics," Next Generation Photovoltaics IUCRC Industrial Advisory Board Meeting." November 11, Knoxville, TN (2013) Invited.

C. Duty, University of Tennessee: Site Update, NSF Industry / University Cooperative Research Program Update (I/U CRC), Fort Collins, CO, July 30, 2013.

Teja Kuruganti, Stephen Killough, Pooran Joshi, “Low-Cost Wireless Sensor Networks for Building Applications Using Novel Materials and Energy-Efficient Communication Techniques,” Intelligent Building Operations Workshop, Boulder, CO, June 20-22, 2013.

Teja Kuruganti, Stephen Killough, Pooran Joshi, “Miniature Wireless Sensors as Printable Components,” 59th International Instrumentation Symposium, Cleveland, OH, May 13-17, 2013.

C. Duty, Photovoltaic MicroGrid Technology, Defense Manufacturing Conference, Anaheim, CA. November 12, 2012.

P. Joshi, R. Dehoff, C. Duty, W. Peter, R. Ott, L. Love, C. Blue, Direct Digital Additive Manufacturing Technologies: Path Towards Hybrid Integration, Future of Instrumentation International Workshop, Gatlinburg, TN, October 8-9, 2012.

5.3 COMMERCIALIZATION

Oak Ridge National Laboratory partnered with Novacentrix of Austin, Texas (printed electronics, nanoparticle manufacturing, pulsed power equipment) on commercialization of these technologies

This project provided advances in roll to roll manufacturing processes of thin film deposition on low-cost flexible substrates for electronics and sensor applications and suggests a promising avenue for the amalgamation of cutting edge nanotechnologies that can be utilized toward DOE’s mission fostering opportunities for U.S. companies.

Crucial to the commercialization strategy was the engagement of relevant industry partners (Novacentrix) during the course of the proposed work. We had several interactions with both Cabot Corporation and Novacentrix and have identified areas of future direction that will provide a clear path to commercialization of roll to roll manufacturing processes that include drying/sintering techniques for electrically-conductive inks, and commercially-relevant targets for nanoparticle thin films. In addition, the ORNL technology transfer program will assist in implementing the appropriate mechanism for transferring the technology developed in this work to the commercial arena using IP licensing agreements.

5.4 RECOMMENDATIONS

It is recommended that future work focus on several key aspect of the roll to roll approach in order to achieve rapid commercialization and capitalize on existing and emerging market opportunities. The development of non-vacuum, large scale deposition and processing techniques for nanoparticle-based inks and pastes will help reduce cost and energy requirements associated with processing of thin film electronics and sensors. Future efforts should focus on low-cost, flexible substrates, such as polymers and paper and be expanded to include embedded circuitry in additive manufactured components. Additive integration of metal interconnects using inkjet printing of conducting lines is important for

low-cost flexible electronics. This will define the path towards roll-to-roll processing of multifunctional sensors using low cost Ag and Cu inks for interconnects and ORNL's unique pulse thermal processing technology. Furthermore, integration of functionality into structures will allow not only electrical circuits and sensors but provide communication and energy generation / storage capability for a completely autonomous low-cost sensor node. A "traditional" sensor node costs ~ $150 while a flexible printed sensor node will be < $0.15.

The present work has demonstrated that low cost printed sensors can be fabricated using non-vacuum deposition techniques with the integration of metal and semiconductor layers. This provides a tremendous opportunity to incorporate such capability into additively manufactured products with sensing, energy storage and communications capability.